UNIVERSITY OF CALIFORNIA
RIVERSIDE

Faint Star-Forming Galaxies at the Peak Epoch of Star Formation: An Application of Strong Gravitational Lensing

A Dissertation submitted in partial satisfaction
of the requirements for the degree of

Doctor of Philosophy

in

Physics

by

Anahita Alavi

December 2016

Dissertation Committee:

Dr. Brian Siana, Chairperson
Dr. Bahram Mobasher
Dr. Naveen Reddy

The Dissertation of Anahita Alavi is approved:

_____

_____

_____

Committee Chairperson

University of California, Riverside

Acknowledgements

This thesis became a reality with the kind support and help of many individuals. I wish to acknowledge all of them.

I would like to express my sincere gratitude to my advisor, Professor Brian Siana, for his patience, motivation and his continuous support throughout my graduate study. He has always supported me not only by providing a research assistantship but also academically and emotionally through the rough road to finish this thesis. He genuinely cares about his students and believes that they can succeed. I was very lucky to work with him and I could not imagine having a better advisor and mentor for my Ph.D. study.

Besides, I would like to thank my thesis committee: Prof. Naveen Reddy and Prof. Bahram Mobasher for their insightful comments and questions. In particular, I thank Prof. Reddy for all the discussions that I had with him and his valuable comments about different parts of my Ph.D. projects. In addition, I am very grateful to Prof. Mobasher for encouraging me to come to UCR and all his help when I had just started as an international student.

I also thank Prof. Gabriela Canalizo for being in my qualifying exam committee and for her constant encouragement throughout my research period. I am grateful to have worked with intellectual and awesome collaborators Johan Richard, Marc Rafelski, Alberto Dominguez, Brant Robertson, Daniel Stark, Claudia Scarlata, Harry Teplitz, Mathilda Jauzac, and Marceau Limousin. In particular, I praise the enormous amount of help and explaining by Johan throughout these years of collaboration.

I am so grateful of my fellow colleagues William Freeman, Najmeh Emami, Kaveh Vasei, Louise Daniels and our new teammate Tim Gburek for their friendship and all the fun that we had during our group meetings. I also thank Ali Ahmad Khostovan and Amanda Pagul for many interesting discussions that we had. I want to thank Dr. Mario De Leo Winkler for all his endeavors for promoting outreach activities in our astronomy group and providing a joyful opportunity for graduate students including me to jointly work with him. A special

thanks to the Physics department student affairs officer Dr. Derek Beving who was always very helpful whenever I had any question or I needed any paperwork.

And to wrap this up, my biggest thanks to Nader, my beloved husband whose love and support has been always with me. Without you, I would not have been able to accomplish my dreams. You are the best and thanks for coming into my life.

Last but not the least, my beautiful parents receive my deepest gratitude and love for their dedications and many years of supporting and believing in me. And thank to my brother for all the sweet memories that he has made for me during all past years.

This work is partly based on research that has been either published in the Astrophysical Journal (2014ApJ...780...143A) or submitted to (manuscript number: AAS01234).

To Nader for his endless love

And to my parents and my grandma for their unconditional supports

ABSTRACT OF THE DISSERTATION

Faint Star-Forming Galaxies at the Peak Epoch of Star Formation:
An Application of Strong Gravitational Lensing

by

Anahita Alavi

Doctor of Philosophy, Graduate Program Physics
University of California, Riverside, December 2016
Dr. Brian Siana, Chairperson

Obtaining a complete census of cosmic star formation requires an understanding of the faint star-forming galaxies that are beyond the detection limits of our current surveys. To find these faint galaxies, we use the power of gravitational lensing from foreground massive galaxy clusters to push the detection limits of the Hubble Space Telescope (*HST*) to much fainter luminosities. Combining very deep ultraviolet, optical and near-IR imaging from *HST*, with magnification of strong gravitational lensing from three foreground galaxy clusters, we discover a sample of 780 ultra-faint star-forming galaxies at $1 < z < 3$. The UV absolute magnitude of these galaxies are extended down to very faint magnitudes of $M_{UV} < -12.5$ AB mag. Using this unprecedented sample, we study the evolution of the UV luminosity function (LF) between $1 < z < 3$. We find that the UV LFs are steep with an estimate of faint-end slopes of $\alpha = -1.56 \pm 0.04$, $\alpha = -1.72 \pm 0.04$ and $\alpha = -1.94 \pm 0.06$ at $1.0 < z < 1.6$, $1.6 < z < 2.2$ and $2.2 < z < 3.0$, respectively. We demonstrate that there is no sign of turnover in these UV LFs at least down to $M_{UV} = -14$. As an important consequence of steep LFs, we show that the faint star-forming galaxies covered in this study with $-18 < M_{UV} < -12.5$, produce a majority ($55\% - 60\%$) of the unobscured UV luminosity density

at $1 < z < 3$. Furthermore, we examine two techniques, fitting a power law to broad-band photometry as well as best-fit SED for each object, to study the evolution of rest-frame UV spectral slopes β for these ultra-faint galaxies. We demonstrate that our UV spectral slopes β change with UV luminosity, such that galaxies become bluer at fainter luminosities. However, we show that the UV spectral slope $\beta - M_{UV}$ correlation is not tight and there is a large intrinsic scatter in the UV slope distribution at a given M_{UV}. Using hydro-dynamical simulations of dwarf galaxies, we demonstrate that the bursty star formation histories alone can explain the intrinsic scatter in β.

Contents

List of Figures

List of Tables

Chapter 1

Introduction

Understanding how galaxies form and evolve throughout cosmic time is one of the most fundamental questions in observational cosmology today. The story of structure formation in the universe starts shortly after the Big Bang, when the initial density fluctuations begin to grow in amplitude. The distribution of these early density fluctuations are imprinted in the cosmic microwave background (CMB) radiation emitted 377000 years after the Big Bang. These early over-dense regions grow as gravity causes them to draw more material from the surrounding. The first generation of galaxies formed about 400 million years after the Big Bang, when the density perturbation had grown enough to build dense cloud of dark and baryonic matter. This time coincides with the so-called reionization era, when a transition from neutral hydrogen intergalactic medium (IGM) to ionized IGM occurred. The reionization era ends about 1Gyr after the Big Bang at $z \sim 6$, when the IGM is fully ionized by the ionizing radiation (i.e., Lyman continuum photons) from as yet unknown sources. It is believed that the young stars in the early galaxies are likely one of the principal sources of these ionizing photons during the epoch of reionization, when only 1% of today stellar mass density was formed (Madau and Dickinson, 2014).

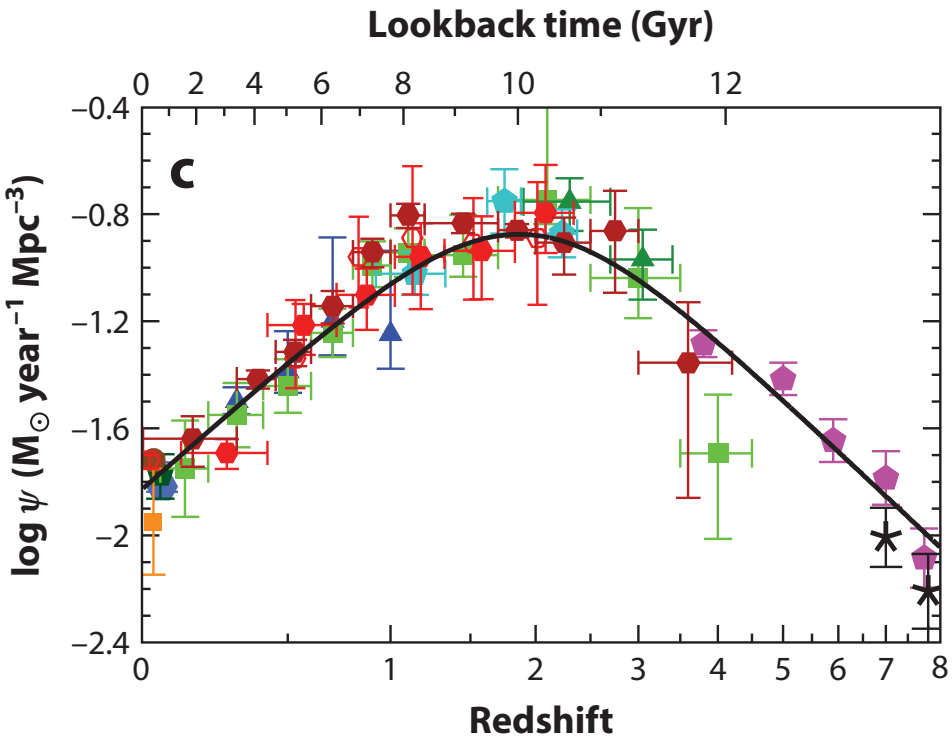

Figure 1.1: Cosmic star formation history taken from Madau and Dickinson (2014). The star formation rate density peaks between $z = 1 - 3$.

1.1 Cosmic Star Formation History

Over the last decade, great progress has been made in probing the galaxy build-up from the reionization epoch at $z = 7 - 8$ to the present time (Madau and Dickinson, 2014, and references therein). Combining all of these studies, there is a remarkably consistent picture of cosmic star formation history (SFH, Figure 1.1) during the past 13.8 billion years. As shown in Figure 1.1, the galaxies continue to build up their stellar mass with time from z=8 to z=3 (SFH $\propto (1+z)^{-2.9}$, Madau and Dickinson, 2014), until the star formation density peaks at some point between $1 < z < 3$. After z=1, when the universe was $\sim$ 6 Gyr old about half of its present age, the cosmic star formation density declines toward present times (SFH $\propto (1+z)^{2.7}$, Madau and Dickinson, 2014).

Understanding this peak epoch of star formation is particularly important for completing the picture of galaxy evolution. Based on many studies of the stellar mass function at high redshifts (Ilbert et al., 2013; Muzzin et al., 2013; Tomczak et al., 2014), $> 50\%$ of current total stellar mass density formed at this time. In addition to the star formation activity, the AGN activity peaked during this era, as well.

Over the past twenty years, many multi-wavelength surveys have employed a variety of novel techniques to find the galaxies from this peak epoch. In order to study the diverse population of galaxies at these redshifts, these surveys select their targets via different parts of their electromagnetic spectrum. From the most commonly used techniques: a) many studies have selected the galaxies via their rest-frame UV colors (e.g., Lyman break selection (LBG), Steidel et al., 1999). This technique particularly identifies the star-forming galaxies with ongoing star formation and thus it is not sensitive to passive galaxies. b) many studies select the galaxies based on their rest-frame optical colors (e.g., BZK, Daddi et al., 2004). This technique finds both star-forming and quiescent galaxies. c) Because there is an increase in the overall star formation activity in the universe during this peak epoch, there are extremely luminous dusty objects, which emit most of their lights in the far-IR wavelengths. To observe this group of galaxies, some studies select the galaxies based on their sub-millimeter and mid-IR light (SMG, Smail et al., 1997).

From these different techniques, the rest-frame UV selection is likely the most practical method for imaging the galaxies at $1 < z < 3$. This is especially true after the installation of WFC3/UVIS camera on the Hubble Space Telescope (*HST*), which provides a unique opportunity for imaging the galaxies at $1 < z < 3$ in the rest-frame UV wavelengths. In addition, the fact that the UV light is dominated by the young stars in the galaxies, makes it a powerful tracer of star formation activity.

One of the most useful tools for studying the early galaxies is the luminosity function (LF), which assesses the number density of galaxies at different luminosities. Therefore, the UV LF is an important diagnostic to measure the contribution of the star-forming galaxies with different luminosities to the total star formation density at different cosmic times. In

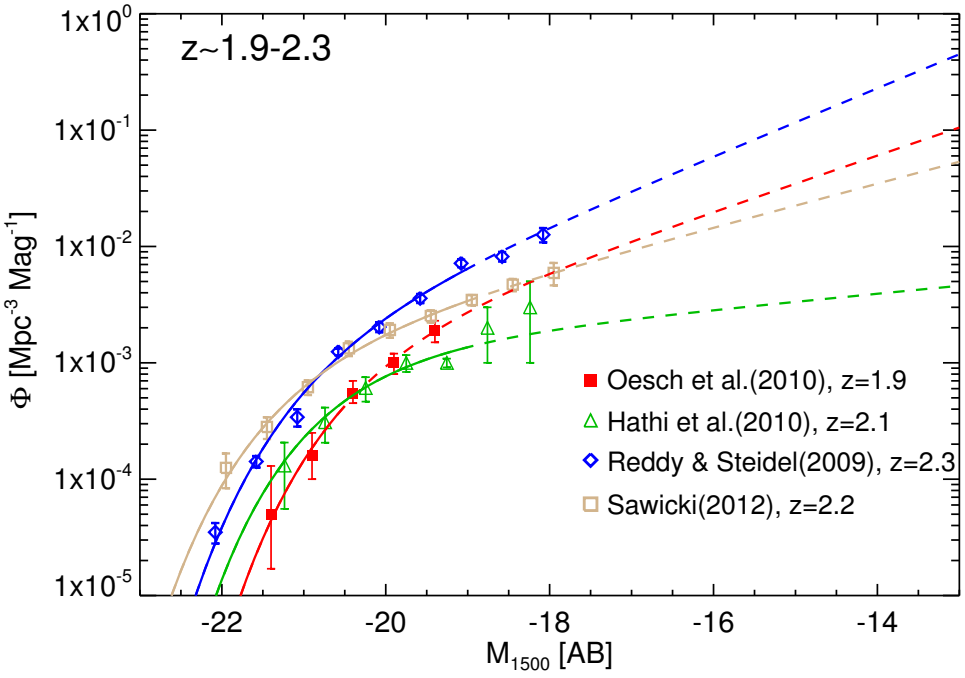

Figure 1.2: The UV luminosity function of $z \sim 2$ galaxies. Each symbol shows the measured number density of galaxies at a given absolute magnitude bin, M_{UV}, at bright luminosities. The dashed lines show the extrapolation to fainter luminosities.

particular, the UV LF at the peak epoch of cosmic star formation has been extensively studied by different groups. Figure 1.2 shows some of the well-known UV LF measurements at $z \sim 2$ (Reddy and Steidel, 2009; Hathi et al., 2010; Oesch et al., 2010a; Sawicki, 2012). The UV LF shape shows a power-law slope at faint luminosities and an exponentially cut-off at bright luminosities. As seen in this figure, the UV LF measurements of faint galaxies and thus their contribution to the total UV light is very poorly constrained. This is because these studies are missing many faint galaxies. This uncertainty in the UV LF measurements, can affect our estimate of the total star formation density at these redshifts.

1.2 Why Faint Galaxies Are Important?

Faint galaxies, so-called dwarf galaxies, are the smallest and least luminous, but most abundant galaxies in the Universe. These galaxies have stellar masses between $10^6 < M_*/M_\odot <$

10^9. Below, we briefly explain why these galaxies play a critical role in the galaxy formation and evolution.

- Broadly, the high-redshift studies measure a steep faint-end slope for the UV luminosity function. As a direct consequence of a steep UV LF, the large volume density of faint star-forming galaxies can cause them to have a significant contribution in the total UV light (Bouwens, 2016). Consequently, the faint galaxies likely host a large fraction of total stars in the early universe.

- The faint galaxies are the most plausible sources of ionizing photons during the reionization epoch. As discussed in Robertson et al. (2013), to fully reionize the IGM by $z = 6$, the UV LF should be extended down to an absolute magnitude of $M_{UV} = -13$. Moreover, the faint galaxies are believed to have larger escape fraction for ionizing photons than their brighter counterparts. Although at high-redshift, searches for the Lyman continuum (LyC) photons from galaxies have been very difficult and mostly unsuccessful. But, a recent direct detection of LyC leakage from low-mass compact star-forming galaxies at $z < 1$ (Green Peas, Izotov et al., 2016a,b), as well as at $z > 3$ (*Ion2* at z=3.2, Vanzella et al., 2016) indicates that these low-mass systems are likely promising candidates for high escape fraction.

- The dwarf galaxies significantly contribute to the IGM metal enrichment at high redshifts. As shown in different studies (Madau et al., 2001; Porciani and Madau, 2005), the galaxy-scale outflows (i.e., supernova winds) can easily overcome the low gravitational potential of dwarf galaxies and thus the enriched material can be ejected far from the galaxy.

- The dwarf galaxies maintain the ionizing background at high redshifts ($z > 3$, Nestor et al., 2011). This can be understood by considering their large number density and high escape fraction of ionizing photons at these redshifts. However, at lower redshifts $z < 2$, the contribution from Quasi-stellar objects, QSO, in the total ionizing emissivity dominates.

Despite these important reasons, the dwarf galaxies have been inaccessible to high-redshift UV searches, because they are far below the detection limits of current surveys.

1.3 Strong Gravitation Lensing

According to the general relativity theory, massive objects such as galaxies can change the path of light passing in the vicinity of that object, refocus it somewhere else, and ultimately magnify the background source. Therefore, the observed image is brighter and its shape is distorted relative to the original source. Because the gravitational lensing conserves the surface brightness, both the flux and area are increased by the same value. In order to study a lensed source, one needs to correct the observed flux for the magnification. However, because the lensing magnification is independent of the wavelength of the light, those galaxy properties which are dependent on the ratio of fluxes, are not affected by the lensing magnification and thus do not need any correction.

The distances between the observer, lens and background source as well as the gravitational field of the lens are the main factors that determine the amount of magnification. If the lens has a strong gravitational field, and the source and lens have very close alignment, the lensing regime is called strong gravitational lensing. Galaxy clusters, which are the most massive bound structures in the universe, are the strongest lenses and provide strong gravitational lensing. Among these lenses, those massive clusters, which have very high density in the inner regions, can even break the wave front emitted by the background source and thus produce multiple images of a single object (Figure 1.3). In this case, from the point of view of an observer it appears as two light rays emitted by the same source have travelled from two different directions. The strong gravitational lensing from foreground galaxy clusters offers three significant advantages for studying the high redshift galaxies. First, they provide high magnification over large area. Second, due to the high magnification, one can find new galaxies that otherwise are too faint to be detected. Finally, because the phenomenon of gravitational lensing increases the apparent size of background galaxy, it allows a study

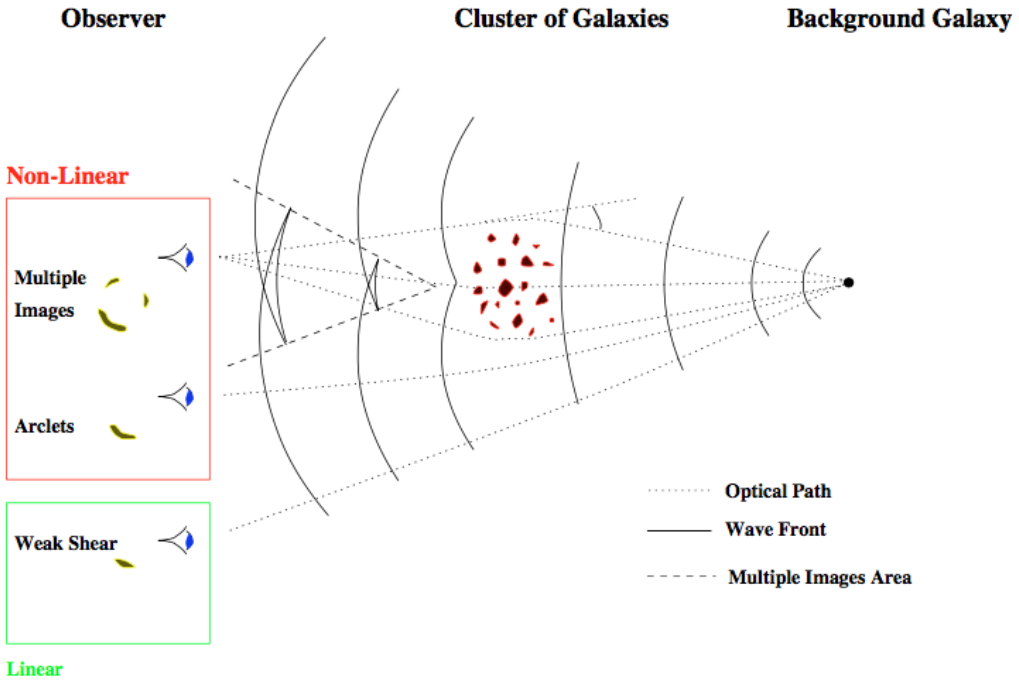

Figure 1.3: Strong gravitational lensing in clusters taken from Kneib and Natarajan (2011). A schematic of how massive foreground galaxy clusters generate multiple images of a single background object.

of the morphology of distant and/or faint galaxies, which otherwise would be unresolved. These massive clusters can provide magnification of a few up to a few hundred over a few square arcminutes.

This technique of using magnification from the foreground galaxy clusters has been extensively used by different groups for a variety of reasons such as finding very high-redshift galaxies up to $z = 10$ (e.g., Richard et al., 2008; Zitrin et al., 2014) as well as measuring the physical properties of lensed galaxies at $z \sim 2 - 3$ using their resolved spectroscopy (Jones et al., 2010). Specifically, after the installation of both ACS and WFC3 cameras on board *HST*, there has been a growing interest in using lensing clusters as well as designing surveys targeting these lenses in different wavelengths. In Figure 1.4, we show color images of three lensing clusters, Abell 1689 , Abell 2744 and MACSJ0717, which are used in this thesis. The high magnification from these lensing clusters allows us to uncover a large population of long-suspected dwarf galaxies at $1 < z < 3$.

Figure 1.4: These color images show three lensing clusters that are used in this thesis. The Abell 2744 andMACSJ0717 clusters from the Hubble Frontier Fields (HFFs) program are shown in the first row left and right panels, respectively. The Abell 1689 cluster is shown in the second row. The images of the HFF clusters are composite of optical and near-IR data. The image of Abell 1689 is composite of UV and optical data.

1.4 Summary of Thesis

In this thesis, we study the faint star-forming galaxies at the peak epoch of cosmic star formation, $1 < z < 3$. To this end, we target the galaxies behind the foreground massive clusters, where the strong gravitational lensing effect provides the high magnification required for detecting these faint galaxies. Below, we summarize the structure of this manuscript.

Chapter 2: We obtain very deep UV imaging of a massive galaxy cluster Abell 1689. Taking advantage of the magnification of strong gravitational lensing from this cluster, for the first time, we present a sample of ultra-faint LBG galaxies with UV absolute magnitude of $M_{UV} > -13$ at $z \sim 2$. These lensed galaxies in our sample are $100\times$ fainter than previous surveys at this redshift. Therefore, we are able to provide a robust measurement of the faint-end slope of the UV LF at $z \sim 2$. We derive a steeper faint-end slope, when compared to the previous determinations at the same redshift. This has an important effect on the estimate of the total UV luminosity density at these redshifts. Measuring the average dust reddening of these faint galaxies, we also estimate the global star formation rate density at $z \sim 2$.

Chapter 3: We study the evolution of the faint-end slope of the UV LFs during the peak epoch of cosmic star formation at $1 < z < 3$. Using deep multi-wavelength images of 3 lensing clusters, we apply two selection methodologies of photometric redshifts and Lyman break "dropout" technique and we find a large sample of faint star-forming galaxies at these redshifts. Thanks to the magnification from these lensing galaxy clusters, we extend the UV LFs at $1 < z < 3$ to very faint UV absolute magnitudes of $M_{UV} = -12.5$. We demonstrate that the faint-end slope is steep and becomes steeper from $z \sim 1.3$ to $z \sim 2.6$. Consequently, we show that the faint galaxies contribute significantly to the total unobscured UV luminosity density at these redshifts.

Chapter 4: We provide a comprehensive measurement of the rest-frame UV spectral slopes (β) of a population of faint star-forming galaxies at $1<z<3$. We adopt two different techniques for measuring the UV spectral slopes β and we show that our final results are

robust against the choice of technique. We investigate the relation between the β values and UV absolute magnitudes by measuring the slope and scatter. The slope of the $\beta - M_{UV}$ relation indicates that the galaxies with lower UV luminosities have on average bluer UV spectral slopes. However, we show that there is a large intrinsic scatter in this relation. We further investigate this intrinsic scatter using a sample of simulated galaxies with bursty star formation histories, SFHs. We conclude that the bursty SFHs can cause dramatic changes in the UV spectral slopes of faint galaxies.

Chapter 2

Ultra-faint Ultraviolet Galaxies at $z \sim 2$ Behind the Lensing Cluster Abell 1689: the Luminosity Function, Dust Extinction and Star Formation Rate Density

Abstract

We have obtained deep ultraviolet imaging of the lensing cluster Abell 1689 with the WFC3/UVIS camera onboard the *Hubble Space Telescope* (*HST*) in the F275W (30 orbits) and F336W (4 orbits) filters. These images are used to identify $z \sim 2$ star-forming galaxies via their Lyman break, in the same manner that galaxies are typically selected at $z \geq 3$. Because of the unprecedented depth of the images and the large magnification provided by the lensing cluster, we detect galaxies 100× fainter than previous surveys at this redshift. After removing all multiple images, we have 58 galaxies in our sample between $-19.5 < M_{1500} < -13$ AB mag. Because the mass distribution of Abell 1689 is well con-

strained, we are able to calculate the intrinsic sensitivity of the observations as a function of source plane position, allowing for accurate determinations of effective volume as a function of luminosity. We fit the faint-end slope of the luminosity function to be $\alpha = -1.74 \pm 0.08$, which is consistent with the values obtained for $2.5 < z < 6$. Notably, there is no turnover in the luminosity function down to $M_{1500} = -13$ AB mag. We fit the UV spectral slopes with photometry from existing *Hubble* optical imaging. The observed trend of increasingly redder slopes with luminosity at higher redshifts is observed in our sample, but with redder slopes at all luminosities and average reddening of $< E(B-V) >= 0.15$ mag. We assume the stars in these galaxies are metal poor ($0.2\ Z_{\odot}$) compared to their brighter counterparts ($Z_{\odot}$), resulting in bluer assumed intrinsic UV slopes and larger derived values for dust extinction. The total UV luminosity density at $z \sim 2$ is $4.31^{+0.68}_{-0.60} \times 10^{26}$ erg s^{-1} Hz^{-1} Mpc^{-3}, more than 70% of which is emitted by galaxies in the luminosity range of our sample. Finally, we determine the global star formation rate density from UV-selected galaxies at $z \sim 2$ (assuming a constant dust extinction correction of 4.2 over all luminosities and a Kroupa IMF) of $0.148^{+0.023}_{-0.020}$ M$_{\odot}$ yr^{-1} Mpc^{-3}, significantly higher than previous determinations because of the additional population of fainter galaxies and the larger dust correction factors.

2.1 Introduction

A primary goal of observational cosmology has been to obtain a complete census of star formation at all epochs (e.g., Madau et al., 1996; Lilly et al., 1996). One effective method of selecting star-forming galaxies is to identify a "Lyman break" in the ultraviolet (UV) continuum caused by Lyman line and continuum absorption from hydrogen in the stellar atmospheres, interstellar medium, and the intergalactic medium (Steidel et al., 1999). This technique was first used to select the star-forming galaxies as U-band "dropouts" at z$\sim$3 (Steidel et al., 1999), and has since been widely adopted to select Lyman break galaxies (LBGs) at higher redshifts (e.g., Bunker et al., 2004; Sawicki and Thompson, 2006; Yan et al., 2006; Bouwens et al., 2007, 2009; Reddy and Steidel, 2009; Oesch et al., 2010b; Bunker et al., 2010; Yan et al., 2010; Hathi et al., 2010).

Although the peak epoch of star formation is likely at lower redshifts ($1.5 < z < 3$, e.g., Ly et al., 2009; Reddy and Steidel, 2009), it has been impossible to select galaxies at these redshifts via their Lyman break without imaging at wavelengths below the atmospheric limit, $\lambda < 3100$ Å. Other selection methods such as the BM/BX (Adelberger et al., 2004) and BzK (Daddi et al., 2004) criteria have been used, but unambiguous comparison with Lyman break selected galaxies at $z \geq 3$ is difficult because the selection effects are different.

The new Wide–Field Camera 3 (WFC3) on the *Hubble Space Telescope* has an ultraviolet/optical channel (UVIS) that increases survey efficiency (area $\times$ throughput) by more than an order of magnitude compared with WFPC2. With the first ultraviolet images in the Early Release Survey (ERS) (Windhorst et al., 2011), star-forming galaxies were selected via the Lyman break technique at $1 < z < 3$ (Oesch et al., 2010a; Hathi et al., 2010). These studies were limited by the depth of the shallow ultraviolet imaging and could only detect galaxies with absolute UV magnitude (typically measured at 1500 Å, M_{1500}) brighter than -19 AB-mag, making it impossible to accurately constrain the faint-end slope of the UV luminosity function (LF).

Rest-frame ultraviolet light is a strong tracer of unobscured star formation, so the UV luminosity function can be used to determine the relative contribution of faint and bright galaxies to the total star formation rate density (SFRD). The UV LF has been studied widely at this active star forming era (Arnouts et al., 2005; Reddy and Steidel, 2009; Hathi et al., 2010; Oesch et al., 2010a).

There are two difficulties in determining a complete census of star formation. First, the ultraviolet light emitted by bolometrically luminous galaxies is significantly attenuated by dust, which causes UV-selected samples to be incomplete at the bright end. However, these galaxies can be identified by their far-infrared emission (Reddy et al., 2006; Magnelli et al., 2011). Second, there may be a large population of faint star-forming galaxies beyond the detection limit of the deepest surveys (typically $M_{1500} < -18$ AB-mag).

This population of faint ultraviolet galaxies may contribute significantly to the global star formation density and the ionizing background (Nestor et al., 2013) at $z > 2$. Recent searches at z=3 (Nestor et al., 2011) have revealed that faint star-forming galaxies on average have larger Lyman continuum escape fractions relative to the brighter galaxies. This result proves the importance of these feeble objects in maintaining the ionizing emissivity especially at the peak of star formation activity. In addition to the crucial role of the faint galaxies at lower redshifts, it is believed that low luminosity galaxies at $z > 7$ are likely the primary sources of ionizing photons that caused the reionization of the intergalactic medium (Kuhlen and Faucher-Giguère, 2012; Robertson et al., 2013). Studying an analogous population at lower redshifts ($z \sim 2$) provides a clearer picture of ultra-faint populations at high redshifts.

One way to efficiently detect and study these faint galaxies is to use foreground massive systems as lenses to magnify background galaxies. This strong gravitational lensing conserves surface brightness while spreading out a galaxies' light over a larger area and magnifying it. Over the last decade, this has been used to study individual lensed galaxies in great detail (e.g., Pettini et al., 2002; Siana et al., 2008b, 2009; Stark et al., 2008; Jones et al., 2010; Yuan et al., 2013).

When using strong lensing to identify large numbers of faint galaxies, galaxy clusters are particularly useful as they highly magnify background galaxies over a large area (Narayan et al., 1984). The regions amplified by a higher factor have smaller source-plane area, so the benefit of magnification is offset by reduced sample volume. Therefore the total number of candidate galaxies behind a cluster could be either smaller or larger than a field survey of the same depth and area, due to the competition between these two variables. Determining the ratio of the total number of galaxies found by using cluster lensing relative to the field studies, depends on the effective slope of the luminosity function (Broadhurst et al., 1995; Bouwens et al., 2009). If the effective slope of the luminosity function, $-d \log \phi / d \log L$, is greater than unity then a survey behind a lensing cluster will find more objects than the same survey in the field. Lensing clusters have been used to identify very high redshift objects (e.g., Kneib et al., 2004; Egami et al., 2005; Stark et al., 2007; Bradley et al., 2008; Richard et al., 2008; Bouwens et al., 2009; Richard et al., 2011; Bouwens et al., 2012a; Zheng et al., 2012; Zitrin et al., 2012; Coe et al., 2013) because the luminosities probed are on the steep, bright end of the luminosity function, resulting in larger samples than field surveys. Historically, surveys have not used lensing clusters to identify galaxies significantly fainter than L^* because it finds fewer galaxies. However, our primary concern is not the *number* of galaxies found, but the intrinsic *luminosity* of the galaxies. The average luminosity of galaxies found behind a lensing cluster will be significantly lower than surveys in the field. Because we are interested in finding galaxies that are undetected in our deepest field surveys, we chose to survey faint star-forming galaxies behind massive clusters. Once these ultra-faint galaxies are identified, the lensing will allow detailed study as they are highly magnified and the light is spread over many more resolution elements. This strategy of surveying large numbers of background galaxies with deep observations of lensing clusters will soon be adopted with deep *Hubble* imaging of the Frontier Fields beginning in Cycle 21.

In this paper we use the WFC3/UVIS channel to look for faint star-forming galaxies located behind the massive cluster Abell 1689. This cluster has the most constrained cluster mass model due to the large number of confirmed multiply imaged systems (43), of which 24

have spectroscopic redshifts (Limousin et al., 2007; Coe et al., 2010). This mass model gives us a precise estimation of magnification factor over the total area. The high magnification area for this cluster is well-matched with the WFC3/UVIS field of view. Abell 1689 has been observed extensively with *HST* in the optical with ACS/WFC (F475W, F625W, F775W, F814W, F850LP) and the near-IR with WFC3/IR (F105W, F125W, F140W, F160W), *Spitzer* IRAC and MIPS as well as *Herschel* PACS and SPIRE.

The outline of this paper is as follows. In Section 2.2, we describe the observations and data reduction. The selection technique is given in Section 2.3. In Section 3.7 we discuss the details of the completeness simulation as well as the Monte Carlo simulation used for IGM opacity. The redshift distribution of the sample is explained in this section. We explain the maximum likelihood method used for estimating the rest-frame UV luminosity function parameters in Section 2.5. In Section 2.6 we determine the dust content of the selected Lyman break galaxies. In Section 3.10, we compare our final results for the UV luminosity density and evolution of the faint-end slope and dust extinction with other results in the literature. We also briefly discuss about the effect of the intracluster dust. Finally, we present a short summary in Section 2.8.

All distances and volumes are in comoving coordinates. All magnitudes are given in the AB system (Oke and Gunn, 1983). We assume $\Omega_M = 0.3$, $\Omega_\Lambda = 0.7$ and $H_0 = 70$ km s^{-1} Mpc^{-1}.

2.2 Observations

We used the WFC3 UVIS channel to obtain images in F275W (30 orbits) and F336W (4 orbits) as part of *HST* Program ID 12201 (PI: B. Siana) between December, 2010 and March, 2011. We used long exposure times, half an orbit in length (1310s each) in order to minimize the total read noise, as this is the dominant source of noise in near-UV imaging with *Hubble*. The data were obtained in two orbit visits during which we performed the standard UVIS dither pattern, WFC3-UVIS-DITHER-BOX. Each dither pattern was offset up to ±3" from

Table 2.1. WFC3/UVIS and ACS/WFC Magnitude Limits

Filter	F275W	F336W	F475W	F625W	F775W	F850LP
Magnitude Limit[a]	28.7	27.90	28.55	28.29	28.17	27.80

[a] 5σ limit in a $0.2''$ radius aperture

the central pointing to place different pixels on the same objects and to fully cover the UVIS chip gap. The 5σ depths measured in a $0.2''$ radius aperture are given in Table 3.1.

In order to identify the LBGs at $z \sim 2$, we also used the existing *HST*/ACS images in optical bands (F475W, F625W, F775W, F850LP; PID 9289, PI: H. Ford). Table 3.1 shows the limiting magnitudes of these observations. The overlapping area between the ACS/WFC and WFC3/UVIS fields of view, after subtracting the areas contaminated by the bright cluster galaxies, covers 6.56 arcmin^2 in the image plane.

2.2.1 Data Reduction

The calibrated, flat fielded WFC3/UVIS and ACS/WFC images were processed with *MultiDrizzle* (Koekemoer et al., 2003), part of the STSDAS/DITHER IRAF package (Tody, 1986). The initial drizzled images were registered to SDSS images in order to compute the shift file required for astrometric correction. Because each visit has a slightly different pointing and small differences in rotation and alignment, we make a shift file for each visit to project all the images to the same astrometric reference grid.

The F336W image was aligned with the SDSS g′-band image with a precision of $0.1''$, using unsaturated stars and compact objects. We chose to use the UVIS F336W image to align with SDSS because many of the stars were not saturated at these wavelengths and the galaxies were generally more compact, resulting in more precise alignment.

The other *HST* images were matched to F336W to achieve astrometric registration with the SDSS reference frame. The relative alignment of images was done with a precision of

0.1 pixels ($0.004''$) because of its importance in doing matched-aperture photometry in all filters. The shift files were created by running the *geomap* task in IRAF. These shift files were then used as input to re-run *MultiDrizzle*.

The input images to the *MultiDrizzle* software were drizzled onto separate undistorted output frames which were combined later into a median image. The median image was transformed back (blotted) to the original distorted images in order to make the cosmic ray masks. The final output is a registered, undistorted and cosmic ray-rejected image. We also set *MultiDrizzle* to produce an inverse variance weight image to be used for computing uncertainties in the photometry. In order to do matched-aperture photometry for all wavelengths, we set the same output pixel sizes for WFC3/UVIS and ACS/WFC images to $0.04''$. We set the pixfrac, fraction by which the input pixels are shrunk before being drizzled, to 0.8 for ACS/WFC and 1 for WFC3/UVIS images since these pixfrac values were well matched to our output pixel scale.

The sources were detected in the ACS B band image (F475W) using *SExtractor* (Bertin and Arnouts, 1996). The photometry was done by running *SExtractor* in dual image mode using the weight map RMS-MAP generated by *MultiDrizzle*. We used isophotal apertures with detection threshold 1.27σ and minimum area 16 pixels. We ran *SExtractor* with high and low values for the de-blending minimum contrast parameter without changing other parameters in the *SExtractor* configuration file. We were able to detect very faint galaxies as separate objects in the catalog with very low DEBLEND-MINCONT=0.005 and then add them to the other catalog produced with the larger DEBLEND-MINCONT =0.13 parameter. This method is similar to hot and cold detections used in Rix et al. (2004). All of the isophotal magnitudes are given in AB magnitudes by using the WFC3 and ACS photometric zero points provided by STScI.

The output *SExtractor* uncertainties don't include the correlations between pixel counts that result from combing the input images with *MultiDrizzle*. Following Casertano et al. (2000) paper, the correction factor ($\sqrt{F_A}$) which is approximately the ratio of uncorrelated noise to correlated error from *SExtractor*, can be estimated as below:

$$\sqrt{F_A} = \begin{cases} \frac{s}{p}(1 - \frac{1}{3}\frac{s}{p}) & s < p \\ 1 - \frac{1}{3}\frac{p}{s} & s > p \end{cases} \tag{2.1}$$

where p is the pixfrac and s is the ratio of output pixel size to original pixel size.

We also supplemented our WFC3/UVIS and ACS/WFC images with WFC3/IR data, in order to compute the photometric redshifts. The higher resolution near-UV and optical images were convolved with Gaussians to degrade the resolution to that of the WFC3/IR images. The photometry was then measured using matched apertures in all images.

2.3 Color Selection and Sample

With our near-UV images we apply the Lyman break selection of $z \sim 2$ galaxies, allowing for direct comparison with $z \geq 3$ studies. The selection region is defined by the location of star-forming SEDs in color-color space. Our selection criteria, which are shown in Figure 2.1, were found by running Bruzual and Charlot (2003) (hearafter BC03) models with constant star formation for 100 Myr, reddened by applying Calzetti attenuation curve (Calzetti et al., 2000) with $E(B-V) = \{0, 0.1, 0.2, 0.3\}$ (in magnitudes) and IGM obscuration from Madau (1995). The green dashed line is the track of lower redshift elliptical galaxies which is

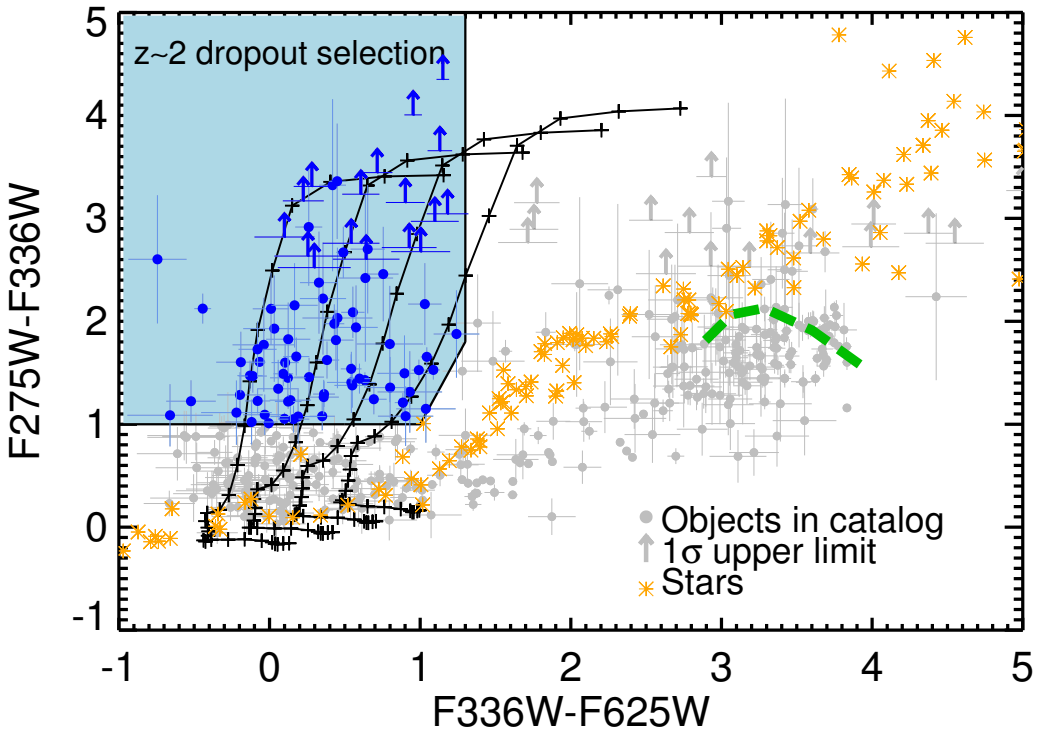

Figure 2.1: Color selection of $z \sim 2$ Lyman-break galaxies (F275W-dropouts). Grey dots are objects detected at greater than 5σ significance in F336W and F625W filters. Grey arrows represent 1σ upper limits. Black lines are tracks of star-forming galaxies that are dust obscured with E(B-V)={0, 0.1, 0.2, 0.3} (in magnitudes). Orange asterisks are stars from Pickles (1998). The blue shaded region is the region selected by the criteria given in Equation 2.2. The blue circles and blue arrows indicate our candidates. The green dashed line is the expected color track for lower redshift ($0.0 < z < 0.2$) elliptical galaxies (Coleman et al., 1980). Abell 1689 is at $z = 0.18$. The large number of redder galaxies (in both colors) are primarily galaxies in Abell 1689.

extended to $z = 0.2$, as Abell 1689 is at $z = 0.18$. Our color selection criteria for selecting the F275W dropouts are:

$$\begin{aligned} & F275W - F336W > 1 \\ & F336W - F625W < 1.3 \\ & F275W - F336W > 2.67(F336W - F625W) - 1.67 \\ & S/N(F336W) > 5 \quad , \quad S/N(F625W) > 5 \end{aligned} \tag{2.2}$$

We found 84 candidates using these criteria. Four candidates were dismissed as they were fainter than the limiting magnitude in Table 3.1 (F336W=27.9 mag and F625W=28.29 mag). Because of the strong lensing phenomenon, many of the candidates in our sample are multiply imaged. In order to compute the luminosity function, we must remove all but one of the multiple images from our catalog. We removed all of the previously known multiple images (12) except the brightest image in each system. In addition to these confirmed multiple images, the Abell 1689 mass model predicts all of the possible counterimages for each object as a function of redshift. Using these predictions, we found eight new multiple images by performing a visual inspection considering the photometric redshift of each object (A. Dominguez et al., in preparation, also see Subsection 2.4.3). We removed two objects with photometric redshifts less than 1.3. Our final sample consists of 58 $z \sim 2$ LBG candidates (see Section 3.7).

The purity of our sample is quite high because of two main reasons. First, the possible contamination from other sources (e.g, stars) can be recognized easily, because these images are high resolution. Second, since these galaxies are UV dropouts, it is very unlikely to have any other break except Lyman break in the UV band. However the contamination from similar galaxies (LBGs) at slightly either higher or lower redshifts, is not negligible. We account for these possible contaminants in our completeness simulation (see Subsection 2.4.3).

The selected Lyman break galaxies have observed B-band magnitude down to $m_{F475W} <$ 27.5 mag, but are intrinsically fainter as they are all highly magnified. The lensing clus-

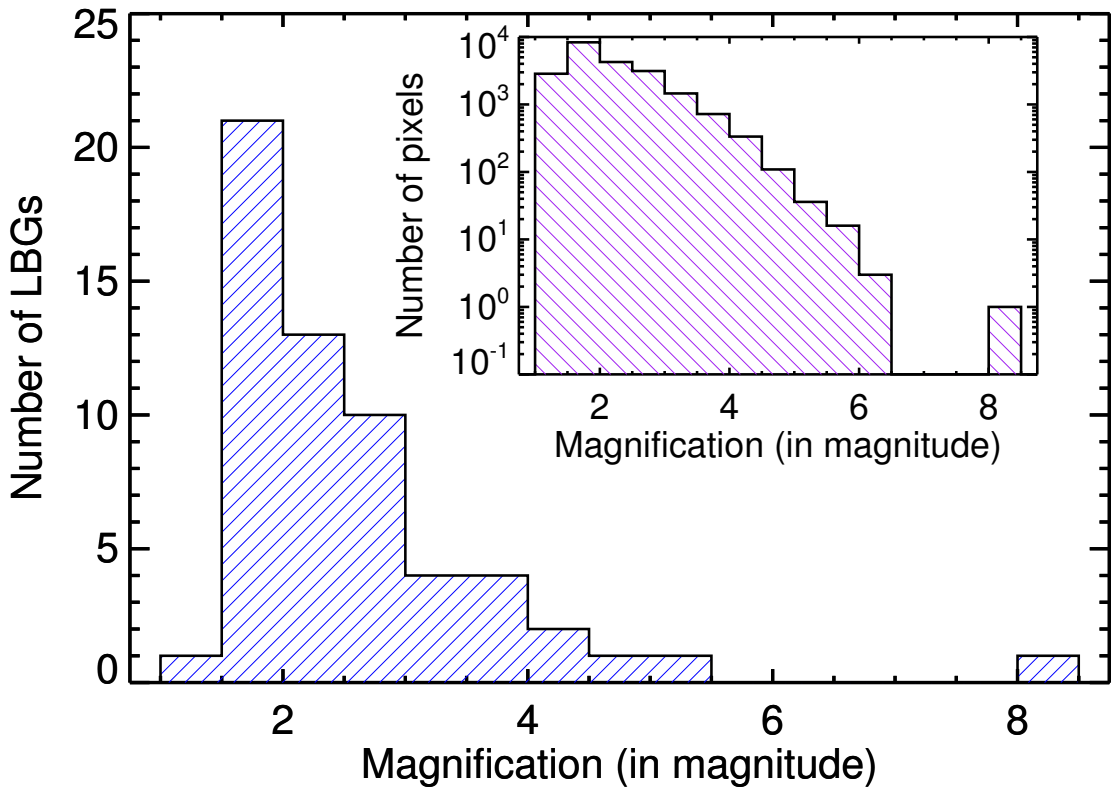

Figure 2.2: The magnification distribution function of Lyman-break galaxies. The magnification values are from the cluster lens model assuming the spectroscopic redshifts for 12 objects (see Subsection 2.4.3) and an average redshift of $z = 2$ (see Subsection 2.4.3) for the rest of the LBGs. The inset shows the distribution function of magnification values over all field of view pixels which are projected on the source plane at $z = 2$.

ter mass model estimates the magnification value at each point of the image as a function of redshift. The magnification of each LBG was measured by assuming the spectroscopic redshifts for 12 out of 58 LBGs (see Subsection 2.4.3) and an average of $z = 2$ (see Subsection 3.7) for the rest of the sample. Figure 2.2 shows the distribution of magnification in magnitude units for all the UV-dropout galaxies. The fluxes are on average magnified by a factor of 10 (2.5 magnitude) and for some galaxies the magnification becomes very large (up to 8 magnitude). The distribution of magnification over the whole field of view in the source plane at $z = 2$ is given in Figure 2.2 (inset), which shows all the pixels in this area are magnified by at least one magnitude.

Due to the large magnifications, the intrinsic absolute magnitudes measured at rest frame 1500 Å, M_{1500}, probed in this study go down to very faint magnitudes ($M_{1500} < -13$ mag), about 100 times fainter than previous studies ($M_{1500} < -18$ mag) at the same redshift (Reddy and Steidel, 2009; Hathi et al., 2010; Oesch et al., 2010a; Sawicki and Thompson, 2006). The intrinsic absolute magnitudes corrected for magnification (M_{1500}) versus observed B-band magnitudes (F475W) are plotted in Figure 2.3. The Dashed lines represent the fixed magnifications of 3, 10 and 30 in flux density units. There are 39 galaxies within the blue box which are both intrinsically very faint ($M_{1500} > -18$ mag) and bright enough ($m_{F475W} < 26.5$ mag) due to magnification to get ground-based spectroscopy in the rest-frame UV and optical bands.

2.4 Completeness

The completeness correction factor $C(z, m, \mu)$ is the probability that a galaxy at redshift, z, with intrinsic apparent magnitude, m, and magnification, μ, will be detected in our magnitude limited sample and also satisfy our color selection criteria. The completeness is affected by several factors: intrinsic luminosity, dust extinction, magnification, size and IGM opacity. In the subsequent subsections, we will describe how these quantities vary and how these variations are implemented in the completeness simulations.

2.4.1 Simulating the Faint Galaxies

We used BC03 models to generate a template spectrum by assuming a Chabrier initial mass function, constant star formation rate, 0.2 $Z_{\odot}$ metallicity, and an age of 100 Myr. Both Salpeter (Salpeter, 1955) and Chabrier (Chabrier, 2003) initial mass functions roughly follow the same power law for stars with $M > 1M_{\odot}$. However at smaller masses there are significant differences. This results in different stellar mass determinations, while having little effect on the ultraviolet spectral energy distributions.

We choose to use a somewhat younger, 100 Myr, stellar population (Haberzettl et al., 2012; Hathi et al., 2013) than is typically used at these redshifts for star forming galaxies ($\sim$ 300 Myr, e.g. Shapley et al., 2005; Reddy et al., 2008) as the target galaxies are typically smaller and have shorter dynamical timescales than their more massive counterparts. The SEDs don't change significantly for stellar ages between 100 Myr and 300 Myr (Leitherer et al., 1999), therefore our assumption for the age does not have a large effect on our main results (see Section 2.6). We will present the ages from SED fitting in a future paper (A. Dominguez et al., in preparation). The star formation histories are undoubtedly more complicated than the assumed constant rate, but the ultraviolet SED reacts slowly (on timescales of 50 Myr) to sudden changes (Leitherer et al., 1999) and smooths out the effects of small timescale star formation events.

Our galaxies have low stellar masses ($7 < \log(M/M_{\odot}) < 9$; A. Dominguez et al., in preparation). Applying the mass-metallicity relation at these redshifts (Erb et al., 2006; Fynbo et al., 2008; Belli et al., 2013; Yuan et al., 2013) to these galaxies gives a lower value than is typically assumed in similar studies which are based on brighter galaxies (0.2 vs 1 $Z_{\odot}$).

The Calzetti attenuation curve (Calzetti et al., 2000) was used for the dust extinction by assuming a Gaussian distribution for $E(B-V)$ centered at 0.14 mag (Steidel et al., 1999; Hathi et al., 2013) with a standard deviation of 0.1.

We also estimated the completeness for the typical stellar population assumptions (300Myr and $1Z_{\odot}$) and again a Gaussian distribution for $E(B-V)$ centered at a value lower than 0.14 mag (0.05 mag, see Section 2.6) to see if varying the input stellar population parameters changes the results significantly. Our completeness determinations are robust against these initial considerations.

2.4.2 Monte Carlo Simulation : IGM Opacity

Ultraviolet (both Lyman emission line and continuum) photons are absorbed by neutral hydrogen clouds located along the line-of-sight to any galaxy. These intervening absorbers

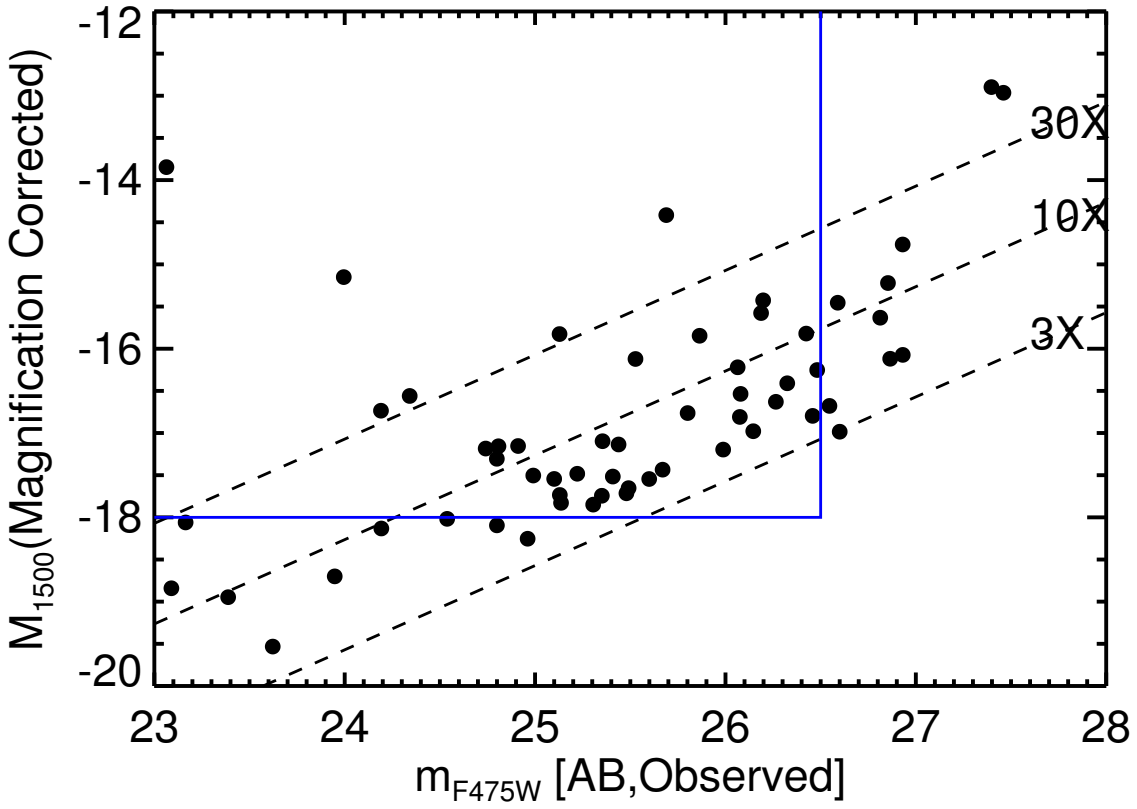

Figure 2.3: The intrinsic absolute magnitude, corrected for magnification, is plotted vs. observed B-band magnitude. There are 39 LBGs in the blue box which denotes galaxies that are both intrinsically faint ($M_{1500} > -18$) *and* bright enough ($B < 26.5$) for follow-up ground-based spectroscopy. Dashed lines show constant magnifications (3, 10 and 30 in flux density units)

are classified in three groups based on their hydrogen column densities : Lyman-α forest (10^{12} cm$^{-2} < N_H < 10^{17.5}$ cm^{-2}), Lyman limit systems (LLSs, $10^{17.5}$ cm$^{-2} < N_H < 10^{20.3}$ cm^{-2}) and damped Lyman-α systems (DLAs, $N_H > 10^{20.3}$ cm^{-2}). The column density distribution of these absorption clouds is given as

$$\frac{df}{dN_H} \propto N_H^{-k} \tag{2.3}$$

and their number density distribution (number per unit redshift) changes as a power law with redshift.

$$N(z) = N_0(1+z)^{\gamma} \tag{2.4}$$

Where N_0 is the number of absorbers per unit redshift at present time (z = 0). The values we have adopted (from the literature) for k, N_0 and γ are given in Table 2.2 (Janknecht et al., 2006; Rao et al., 2006; Ribaudo et al., 2011; O'Meara et al., 2013)

The IGM opacity at each line-of-sight is computed by running a Monte Carlo simulation. A complete description of this simulation is presented in Siana et al. (2008a). Here we briefly summarize how the IGM absorption code works.

We randomly vary the number of absorbers along the line of sight to each galaxy by sampling from a Poisson distribution with the expectation value $< N >$.

$$< N >= \int_0^{z_{\rm galaxy}} N(z)dz \tag{2.5}$$

We then select a column density and redshift for the absorber from the distributions in Equations 2.4 and 2.5, respectively. We determine the Voigt profile with doppler parameters given in Table 2.2, for the first twenty Lyman lines for each absorber. Finally, the IGM transmission for non-ionizing UV wavelengths at each line of sight is derived by adding the optical depths of randomly selected absorbers. We also incorporate the opacity to Lyman continuum photons using a photo-ionization cross section of $\sigma = 6.3 \times 10^{-18}$ cm^2 and decreasing as λ^3 for $\lambda < 912$ Å. We generated 1000 lines-of-sight at each redshift in steps of

Table 2.2. IGM Parameters

Name	$\log(N_H)$	k[a]	N_0[b]	γ[b]	b (km s^{-1})[c]	redshift[b]
Lyman-α forest	12 - 14	1.67	50.12	1.18	30	$1.9 \leq z$
			62.52	0.78	30	$z < 1.9$
	14 - 17.5	1.67	6.02	2.47	30	$1.9 \leq z$
			16.98	1.66	30	$0.7 \leq z < 1.9$
			35.4	0.13	30	$z < 0.7$
Lyman limit system (LLS)	17.5 - 20.3	1.07	0.17	1.33	70	$z < 2.6$
Damped Lyman-α system (DLA)	20.3 - 21.5	1.71	0.04	1.27	70	$z < 5$
	21.5 - 22	11.1	0.04	1.27	70	$z < 5$

[a]The values are taken from O'Meara et al. (2013)

[b]The column density distribution parameters N_0 and γ are from Janknecht et al. (2006); Ribaudo et al. (2011); Rao et al. (2006) for Lyman-α forests, LLSs and DLAs , respectively.

[c]The doppler parameter values are from Kim et al. (1997) and Moller and Jakobsen (1990)

$\Delta z = 0.1$ over the required redshift range for the completeness simulation ($1 < z < 3$, see Section 2.4.3).

2.4.3 Simulation: Incompleteness Correction

We created a 3-D grid to compute the completeness as a function of redshift z, magnitude m and magnification μ. For each point in this 3-D space, the SED generated by BC03 was redshifted, magnified and then attenuated by the IGM for 300 randomly selected line-of-sights. At each line-of-sight, the dust attenuation is sampled randomly from the Gaussian distribution mentioned above.

As was mentioned before (see Section 2.3), the primary contaminants in our sample are similar galaxies (LBGs) at slightly higher or lower redshifts. The photometric uncertainties can scatter the galaxies both into and out of the selection region. Adding these to the completeness simulation effectively broadens the redshift distribution of our sample. The photometric uncertainties are assumed to have a Gaussian distribution with $\sigma \propto \sqrt{\text{area}}$ (assuming a constant instrumental noise over the object's area). We assume a normal

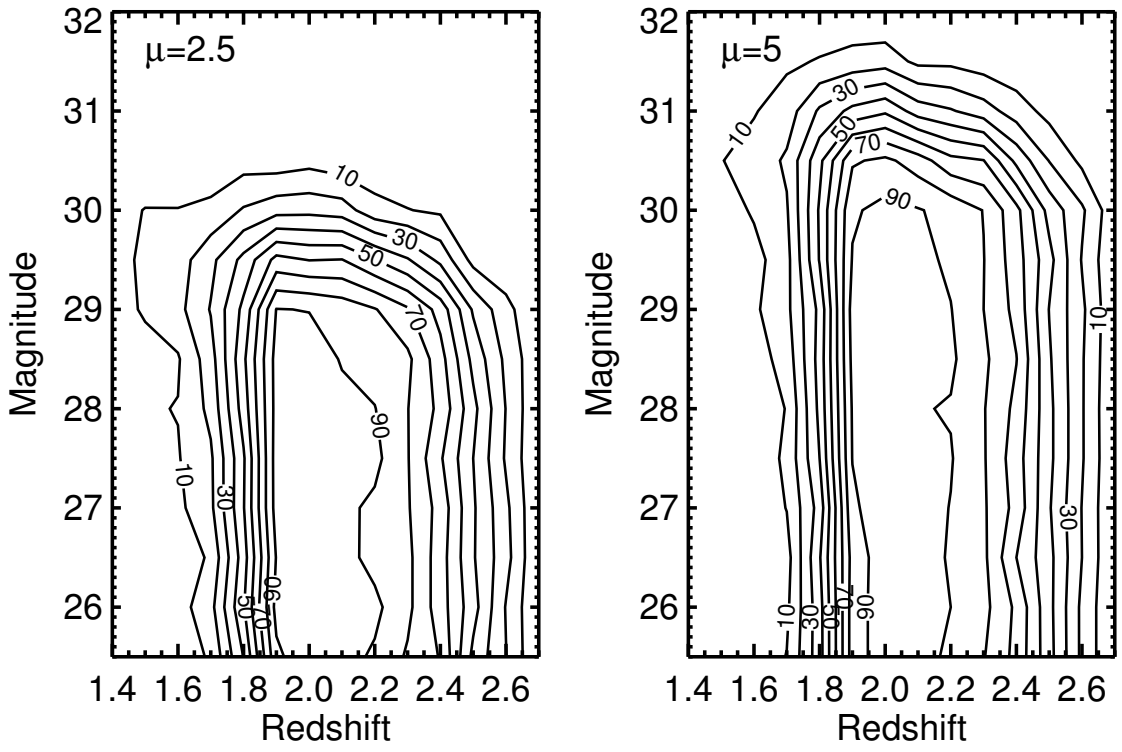

Figure 2.4: The completeness contours as a function of intrinsic F475W apparent magnitude and redshifts. The contours are plotted for two values of magnification, μ=2.5 mags (left, the typical magnification) and $\mu = 5$ mags (right, an extreme magnification in our sample).

distribution for the galaxy sizes centered at 0.7 kpc (Law et al., 2012) with σ=0.2 kpc. At each line-of-sight, the randomly selected area is magnified by the magnification factor.

There is another important factor which can affect our completeness simulation. Charge transfer inefficiency (CTI) causes some signal to be lost during the readout. The CTI depends on the flux density of the object, sky background, the distance on the detector between the object and the readout amplifier and the time of the observation (e.g. as the CTI worsens with time, Baggett et al., 2012; Teplitz et al., 2013). This problem is more significant for images with very low background similar to our images in the F275W band ($\sim$ 0.5 e^-, Teplitz et al., 2013). Therefore CTI associated charge loses would make some galaxies fainter in the F275W band and push them inside the color selection region. We consider this issue in our completeness computations based on the analysis done in Noeske et al. (2012) . The CTI is estimated as follows:

$$\mathrm{m_{(corr)}} = \mathrm{m_{(uncorr)}} - \mathrm{S}\frac{\mathrm{Y}}{2048} \tag{2.6}$$

where Y is the distance in rows between the simulated galaxy and readout amplifier. For each line-of-sight, Y is randomly selected from a uniform distribution. S is a 2nd degree polynomial function of flux and observation date. More information related to the estimation of CTI is given in Noeske et al. (2012). The CTI corrections are small for most of the F275W-detected objects ($<$ 0.1 mag), therefore they do not have a significant effect on the completeness results. In Section 2.4.4, we discuss about the possibility that CTI causes galaxies to be undetected in the F275W filter.

Therefore, at each point in the 3D grid (z, m, μ), we simulate 300 galaxies at different lines of sight with different reddening, distance from readout amplifier and noise (size) selected from the related distributions mentioned above. The completeness was computed by counting the fraction of galaxies that satisfy the same selection criteria as the real observed objects (Equation 2.2)

The completeness contours are given in Figure 2.4. The contours are plotted for two different values of magnification, $\mu = 2.5$ and $\mu = 5$ in units of magnitude which are the average and maximum predicted magnifications by the mass model for the LBG candidates in the sample. The figure indicates that the completeness as a function of absolute magnitude is obviously dependent upon the magnification. The color selection criteria represented in Section 2.3 is more than 90% complete between $1.9 < z < 2.1$.

As a test of the completeness simulation, we compare to the completeness of our selection of LBGs from a parent sample of galaxies with spectroscopic redshifts. The spectroscopic redshifts are discussed in J. Richard et al. 2013 (in preparation) and D. Stark et al. (in preparation). These spectroscopic campaigns have targeted primarily galaxies with high magnification (arcs) so many of the galaxies are intrinsically faint. In the core of the lensing cluster, we have targeted multiply imaged systems. Because the multiple systems are important for modeling the mass distribution of the cluster, they were targeted down to very faint magnitudes ($m_{475} \sim 27.0$). Therefore the final spectroscopic sample is less biased toward luminous galaxies than it would be in a blank field without magnification. In the outskirts of the cluster, where the magnification is lower, spectra were obtained for a variety of galaxies.

Figure 2.5 shows the redshift distribution of all 57 objects with spectroscopic redshifts in the field together with the subsample selected as LBGs. A few over densities are seen at z=1.83 and z=2.54. The dashed line is the completeness distribution for a galaxy with typical intrinsic apparent magnitude ($m_{F475W} = 27.5$) and magnification ($\mu = 2.5$ mag). We detected 75% of the galaxies in the redshift range, ($1.8 < z < 2.4$), consistent with our completeness calculations. The simulated completeness values are given at right-hand axis. The tail in the dashed line seen at lower redshifts shows the contamination from lower redshift galaxies (see Section 2.3). This effect slightly broadens the redshift distribution of our sample, and is accounted for in the completeness simulation.

We see that the observed completeness, ratio of these two spectroscopic redshift histograms at each bin, is in good agreement with the corresponding simulated completeness

value (dashed line). Predicting a high value of simulated completeness in the redshift bin $1.9 < z < 2$, we might expect to have more than one LBG out of three at this redshift interval. One of the objects was not selected because it is not a 5σ detection in F336W.

subsectionRedshift Distribution

In order to determine luminosities and magnifications, we need to know the mean redshift of galaxies in our sample (and its dispersion). From our completeness function (Figure 2.4), if we assume that there is no strong evolution of number density with redshift, we would expect the average redshift of the sample to be between $2.0 \lesssim z \lesssim 2.1$. Given the unknown number density evolution and the possibility of structure along the line-of-sight, we determine the average redshift of the sample from both the spectroscopic and photometric redshifts.

From the 12 galaxies with spectroscopic redshift, we obtain an average redshift, $< z >= 1.98$ with a dispersion of $\sigma_z = 0.30$, in agreement with the completeness simulations.

To obtain a larger sample of redshifts, we calculated photometric redshifts for a sample of 26 galaxies that lie within the WFC3/IR image footprint. These photometric redshifts should be more precise because of the addition of the near-IR data, which span the Balmer/4000Å break at $z \sim 2$. We used the EAZY code (Brammer et al., 2008) to determine photometric redshifts of our eight *HST* band (UV,optical and IR) catalogs. We compare the photometric and spectroscopic redshifts (6 in this sample) to determine the fractional redshift error, $\Delta = |(z_{phot} - z_{spec})| \ / \ (1 + z_{spec}) = 0.02$. The dispersion of the photometric versus the spectroscopic redshifts shows that there is no bias in our photometric redshift estimates. Figure 2.6 shows the estimated photometric redshift distribution of the 26 candidates that have near-IR photometry. The mean of the photometric redshift distribution is $z = 2.03$ with a dispersion of $\sigma_z = 0.20$, in agreement with what we expect from the completeness simulation.

Given the average and dispersion of our spectroscopic and photometric redshifts, we assume an average redshift $< z >= 2.00$ with a dispersion of $\sigma_z = 0.25$ for LBGs without spectroscopic redshifts. For comparison, the studies of Oesch et al. (2010a) and Hathi

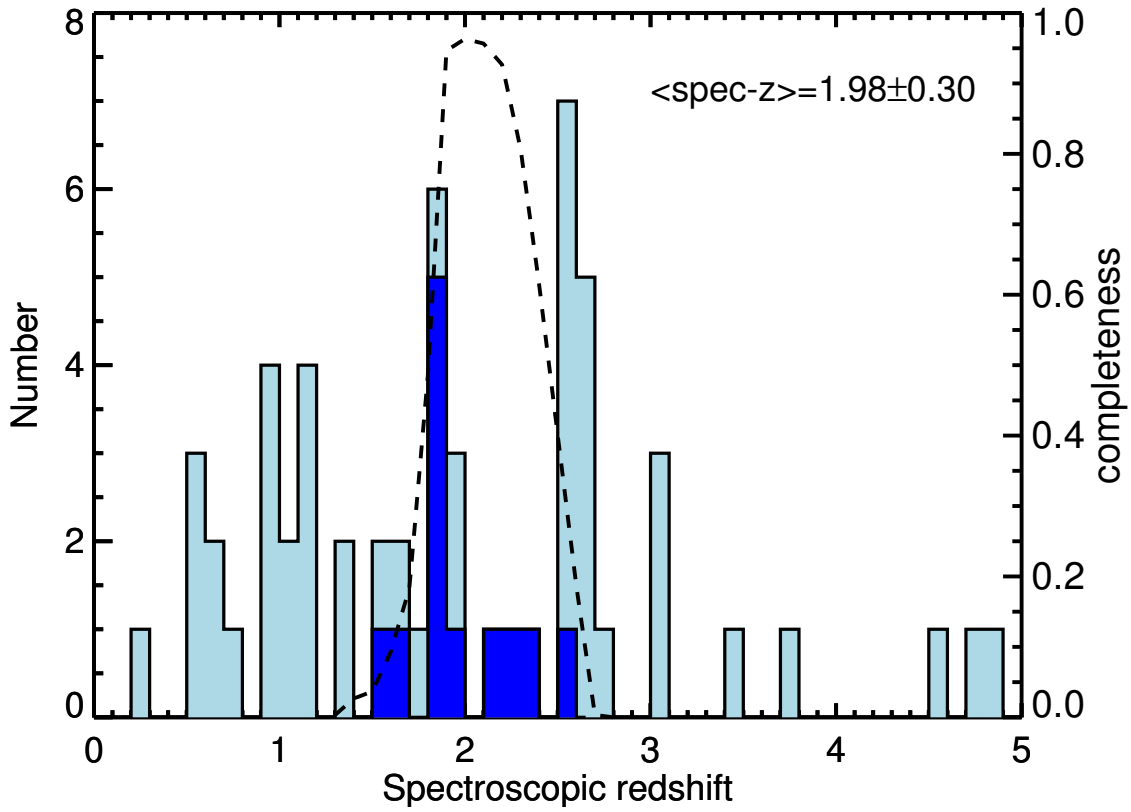

Figure 2.5: The spectroscopic redshift distribution. The redshift histogram for galaxies with spectroscopic redshift is shown in light blue. The dark blue histogram shows the spectroscopic redshift distribution of 12 galaxies selected as $z \sim 2$ LBGs in our image. We recovered 75% (9 of 12) galaxies in the range $1.8 < z < 2.4$ where we should have high selection completeness. A few over densities are evident at $z \sim 1.83$ and $z \sim 2.54$. The right-hand axis shows the completeness values from the simulation. The dashed line shows the simulated completeness distribution over the redshift for a galaxy with typical intrinsic apparent magnitude (m_{F475W}=27.5) and magnification ($\mu = 2.5$ mag).

et al. (2010), using similarly selected samples, assumed average redshifts of 1.9 and 2.1, respectively.

2.4.4 F275W Non-detections and CTI

Our completeness simulations account for the small corrections to F275W magnitudes from CTI. However, one concern is that very faint F275W fluxes near the detection limit will be lost completely due to CTI. Of the final sample of 58 sources, 11 are undetected in F275W. Most of these 11 galaxies are bright in F336W and would have bright F275W

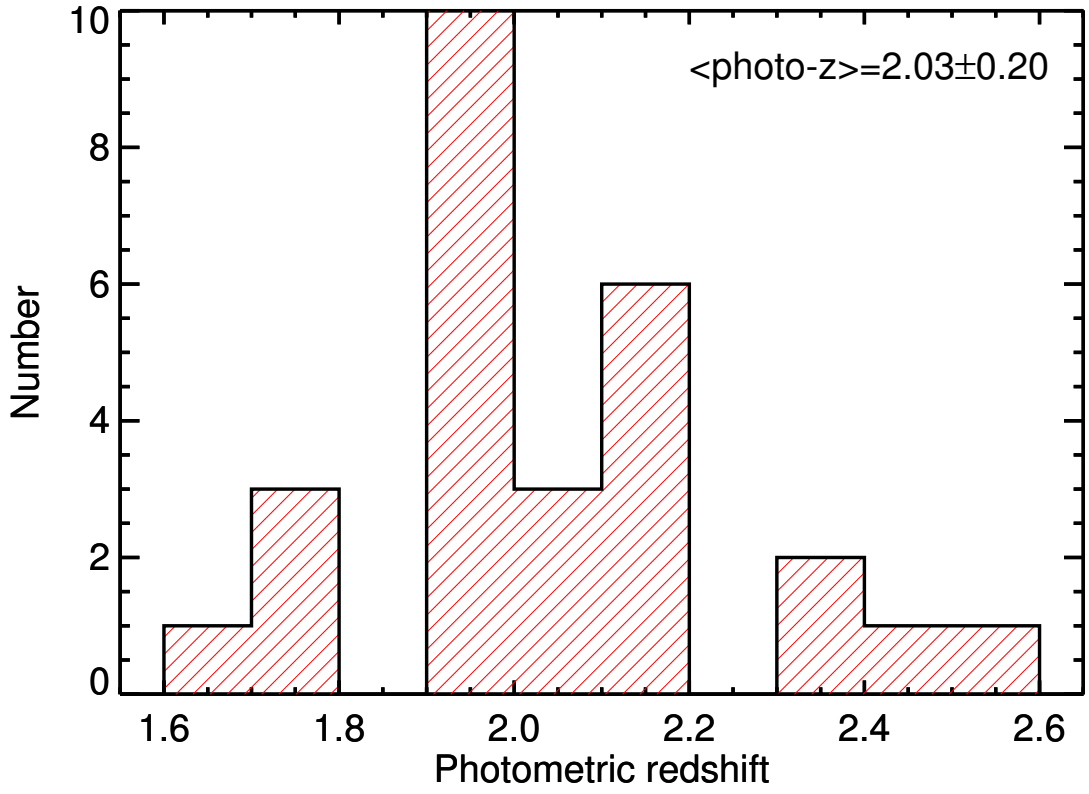

Figure 2.6: The photometric redshift distribution from SED fitting to 8 *HST* bands spanning UV, optical and near-IR wavelengths. The photometric redshift uncertainty is $\Delta = |(z_{phot} - z_{spec})|/(1+z_{spec}) = 0.02$ when comparing to the six galaxies in the sample with spectroscopic redshifts.

magnitudes if they were blue enough to lie outside of our selection window. Therefore, CTI can not be responsible for the non-detection in F275W. However, there are five galaxies with $F336W > 27.0$ mag, meaning that the F275W magnitude of an LBG would have to be fainter than $F275W > 28.0$ mag to be selected as an LBG. For these galaxies, CTI can cause a non-detection if the galaxy is far from the readout amplifier. The galaxies are 422, 1104, 1141, 1604, and 1620 pixels from the read amplifier. It is possible that a few of the galaxies that are far from the amplifier (> 1000 pixels) may be in our sample because of CTI issues. We note however that these galaxies span a range in intrinsic UV magnitudes ($-16.98 < M_{1500} < 15.22$ mag) where there are many galaxies per bin. Therefore, even in the worst case scenario that all four of these galaxies are low-z interlopers, the CTI concerns will not significantly affect the conclusions of this paper.

We are using two orbits of our cycle-20 program to test the effects of CTI in our F275W image and will refine our selection in the future.

2.5 Luminosity Function

The ultraviolet luminosity function at rest-frame 1500 Å is measured by using the spectroscopic redshifts for 12 out of 58 dropout candidates and assuming a mean redshift of 2.0 for the rest of the objects. The absolute magnitudes are computed at 1500 Å by using the apparent magnitude at F475W as below:

$$M_{1500} = m_{F475W} + \mu - 5\log(d_L/10 \text{ pc}) + 2.5\log(1+z) \tag{2.7}$$

Where μ is the magnification in magnitudes predicted by the lens model. The luminosity distribution of galaxies can be parametrized by a Schechter function which has three parameters: faint end slope (α), characteristic luminosity (L^*) and normalization coefficient (ϕ^*).

The accurate approach to fitting the luminosity function is the maximum likelihood method (Sandage et al., 1979) using the individual galaxies and their associated effective

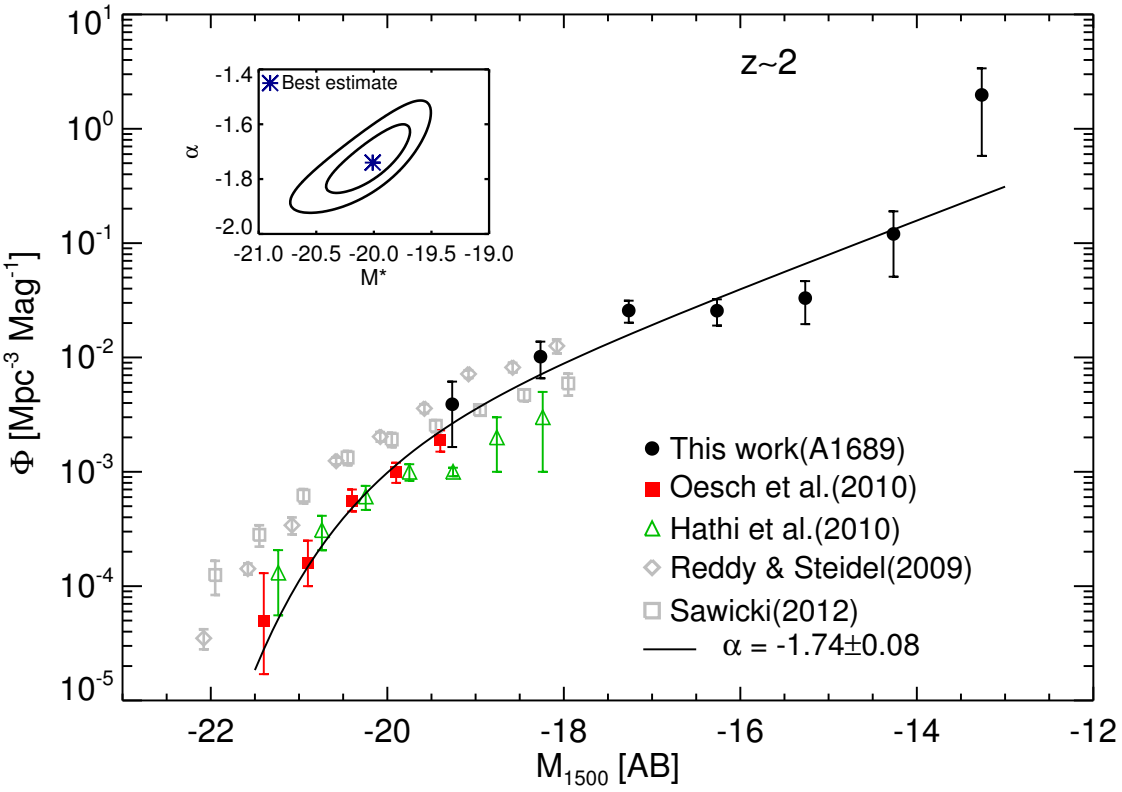

Figure 2.7: The UV luminosity function at z∼2. The black circles are our binned luminosity function values computed by using the Equation 2.14. The red filled squares and the green open triangles are the LFs from Oesch et al. (2010a) and Hathi et al. (2010), respectively, which are selected in a similar manner to our sample and are at the same redshift ($z \sim 2$). Grey open diamonds and grey open squares are the LFs at slightly higher redshift ($z \sim 2.3$) from Reddy and Steidel (2009) and Sawicki (2012), respectively. The black solid line is the best unbinned maximum likelihood fit to the whole sample of our data and Oesch et al. (2010a). The inset shows the 68% (1σ) and 95% (2σ) confidence contours of the Schechter parameters.

volumes. The main advantage of this approach is in using the unbinned data. Fits to binned data are imprecise as the choice of bin size and center effects the results. Furthermore, the completeness and the effective volume can change significantly from one side of the bin to the other.

In addition to using our data in the maximum likelihood fitting process, we used the individual data points from Oesch et al. (2010a) $z = 1.9$ sample as well. Their sample includes the rare, bright galaxies which are not present in our small survey volume, but are necessary to constrain L^*.

The probability that a galaxy with absolute magnitude M_i is detected in our magnitude limited sample is :

$$P(M_i) = \frac{\phi(M_i)V_{\rm eff}(M_i)}{\int_{-\infty}^{M_{\rm limit}} \phi(M)V_{\rm eff}(M)\mathrm{d}M} \tag{2.8}$$

Where ϕ is the parametric luminosity function and M_{limit} is the faintest intrinsic absolute magnitude in the sample. $V_{\rm eff}$ is the effective comoving volume in which a galaxy with magnitude M can be found. The effective volume associated with each galaxy in our sample is derived by taking incompleteness into account,

$$V_{\rm eff} = \int_{\mu>\mu_0} \int_0^\infty \frac{dV_{com}}{dzd\Omega} C(z, m, \mu)\Omega(\mu)\mathrm{d}z\mathrm{d}\mu \tag{2.9}$$

where $\mathrm{V_{com}}$ and Ω are the comoving volume and solid angle, respectively. $\Omega(\mu)$ is an area in the source plane that is magnified by a factor of μ. Due to the distortion generated by gravitational lensing, the total effective area in the source plane is 0.37 arcmin^2 at $z \sim 2$ which is significantly smaller than the total area in the image plane. μ_0 is the minimum magnification needed for detecting an object with magnitude M relative to the magnitude limit. $C(z, m, \mu)$ is the completeness computed in Section 3.7.

The best fit to the luminosity function was found by maximizing the joint likelihood $\mathcal{L}$, which is the product of individual probabilities taken at all (unbinned) data points of the sample.

$$\mathcal{L} = \prod_{i=1}^{N} P(M_i) \tag{2.10}$$

where N is the total number of objects in both samples (Abell 1689 and Oesch et al. (2010a)). In this method the normalization coefficient is cancelled out so it must be estimated separately from the number counts.

$$\phi^* = \frac{N}{\int_{M_1}^{M_2} \phi(M) V_{\text{eff}}(M) \mathrm{d}M} \tag{2.11}$$

Where M_1 and M_2 represent the brightest and faintest candidates in the sample, respectively.

There are three sources of uncertainty in the determination of the intrinsic absolute magnitudes for *our* sample. First, we do not know the redshift of most galaxies (except those with spectroscopic redshifts, Section 2.4.3), so the conversion from apparent to absolute magnitude is uncertain. We used the completeness computations given in Section 2.4.3 (Figure 2.4) to estimate the standard deviation of the redshift distribution, $\Delta z = 0.25$, which is consistent with the photometric and spectroscopic redshift distributions. Using this $\Delta z = 0.25$, we derive an absolute magnitude uncertainty of $\sigma_z = 0.24$ magnitudes. Second, again due to the unknown source redshift, the magnification estimate from the mass model is uncertain. Using the same redshift uncertainty, $\Delta z = 0.25$, we find a $\sigma_\mu = 0.10$ magnitudes. The third uncertainty is from the Abell 1689 lens model, σ_{model}. Limousin et al. (2007) has used a parametric method to describe the mass distribution of Abell 1689. In this parametric approach, they utilize the observational constraints (multiply imaged systems) to optimize the parameters (minimum χ^2) of the lens model (see Limousin et al., 2007, Equation 3). We computed the lens model uncertainty by producing a series of models through sampling the parameter space around a similar χ^2 as the best model. We used a Bayesian Markov Chain

Monte Carlo sampler in Lenstool (Jullo et al., 2007). The mean and the median values of this uncertainty are 0.08 and 0.04 mags, respectively.

The total absolute magnitude uncertainty, σ, for the objects with spectroscopic redshift is simply $\sigma_{\rm model}$. Because the effect of luminosity distance and magnification when varying the redshift are correlated, they change the absolute magnitude in the same way. Therefore, σ for the rest of the objects is computed by summing the first two uncertainties, σ_z and σ_μ, and then adding the lensing model uncertainty in quadrature. This uncertainty in the absolute magnitude measurement is incorporated into the analysis by marginalizing over the probability distribution of each object's magnitude. The conditional probability that a galaxy with magnitude M_i is in the sample, given the total uncertainty (σ_i) can be estimated through marginalization,

$$P(M_i|\alpha,\sigma_i) = \int_{-\infty}^{\infty} P(M_i|\mu,\alpha,\sigma_i)P(\mu|\sigma_i)\mathrm{d}\mu \tag{2.12}$$

where $P(M_i \mid \mu,\alpha,\sigma_i)$ is the Schechter function at magnitude M_i. The probability of each magnification measurement is given by a normal distribution,

$$P(\mu|\sigma_i) = \frac{1}{\sqrt{2\pi}\sigma_i} e^{\frac{-(\mu-\mu_i)^2}{2\sigma_i^2}} \tag{2.13}$$

where the mean value, μ_i, is the magnification assigned to each candidate by using the ratio of source and image plane luminosities from the Abell 1689 mass model (Limousin et al., 2007) and assuming an average redshift $z = 2$ for all of the objects.

Figure 3.7 shows the best-fit luminosity function derived from the maximum likelihood method along with previous determinations (Reddy and Steidel, 2009; Hathi et al., 2010; Oesch et al., 2010a; Sawicki, 2012). The inset shows the 68% and 95% likelihood contours of the Schechter parameters. In order to display our data better (black filled circles in Figure 3.7), we defined the absolute magnitude bins and then calculated the luminosity function over these bins as below:

$$\phi(M_i)dM_i = \frac{N_i}{V_{\rm eff}(M_i)} \tag{2.14}$$

Table 2.3. UV Luminosity Function Parameters

Method	z	α	M*	$\log_{10}\phi^*(\mathrm{Mpc}^{-3}\ \mathrm{mag}^{-1})$
Maximum Likelihood[a]	2.0	-1.74±0.08	-20.01±0.24	-2.54±0.15

[a]Maximum likelihood fit to the whole sample including both this work (Abell 1689) and Oesch et al. (2010a)

Where N_i is the number of galaxies in magnitude bin i and V_{eff} is the effective comoving volume computed in Equation 2.9. We emphasize that we fit to individual points and not the binned data.

We examined the convergence of the completeness simulation by splitting the simulation in half (150 line-of-sights each). We then re-ran the simulation code and re-fit the luminosity function parameters using the maximum likelihood approach. The difference between the new estimates of each Schechter parameter and what we found before, is less than 4% of the previously determined uncertainty of each parameter. We conclude that our simulation has converged for the adopted number of line-of-sights (300, see Section 3.7).

2.5.1 Cosmic Variance

The cosmic variance uncertainty σ_{CV} in the galaxy number counts can be estimated through the effective volume of the survey, the survey geometry, and an estimate of the typical clustering bias of the discovered sources. In what follows, we compute the cosmic variance uncertainty for the lensed field.

The effective volume of our survey has been calculated using the methods described in Section 2.5. We use these effective volumes and the selection function of the survey with redshift to determine the root-mean-squared (RMS) density fluctuations σ_ρ expected in our survey volume given its pencil beam geometry, following the methodolgy of Robertson (2010). We find these density fluctuations to be $\sigma_\rho \approx 0.1$, which is determined largely by the line-of-sight extent of the pencil beam survey (the comoving radial distance over the

redshift range $1.75 \leq z \leq 2.35$ where our selection is efficient) and the linear growth factor $D(z \sim 2) \approx 0.4$ (Robertson et al., 2013).

To determine the cosmic variance uncertainty in the galaxy counts, we perform a simple abundance matching calculation (e.g., Conroy et al., 2006; Conroy and Wechsler, 2009) assigning galaxies in our survey approximate halo masses and clustering bias based on their volume abundances. For galaxies in our survey, the estimated bias is $b \sim 1.2-2.6$, providing a cosmic variance uncertainty of $\sigma_{\rm CV} \approx 0.12-0.25$ (e.g., Robertson, 2010), comparable to our fractional Poisson uncertainty $1/\sqrt{N} \approx 0.13$. We therefore expect that cosmic variance does not strongly influence the luminosity function results. Further, since cosmic variance instills a covariance in the galaxy number counts as a function of luminosity (see, e.g., Robertson, 2010), if our survey probes either an over- or under-dense region compared to the cosmic mean the covariance in the counts should have little effect on the intrinsic shape of the luminosity function (especially at faint magnitudes where the galaxies are nearly unbiased tracers of the dark matter). Our faint-end slope determination is therefore expected to be robust against systematic considerations owing to cosmic variance uncertainties.

2.6 UV Spectral Slope

The ultraviolet continuum of galaxies can be approximated as a power law, $f_\lambda \propto \lambda^\beta$ (Calzetti et al., 1994). The UV spectral slope, β, of each galaxy in our sample was estimated by making fake power law spectra over a wide range of β values and multiplying these spectra with the filter curves. We then have a one-to-one map of the observed color to the spectral slope. We use the F475W and F625W filters to measure the UV spectral slope as they correspond to rest-frame wavelengths of ~ 1580 Å and ~ 2080 Å respectively, at $z \sim 2$. The uncertainty of the β estimate for each individual object was derived by using the photometric uncertainties in both the F475W and F625W filters.

The $E(B-V)$ values, which have a one to one relation with UV spectral slopes, are obtained based on the comparison of observed UV colors with the colors predicted from

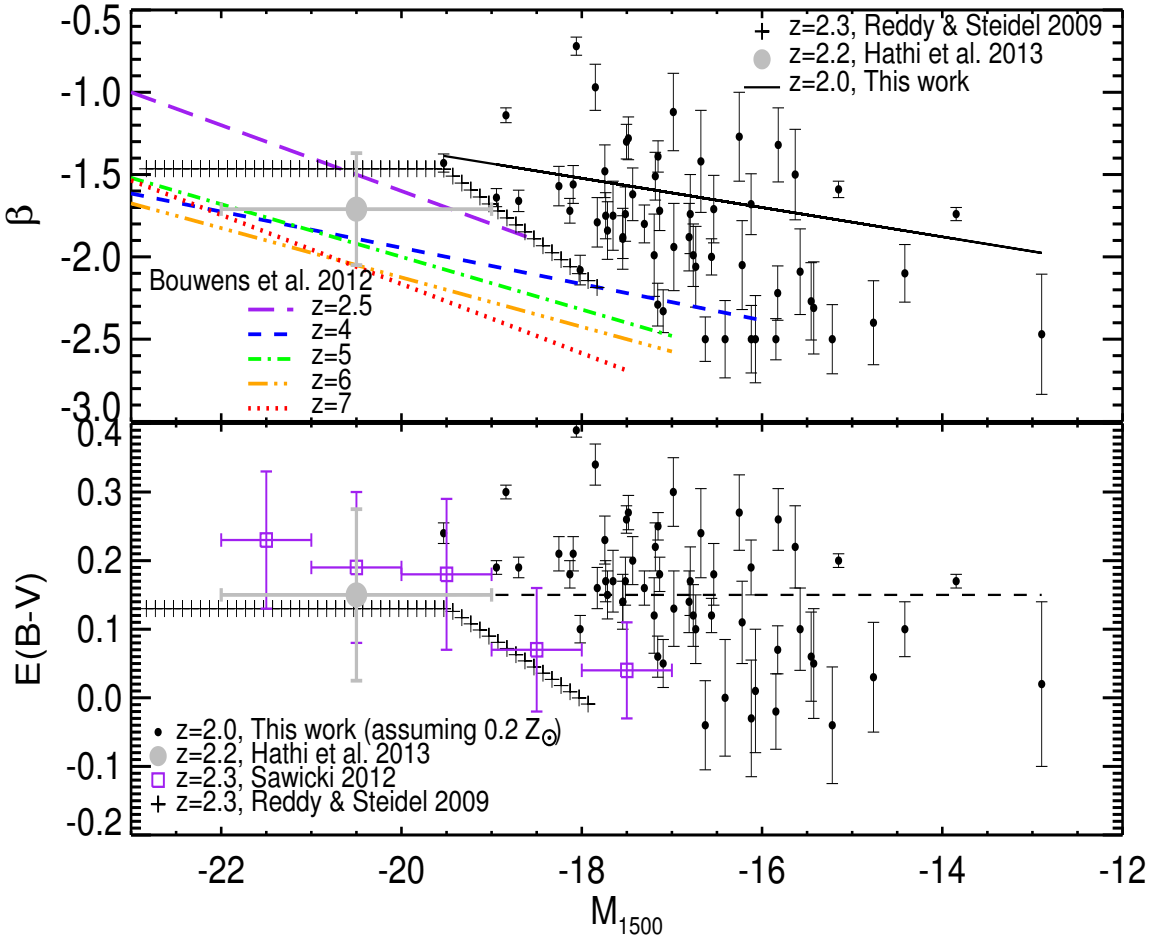

Figure 2.8: Upper panel: UV spectral slope as a function of absolute UV magnitude at 1500 Å. The black solid line is the best linear fit to our individual data. The line made of plus symbols is from Reddy and Steidel (2009) . The purple long dashed, blue dashed, green dot-dash, orange dot-dot-dash and red dotted lines are the best linear fit for redshifts 2.5, 4, 5, 6 and 7 respectively, from Bouwens et al. (2012b). The grey point shows the average and dispersion of values measured by Hathi et al. (2013) at $z \sim 2$. Lower panel: E(B-V) as a function of absolute UV magnitude at 1500 Å . Our reddening values (black filled circles) are computed assuming 0.2 $Z_{\odot}$ but the other E(B-V) values have been found assuming 1 $Z_{\odot}$. The purple open squares are from Sawicki (2012). The rest of the symbols are the same as those in the upper panel. The dashed line is an average of our E(B-V) values and *not* a fit to our data.

the stellar population synthesis model (BC03) and reddened with a Calzetti attenuation curve (Calzetti et al., 2000). We used the realistic assumptions for the age (100 Myr) and the metallicity (0.2 $Z_{\odot}$) of these compact faint galaxies (see Section 2.4.1). In order to compare the importance of the age and metallicity in the color excess measurements, we also estimated the $E(B-V)$ values considering the more typical assumptions for these two quantities (1 $Z_{\odot}$ & 300 Myr). We present the color excess $E(B-V)$ distributions for three sets of age and metallicity assumptions, [(0.2 $Z_{\odot}$ & 100 Myr), (0.2 $Z_{\odot}$ & 300 Myr), (1 $Z_{\odot}$ & 100 Myr)] in Figure 2.10. The black histogram shows the distribution resulting from the realistic assumptions for the age and metallicity (Z = 0.2 $Z_{\odot}$ and age = 100 Myr). We see that varying the assumed metallicity (right panel, blue distribution) dominates the effect on the determined reddening distribution, whereas changing the assumed starburst age has little effect (left panel, red distribution). Therefore, assuming a value of 1 $Z_{\odot}$ would underestimate the dust content of these faint galaxies.

In the upper panel of Figure 2.8 we plot the estimated UV slopes versus absolute UV magnitude at 1500 Å (M_{1500}). The UV spectral slope, β, correlates with the UV magnitude, M_{1500}, such that the less luminous galaxies are bluer. The same trend has been identified in other works at higher redshifts and higher luminosities (Meurer et al., 1999; Labbé et al., 2007; Overzier et al., 2008; Wilkins et al., 2011; Bouwens et al., 2012b). Fitting the estimated β values versus UV luminosities, we find β=(-0.09±0.01)M_{1500}+(-3.1±0.1) for our z∼2 dropout sample. We note that we removed one galaxy from our sample when fitting the reddening distribution as this galaxy had an anomalously high F625W flux. Therefore the derived reddening was quite high, even though the photometry in other bands suggested a blue spectrum.

2.7 Discussion

We have extended the UV luminosity function at $z \sim 2$ to the faintest magnitude limit ever obtained ($M_{1500} \sim -13$ mag), allowing us to put a strong constraint on the ultraviolet

luminosity density at the epoch of peak star formation. In the next few subsections, we will discuss the contribution of faint galaxies to the ultraviolet luminosity and star formation densities at $z \sim 2$. We will also discuss the evolution of the faint-end slope of the luminosity function and dust extinction derived from the UV spectral slope, in comparison with other results from the literature.

2.7.1 Comparison with Other Space Density Measurements at $z \sim 2$

In Figure 3.7, we plot our binned luminosity function with those of Reddy and Steidel (2009); Oesch et al. (2010a); Hathi et al. (2010); Sawicki (2012). We prefer to compare our luminosity function with those of Oesch et al. (2010a) and Hathi et al. (2010), as the galaxies are selected via a Lyman break in the same F275W filter and will therefore have similar redshift distributions. The Reddy and Steidel (2009) and Sawicki (2012) samples are selected with optical data alone and are at a slightly higher average redshift ($z \sim 2.3$). Given the significant evolution in the luminosity function at these redshifts (Oesch et al., 2010a), a direct comparison with the Reddy and Steidel (2009) and Sawicki (2012) data is not ideal but the data are plotted for reference.

If we assume that the faint-end of the luminosity function is truly a power-law, then the fit to that power law suggest an excess of moderately bright galaxies ($M_{1500} \sim -19$ mag) in our sample compared to the measurements of Oesch et al. (2010a) and Hathi et al. (2010), though the space densities are consistent within the 1σ uncertainties. We note that both of these measurements (Oesch et al., 2010a; Hathi et al., 2010) are from the same data, a 50 arcmin^2 area in the GOODS-South region as part of the *HST* Wide-Field Camera 3 Early Release Science (ERS) data (Windhorst et al., 2011). It is important to note that both the ERS bright galaxy sample and our sample may suffer from sample variance, because they are from single, small area fields. Though the ERS UV data covers eight times the area of our survey, they are also probing more massive galaxies, which are more highly biased and subject to sample variance. Therefore surveys in additional fields are needed to address the sample variance at both the bright and faint end of the LF.

2.7.2 Evolution of the Faint-End Slope

Using strong gravitational lensing, we have extended the measurement of the space density of $z \sim 2$ galaxies two orders of magnitude fainter than previous studies, allowing a more precise measure of the faint-end slope of the UV luminosity function. In Figure 2.9, we compare our measurement of the faint-end slope with results at other redshifts. A general implication of this plot is that α is steeper at high redshifts than at lower redshifts. The evolution of the faint-end slope is slow between $2 < z < 7$, however it has evolved significantly between $z = 2.3$ ($\alpha \sim -1.73$ Reddy and Steidel, 2009) and the present ($\alpha \sim -1.2$ Wyder et al., 2005). Our faint-end slope measurement, $\alpha = -1.74$, is nearly consistent with the estimates at higher redshifts ($2.5 < z < 4$) within the error bars. Additional sight lines and deeper selection of UV galaxies at $z \sim 1$ will help us constrain the evolution of the faint end slope over the last 10 Gyr.

2.7.3 Evolution of Dust in Faint Star-Forming Galaxies

In the upper panel of Figure 2.8 we show the β vs. M_{1500} relation of our sample (black line) and similarly selected samples at higher redshift (Reddy and Steidel, 2009; Hathi et al., 2013; Bouwens et al., 2012b). We see the same trend that is seen at higher redshifts in that fainter galaxies have bluer UV spectral slopes. The measured slope of the trend, $d\beta$ / $\mathrm{d}M_{1500} = -0.09 \pm 0.01$, is similar to the slopes measured at higher redshift, though the zeropoint is offset such that galaxies of the same UV luminosity are redder at later epochs. This is consistent with the trend seen from $2.5 < z < 7$ (Bouwens et al., 2012b). The increase in β at the same absolute magnitude from $z \sim 2.5$ to $z \sim 2$ (time difference of ~ 600 Myr) is about 0.4, consistent with the increase in beta from $z \sim 4$ to $z \sim 2.5$ (time difference of ~ 1 Gyr).

The luminosity-dependent UV spectral slope of Reddy and Steidel (2009) (derived from their reddening estimates) is also plotted in Figure 2.8 (plus symbols). Our best fit comes very close to their constant value of β at $M_{1500} \sim -19.5$ mag and consistent with the average value measured by Hathi et al. (2013) at the same redshift. The difference is that Reddy

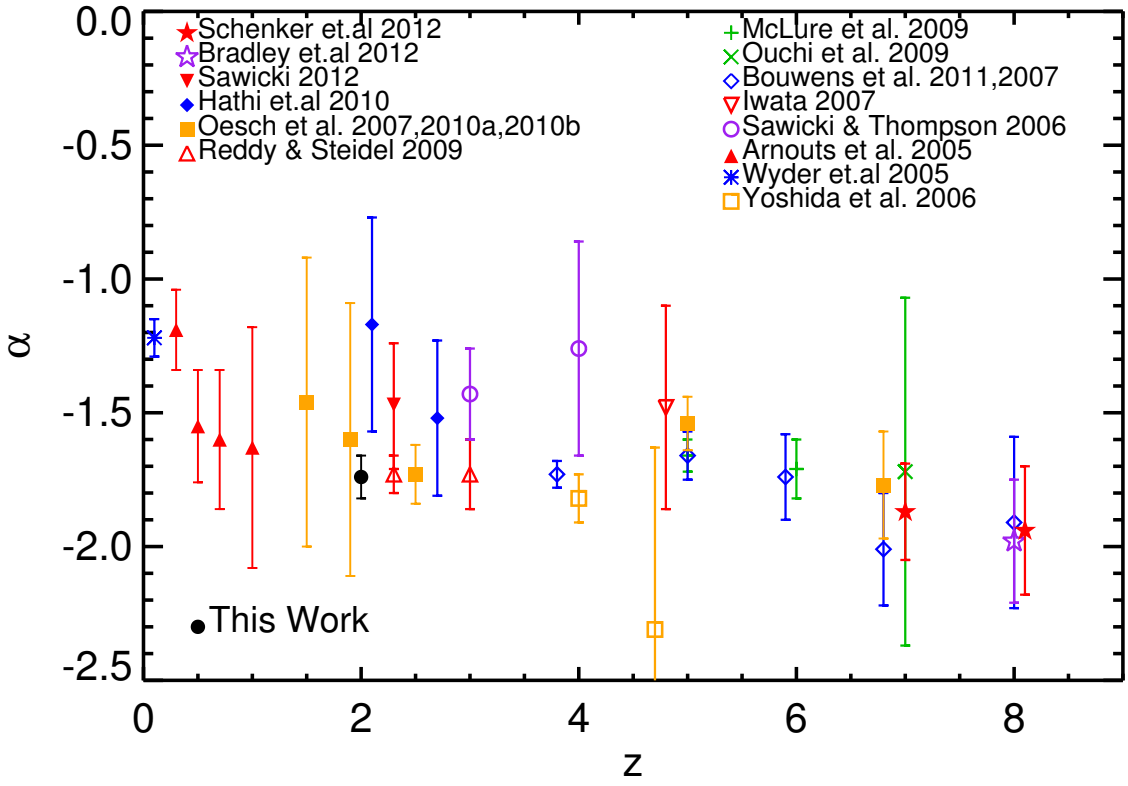

Figure 2.9: The evolution of the faint-end slope with redshift. The black filled circle shows our measurement of α. The plot also includes other determinations from the literature (Arnouts et al., 2005; Wyder et al., 2005; Sawicki and Thompson, 2006; Yoshida et al., 2006; Bouwens et al., 2007; Iwata et al., 2007; Oesch et al., 2007; McLure et al., 2009; Ouchi et al., 2009; Reddy and Steidel, 2009; Oesch et al., 2010a,b; Hathi et al., 2010; Bouwens et al., 2011; Bradley et al., 2012; Sawicki, 2012; Schenker et al., 2013). The data points at z=8 are all at the same redshift but have been offset slightly for clarity.

and Steidel (2009) see bluer galaxies than our sample at $-19.5 < M_{1500} < -18$ mag. In the faintest bin, $M_{1500} \sim -18$ mag, Reddy and Steidel (2009) state that the colors are consistent with no dust extinction, whereas we see significant extinction in galaxies at this absolute magnitude.

We believe that there are two explanations for the redder average spectral slopes exhibited in our sample compared to the Reddy and Steidel (2009) sample. First, there is a 400 Myr time difference between the average redshift of the Reddy and Steidel (2009) sample ($z = 2.3$) and our sample ($z = 2$), and we know that galaxies of the same luminosity are getting redder with time (Bouwens et al., 2012b). Second, we are likely less biased against detecting red galaxies at these absolute magnitudes. Our Lyman break selection is more complete than selections like BM/BX (Adelberger et al., 2004), which purposely target galaxies that are blue in all filters. Also, our ultra-deep imaging along with the high magnification allows us to detect redder, fainter objects at higher S/N in the bluest bands.

The measured reddening of our sample is strongly dependent on the assumed stellar population parameters, as they affect the intrinsic UV spectral slope. This is exhibited in Figure 2.10, where we show that changing the metallicity of the stellar population from 0.2 $Z_{\odot}$ to 1.0 $Z_{\odot}$ decreases the average color excess from $E(B-V) = 0.15$ mag to $E(B-V) = 0.08$ mag. The assumed starburst age has very little effect (average $E(B-V) = 0.15$ mag to $E(B-V) = 0.13$ mag when increasing the age from 100 to 300 Myr).

The lower value of metallicity we have used in this work, $Z = 0.2\ Z_{\odot}$, is justified by the low stellar masses of our sample galaxies ($7 < \log(M/M_{\odot}) < 9$, Dominguez et al., in preparation) and the metallicity measurements at high and low mass at these redshifts (Erb et al., 2006; Belli et al., 2013), assuming that stellar and gas-phase metallicities are similar.

The ultimate goal in measuring the UV spectral slopes of these galaxies is to infer the extinction of the ultraviolet light in order to measure the intrinsic UV luminosities and star formation rates. In the lower panel of Figure 2.8 we show the implied color excess, $E(B-V)$, given the intrinsic spectral slope of our fiducial model (constant star formation, age = 100 Myr, $Z = 0.2\ Z_{\odot}$) and assuming a Calzetti attenuation curve.

Intriguingly, nearly every galaxy brighter than $M_{1500} < -15$ mag has significant reddening. The dashed line in the lower panel of Figure 2.8 shows the average color excess of our sample , $< E(B-V) >= 0.15$ mag, which is similar to the value measured for much more luminous galaxies by Reddy and Steidel (2009, $E(B-V) = 0.13$ mag, plus symbols), Sawicki (2012, purple squares), and Hathi et al. (2013, $E(B-V) = 0.15$ mag, grey filled circle), who assumed solar metallicity.

Thus, we come to the important conclusion that the trend of bluer UV spectral slopes at fainter absolute magnitudes is *not* necessarily due to decreasing dust reddening. Rather, the dust reddening at faint magnitudes ($-18 < M_{1500} < -15$ mag) is similar to the reddening in more luminous galaxies ($-21 < M_{1500} < -18$ mag), and the bluer observed UV slopes are due to bluer *intrinsic* UV slopes because the stellar population is metal poor. Of course, the reddening likely depends on luminosity as well. In order to know the exact relation of average extinction with luminosity, we need a more accurate measure of the luminosity- (or mass) metallicity relation. Furthermore, this analysis has assumed a Calzetti attenuation curve. There is some evidence that young galaxies may have steeper attenuation curves (e.g. SMC, Siana et al., 2008b, 2009; Reddy et al., 2010). Measurements of the infrared luminosities of these faint galaxies will help determine which attenuation curve is more appropriate.

In the future, measurements of metallicities (with rest-frame optical spectroscopy) and infrared luminosities will help us better understand the extinction in these faint galaxies. Because of the high magnification, these galaxies comprise an ideal sample for follow-up.

2.7.4 The Effect of Intracluster Dust

In this study, all of the UV-dropouts are located behind a massive cluster so the light coming from these background galaxies can be affected by intracluster dust. Recent studies of SDSS clusters (Chelouche et al., 2007; Bovy et al., 2008; Muller et al., 2008) have shown that there is a negligible amount of intracluster dust attenuation $E(B-V) < 8 \times 10^{-3}$ mag on scales smaller than 1 Mpc from the cluster center. We estimated the average intracluster dust reddening(A_λ) in the UV and optical bands to see if it has any effect on

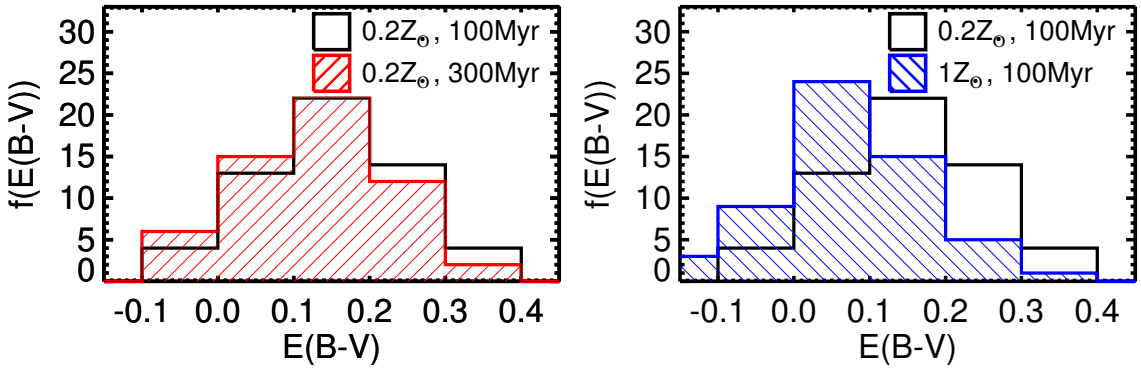

Figure 2.10: The $E(B-V)$ distributions of the $z \sim 2$ LBG sample. The $E(B-V)$ values are derived by comparing the LBG colors with the dust reddened colors predicted by stellar population models. The black distribution is computed by assuming the realistic values for the age (100 Myr) and metallicity (0.2 $Z_{\odot}$) of the stellar population models (see Section 2.4.1). The red (left panel) and the blue (right panel) hatched histograms show the $E(B-V)$ values measured by assuming (0.2 $Z_{\odot}$ & 300 Myr) and (1 $Z_{\odot}$ & 100 Myr), respectively. The assumed age of the galaxy (left) has little effect on the derived reddening values, whereas the assumed metallicity (right) has a very large effect. If we were to assume solar metallicity, a large fraction of galaxies would have colors consistent with no extinction at all.

our LBG selection or spectral slope estimates. Bovy et al. (2008) measures the intracluster dust attenuation for a large sample of SDSS clusters. They calibrate the extinction curve presented in Charlot and Fall (2000), by comparing the spectra of galaxies that lie behind and adjacent to the SDSS clusters. We approximated the A_{λ} values based on their calibrated extinction curve. Both the UV-dropout selection and the UV spectral slope measurements are not significantly affected by intracluster reddening because the estimated color excesses are negligible ($A_{F275W} - A_{F336W} = 0.01$ mag, $A_{F475W} - A_{F625W} = 0.01$ mag).

2.7.5 UV Luminosity Density

In the following discussion we prefer to compare to the samples of Oesch et al. (2010a) and Hathi et al. (2010) because the samples are selected with similar filters and are at a similar redshift. If we integrate our luminosity function over all luminosities down to zero to find the entire UV luminosity density, we get the value of $\rho_{UV} = 43.1^{+6.8}_{-6.0} \times 10^{25}$ erg s^{-1} Hz^{-1} Mpc^{-3}. A large fraction of 71% of the total luminosity density at $z = 2$ is from the

luminosity range of our sample alone ($-19.76 < M_{1500} < -12.76$ mag). The fraction is less than 10% for galaxies in the absolute magnitude range of Oesch et al. (2010a) which are brighter than our sample ($M_{1500} < -19.76$ mag). Our most luminous galaxy is about the faintest galaxy seen in the Oesch et al. (2010a) sample, so there is very little overlap in luminosities. The faint galaxies in our sample account for seven times more UV luminosity density than the brighter galaxies from Oesch et al. (2010a). If we assume the luminosity function has the same slope down to zero luminosity, integrating from our faintest bin down to zero only increases the UV luminosity density by 20%. All of these values are given in Table 2.4. We note that extending the luminosity range to much larger luminosities adds a negligible amount to the UV luminosity density. This demonstrates the power of cluster lensing to quickly uncover the primary sources of star formation at these epochs.

2.7.6 Star Formation Rate Density

The evolution of the star formation rate density (SFRD) has been an ongoing subject of research, especially at $1 < z < 3$ because star formation appears to have peaked at this epoch (e.g., Calzetti and Heckman, 1999; Steidel et al., 1999; Ferguson et al., 2000; Hopkins et al., 2000; Hopkins and Beacom, 2006; Reddy and Steidel, 2009). Because of the steep faint-end slope of the LF, much of the star formation occurs in faint galaxies. Furthermore, because of the significant extinction seen in our sample, there is even more star formation in our faint sample.

Of course, because this population is not well studied, many of the assumptions typically applied in such studies may not apply to our sample. First, as mentioned previously, the metallicity is likely significantly lower than Solar, which results in significant ($\sim 15\%$) differences in the conversion of UV luminosity density to SFRD. Second, the starburst ages may be significantly younger than 10^8 yr. For younger starbursts, the star formation rate is a function of both the UV luminosity and the population age. Indeed, the assumption of continuous star formation may not be accurate at all in these systems where supernovae are thought to be very effective at shutting down star formation on short time scales (e.g.

Governato et al., 2012). Third, because the typical attenuation curve in such systems has not been well measured, the dust corrections are still not well understood. Given these caveats, we calculate below the best estimate of the SFRD from UV-selected galaxies at $z \sim 2$.

We use the Kennicutt (1998) conversion of the UV luminosity density to SFR as below:

$$\mathrm{SFR}(\ \mathrm{M}_\odot\ \mathrm{yr}^{-1}) = 1.4 \times 10^{-28} L_{\mathrm{UV}}\ (\mathrm{erg\ s^{-1}Hz^{-1}}) \tag{2.15}$$

where a Salpeter initial mass function (Salpeter, 1955) from 0.1-100 $M_\odot$ is assumed. Using the total UV luminosity density from Table 2.4, we find a SFRD uncorrected for dust of 0.060 $M_\odot$ yr^{-1} Mpc^{-3}. To correct for extinction, we note that the average attenuation measured in our sample ($E(B-V) = 0.15$ mag) is similar to the values measured at the bright end by Reddy and Steidel (2009) and Hathi et al. (2013). Thus, we use this constant value to derive a factor of 4.17 correction for extinction (assuming a Calzetti attenuation curve) for galaxies of all luminosities. We therefore determine a SFRD of $0.252^{+0.040}_{-0.035}$ $M_\odot$ yr^{-1} Mpc^{-3} for UV-selected galaxies at $z \sim 2$. If we use a Kroupa (Kroupa, 2001) or Chabrier (Chabrier, 2003) IMF, this value needs to be divided by 1.7 or 1.8, respectively to account for the decreased number of low mass stars relative to the Salpeter IMF. We convert to a Kroupa IMF ($\mathrm{SFRD_{Kroupa}} = 0.148^{+0.023}_{-0.020}$ M$_\odot$ yr^{-1} Mpc^{-3}) to compare to the value estimated by Reddy and Steidel (2009, $0.122^{+0.027}_{-0.027}$ M$_\odot$ yr^{-1} Mpc^{-3}). Our value is about 20% higher but within their error bars. It is important to note however, that Reddy and Steidel (2009) use an average dust extinction correction factor of 1.91, less than half the correction that we use (4.17). Thus, if they implemented the same constant extinction correction as this paper for all UV-selected galaxies, their estimate of the SFRD would more than double. This shows the importance of the dust correction estimate for the fainter galaxies.

Table 2.4. UV Luminosity Density

Range[a]	UV Luminosity Density[b]
[-21.68,-19.76][c]	$4.16^{+0.46}_{-0.49}$
[-19.76,-12.76]	$30.8^{+1.9}_{-3.1}$
[-12.76,0.00]	$8.09^{+4.4}_{-2.4}$
[-21.68,0.00]	$43.1^{+6.8}_{-6.0}$

[a]Absolute magnitudes at 1500 Å.

[b]units of $\times 10^{25}$ erg s^{-1} Hz^{-1} Mpc^{-3}

[c]The Oesch et al. (2010a) limit is slightly fainter, but we only integrate to our bright limit

2.8 Summary

The sensitive ultraviolet imaging capability of the WFC3/UVIS camera allows us to study intermediate redshift ($1 < z < 3$) star-forming galaxies. We used the deepest near-UV images ever obtained with the *HST*/UVIS channel to identify ultra-faint star-forming galaxies located behind the massive cluster Abell 1689. We found 58 Lyman break galaxies at $z \sim 2$ that are highly magnified due to strong gravitational lensing. The main conclusions of this work are summarized below:

- The faint-end slope of the UV luminosity function is estimated to be $\alpha = -1.74 \pm 0.08$, consistent with previous determinations at $2.3 < z < 6$ (Bouwens et al., 2007; Reddy and Steidel, 2009).

- The UV luminosity function shows no turnover down to very faint UV magnitudes ($M_{1500} \sim -13$ mag). This is particularly interesting because the bright sources do not provide sufficient ionizing photons to ionize the universe by $z \sim 6$ (Robertson et al., 2013). Galaxies of such low luminosities are required at $z > 7$ to reionize the intergalactic hydrogen and produce the high Thompson scattering optical depth

to the cosmic microwave background seen by the Wilkinson Microwave Anisotropy Probe (Kuhlen and Faucher-Giguère, 2012; Robertson et al., 2013). Indeed, these faint galaxies may contribute significantly to the ionizing background at moderate redshift ($z \sim 3$, Nestor et al., 2013).

However recent numerical simulations by Kuhlen et al. (2013) show a cutoff in the simulated UV LF at M_{1500}=-16, due to the suppression of the star formation in low metallicity faint galaxies. The discrepancy between our results and Kuhlen et al. (2013) is only in our two faintest magnitude bins, where the number of objects is small. Further LBG searches in more lensing clusters will provide a more robust test of this prediction.

- The UV spectral slope, β, for these LBGs at $z \sim 2$ is redder than higher redshift determinations at the same UV luminosities. The correlation between β and the rest-frame UV magnitude implies higher dust extinction in more luminous galaxies, as is seen at higher redshifts. We find evidence for significant dust extinction, averaging $E(B-V) \sim 0.15$ mag, in most star-forming galaxies with $-18 < M_{1500} < -15$ mag, in contrast with previous measurements at these redshifts (Reddy and Steidel, 2009; Sawicki, 2012). Our finding assumes a Calzetti attenuation curve and $Z = 0.2\ Z_{\odot}$ metallicity. Both assumptions need to be confirmed with further studies.

- We derive a total UV luminosity density of $4.31^{+0.68}_{-0.60} \times 10^{26}$ erg s^{-1} Hz^{-1} Mpc^{-3} when integrating our luminosity function and extrapolating to zero luminosity. More than 70% of the UV luminosity density originates from the galaxies in the luminosity range covered by our sample. We estimate that no more than 20% of the UV luminosity density originates from fainter galaxies than those in our sample.

- Assuming a constant extinction ($E(B-V) = 0.15$ mag, UV dust correction of 4.2) for galaxies of all luminosities, we estimate the global SFRD (of UV-selected galaxies) to be $0.148^{+0.023}_{-0.020}\ M_{\odot}$ yr^{-1} Mpc^{-3} (Kroupa IMF). This number is dependent on many assumptions regarding the ages, metallicities and extinction curves for this faint pop-

ulation of galaxies. Further investigations are required to accurately determine these properties of this new population.

The authors wish to thank Pascal Oesch who kindly sent his data to us for our LF computations. We also thank the referee for useful suggestions, as well as Marcin Sawicki for his valuable comments. This work is based on observations with the NASA/ESA Hubble Space Telescope, obtained at the Space Telescope Science Institute, which is operated by the Association of Universities for Research in Astronomy, Inc., under NASA contract NAS 5-26555.

Chapter 3

The Evolution of the Faint End of The UV Luminosity Function During the Peak Epoch of Star Formation $(1 < z < 3)$

Abstract

We present a robust measurement of the rest-frame UV luminosity function (LF) and its evolution during the peak epoch of cosmic star formation at $1 < z < 3$. We use our deep near ultraviolet imaging from WFC3/UVIS on the *Hubble Space Telescope* (*HST*) and existing ACS/WFC and WFC3/IR imaging of three lensing galaxy clusters, Abell 2744 and MACSJ0717 from the Hubble Frontier Field survey and Abell 1689. Combining deep UV imaging and high magnification from strong gravitational lensing, we use photometric redshifts to identify 780 ultra-faint galaxies with $M_{UV} < -12.5$ AB mag at $1 < z < 3$. From these samples, we identified 5 new, faint, multiply imaged systems in A1689. We run a Monte Carlo simulation to estimate the completeness correction and effective volume for each cluster using the latest published lensing models. We compute the rest-frame

UV LF and find the best-fit faint-end slopes of $\alpha = -1.56 \pm 0.04$, $\alpha = -1.72 \pm 0.04$ and $\alpha = -1.94 \pm 0.06$ at $1.0 < z < 1.6$, $1.6 < z < 2.2$ and $2.2 < z < 3.0$, respectively. Our results demonstrate that the UV LF becomes steeper from $z \sim 1.3$ to $z \sim 2.6$ with no sign of a turnover down to $M_{UV} = -14$ AB mag. We further derive the UV LFs using the Lyman break "dropout" selection and confirm the robustness of our conclusions against different selection methodologies. Because the sample sizes are so large, and extend to such faint luminosities, the statistical uncertainties are quite small, and systematic uncertainties (due to the assumed size distribution, for example), likely dominate. If we restrict our analysis to galaxies and volumes above $> 50\%$ completeness in order to minimize these systematics, we still find that the faint-end slope is steep and getting steeper with redshift, though with slightly shallower (less negative) values ($\alpha = -1.55 \pm 0.06$, -1.69 ± 0.07 and -1.79 ± 0.08 for $z \sim 1.3$, 1.9 and 2.6, respectively). Finally, we conclude that the faint star-forming galaxies with UV magnitudes of $-18.5 < M_{UV} < -12.5$ covered in this study, produce the majority (55%-60%) of the unobscured UV luminosity density at $1 < z < 3$.

3.1 Introduction

The galaxy luminosity function (LF) is a fundamental tool to study the formation and evolution of galaxies as the shape of the LF is mainly determined by the mechanisms that regulate the star formation in galaxies (Rees and Ostriker, 1977; White and Rees, 1978; Benson et al., 2003). Comparing the LF with the underlying dark matter halo mass function reveals the importance of different modes of feedback in galaxy formation, with the active galactic nuclei feedback dominating the bright end and supernova and radiation-driven winds dominating the faint end (e.g., Dekel and Birnboim, 2006; Somerville et al., 2008). Furthermore, the LF is a key probe to assess the contribution of galaxies with different luminosities to the total light budget at different redshifts.

As ultraviolet (UV) light is a tracer of recent star formation in galaxies, the UV LF can help determine the total star formation rate density at all epochs. In addition, the UV LF is one of the few galaxy observables which is directly measurable at all epochs using current telescopes. Over the past 20 years, many studies have been devoted to UV LF measurements at high redshifts with $z > 3$ (Steidel et al., 1999; Adelberger and Steidel, 2000; Bunker et al., 2004; Dickinson et al., 2004; Ouchi et al., 2004; Yan and Windhorst, 2004; Beckwith et al., 2006; Yoshida et al., 2006; Sawicki and Thompson, 2006; Bouwens et al., 2007; Iwata et al., 2007; McLure et al., 2009; Ouchi et al., 2009; van der Burg et al., 2010; Bradley et al., 2012; Cucciati et al., 2012; McLure et al., 2013; Schenker et al., 2013; Atek et al., 2014; Schmidt et al., 2014b; Atek et al., 2015b,a; Bouwens et al., 2015; Bowler et al., 2015; Finkelstein et al., 2015; Ishigaki et al., 2015), intermediate redshifts with $1 < z < 3$ (Dahlen et al., 2007; Reddy et al., 2008; Hathi et al., 2010; Oesch et al., 2010a; Cucciati et al., 2012; Sawicki, 2012; Parsa et al., 2016) including our previous work (Alavi et al., 2014, hereafter A14), as well as low redshifts with $z < 1$ (Arnouts et al., 2005; Budavári et al., 2005; Wyder et al., 2005; Haberzettl et al., 2009; Ly et al., 2009; Cucciati et al., 2012). Taken together, these measurements suggest a rise and fall in the history of cosmic star formation from high redshifts to the present time with a peak sometime between $1 < z < 3$ (Madau and

Dickinson, 2014, and references therein). Therefore the redshift range of $1 < z < 3$, known as the peak epoch of cosmic star formation, is a critical time in galaxy evolution.

Many wide and shallow surveys have probed the UV LF of rarer, luminous galaxies at $1 < z < 3$. Arnouts et al. (2005) used the WFPC2 data in the HDF-North and HDF-South and measured a faint-end slope of $\alpha = -1.5 \pm 0.2$ for the UV LF at $z = 2 - 3$. Later, Reddy and Steidel (2009) used a wide ground-based survey covering luminosities with $L > 0.05\ L^*$[1] and measured a steep faint-end slope of $z = -1.73 \pm 0.07$ at $z = 2.3$. Following the installation of WFC3 on the *Hubble Space Telescope* (*HST*), Oesch et al. (2010a) used the wide, shallow Early Release Survey (ERS; Windhorst et al., 2011) and measured steep faint-end slopes ($-1.46 < \alpha < -1.84$) for the UV LFs at $z = 1.0 - 2.5$. However, in order to study the UV LF at fainter luminosities and accurately quantify the faint-end slope, deeper surveys were needed. In A14 (see next paragraph for more details), we used a very deep UV observation of the Abell 1689 (hereafter A1689) cluster obtained with the WFC3/UVIS channel and we extended the $z \sim 2$ UV LF $100\times$ fainter than previous shallower surveys ($L \sim 0.0005\ L^*$). We concluded that the UV LF has a steep faint-end slope of $\alpha = -1.74 \pm 0.08$ with no evidence of a turnover down to $M_{UV} = -13$. Parsa et al. (2016) recently found galaxies as faint as $L > 0.002\ L^*$ utilizing the CANDELS/GOODS-South, UltraVISTA/COSMOS and HUDF data. However, their estimate of the faint-end slope $\alpha = -1.32 \pm 0.03$ is significantly shallower than others. A shortcoming of these two deep surveys is that they probe a single field (A1689 in A14 and HUDF dominating the faint luminosities in Parsa et al. (2016)), where the field-to-field variations affect the LF measurements. In this paper, we attempt to overcome this problem by combining deep observations of three lines of sight.

Faint star-forming galaxies play a critical role in galaxy formation and evolution, because they significantly contribute to IGM metal enrichment (Madau et al., 2001; Porciani and Madau, 2005), are the most plausible sources of ionizing photons during the reionization epoch (Kuhlen and Faucher-Giguère, 2012; Robertson et al., 2013) and maintain the ioniz-

[1] To be consistent with other studies, we quote these limits in terms of $L^*_{z=3}$, i.e. $M^*_{1700,AB} = -21.07$, from Steidel et al. (1999).

ing background at $z > 3$ (Nestor et al., 2013). However, these faint galaxies are inaccessible at high redshifts as they lay outside of the detection limits of current surveys. One powerful way to explore these faint galaxies, is to exploit the magnification of strong gravitational lensing offered by foreground massive systems and thus push the detection limits to lower luminosities. There have been many studies of high redshift galaxies lensed by individual galaxies (e.g., Pettini et al., 2002; Siana et al., 2008b, 2009; Stark et al., 2008; Jones et al., 2010; Yuan et al., 2013; Vasei et al., 2016). However, galaxy clusters acting as gravitational lenses can magnify a large area (e.g., Narayan et al., 1984; Kneib and Natarajan, 2011), allowing a study of many highly magnified galaxies in a single pointing. In A14, combining our deep observations and magnification from strong gravitational lensing from A1689 enabled us to identify background ultra-faint galaxies.

This technique of targeting lensing galaxy clusters has been extensively used since the discovery of the first gravitationally lensed arc in the Abell 370 cluster (Soucail et al., 1987), and has culminated with recent large surveys of lensing clusters such as the CLASH (Postman et al., 2012) and Hubble Frontier Field (HFF) (Lotz et al., 2016) surveys. The HFF program obtains very deep optical and near-infrared imaging over six lensing clusters using *HST*/ACS and *HST*/WFC3, respectively. These deep images enable a search for the faint galaxies as opposed to the shallow CLASH data, which restrict the search to bright galaxies even in the case of high magnification. In addition, the HFF primary observations are complemented with data from *Spitzer, ALMA, Chandra, XMM*, VLA, VLT and Subaru as well as our deep *HST*/WFC3 UV imaging in this study. Since the beginning of the HFF program, many groups have studied the faint-end of the UV LF at $z > 5$ up to $z = 9$ (Atek et al., 2014; Ishigaki et al., 2015; Atek et al., 2015b,a; Livermore et al., 2016).

There are two primary methods of identifying high redshift galaxies, via photometric redshifts and color-color selection of the Lyman break. Both techniques require assumptions about stellar populations, dust reddening and star formation histories. However, each technique has its advantages. The photometric redshift method uses the full SED whereas the Lyman break method requires fewer filters and simpler completeness corrections. Some

groups use the Lyman break technique (e.g., Hathi et al., 2010; Bouwens et al., 2015), while other groups prefer photometric redshifts (e.g., Finkelstein et al., 2015; Parsa et al., 2016). A general agreement between the UV LFs from these two methods is shown both at intermediate (Oesch et al., 2010a) and high redshift studies (McLure et al., 2011, 2013; Schenker et al., 2013). One of the goals of this paper is to exploit the available multiwavelength imaging to provide a comparison between the UV LFs derived with these two selection techniques.

In this paper, we utilize the strong gravitational lensing magnification from three foreground galaxy clusters (two from the HFF program) in combination with our deep WFC3/UVIS imaging to construct a robust sample of faint star-forming galaxies at $1 < z < 3$. The study is similar to A14, but spanning the entire redshift range $1 < z < 3$, and measuring the LF behind three clusters instead of one. This allows us to study the evolution of the UV LF during the peak epoch of global star formation activity (i.e., $1 < z < 3$), and compare with previous determinations. The structure of this paper is as follows. In Section 4.2, we summarize the available observations and the data reduction for each lensing cluster. The catalog construction and photometric redshift measurements are described in Section 3.3 and 3.4, respectively. We briefly review the lens models and the multiple image identification in Section 3.5. We present our selection criteria and photometric redshift samples in Section 3.6. This is followed in Section 3.7, where we provide detailed description for the completeness simulation. We then discuss the UV LF measurements for the photometric redshift samples in Section 3.8 and for the dropout samples in Section 3.9. We compare the UV LFs obtained by different selection techniques, evolution of the UV LF and UV luminosity density in Section 3.10. Finally in Section 3.11, we provide a summary of our conclusions. In the appendices, we describe our color-color selection criteria, the corresponding LBG samples and the completeness simulation for the LBG UV LF. We also provide a list of newly found multiple images of A1689.

In this paper, all distances and volumes are in comoving coordinates. All magnitudes are quoted in the AB system (Oke and Gunn, 1983) and we adopt $\Omega_M = 0.3$, $\Omega_\Lambda = 0.7$ and $H_0 = 70$ km s^{-1} Mpc^{-1}.

3.2 Data

In this section, we describe the data sets of three lensing fields used in this study and briefly explain the data reduction processes, as a more detailed description will be included in a future UV survey paper (Siana et al., in preparation). In this work we use deep *HST* imaging of three lensing clusters in a wide wavelength range, from UV to NIR, as described below.

3.2.1 Hubble Frontier Field Observations and Data Reduction

The HFF survey uses the *HST* Director's Discretionary time (GO/DD 13495, PI Lotz), to obtain deep WFC3/IR and ACS/WFC images of six lensing clusters and their parallel fields (Lotz et al., 2016). The two HFF clusters analyzed here, Abell 2744 (hereafter A2744) and MACSJ0717.5+3745 (hereafter MACSJ0717), were observed during cycles 21 and 22, with 140 orbits of ACS/WFC and WFC3/IR imaging for each cluster/field pair. The NIR images are taken in F105W, F125W, F140W and F160W filters, and the optical data are obtained in F435W, F606W and F814W filters for each cluster.

In addition, we obtained deep near ultraviolet images in F275W (8 orbits) and F336W(8 orbits) for three HFF clusters (including A2744 and MACSJ0717) using the WFC3/UVIS channel onboard *HST*. These deep UV images are part of *HST* program ID 13389 (PI: B. Siana), which were taken between November 2013 and April 2014.

The Space Telescope Science Institute (STScI) handles the reduction and calibration of the optical and NIR images of the HFFs and releases the final mosaics in the Mikulski Archive for Space Telescopes (MAST)[2]. We used the version 1.0 release of the public optical and NIR mosaics with a pixel scale of 60 mas pixel^{-1}. To make these mosaics, the raw optical and NIR exposures were initially calibrated using PYRAF/STSDAS `CALACS` and `CALWF3` programs, respectively. The calibrated images were then aligned and combined using `Tweakreg` and `AstroDrizzle` (Gonzaga and et al., 2012) tasks in PYRAF/DrizzlePac package, respectively. In order to further improve the data reduction processes, the HFF team provides "self-calibrated" ACS images including more accurate dark subtraction and

[2] `https://archive.stsci.edu/prepds/frontier/`

charge transfer efficiency (CTE) correction as well as WFC3/IR images corrected for the time-variable sky lines.

To calibrate the raw UV data, we applied two major improvements in addition to the standard WFC3/UVIS calibration approach. The first improvement is related to the CTE degradation of the UVIS CCD detectors. This degradation caused by radiation damage in the CCDs, results in a loss of source flux and affects the photometry and morphology measurements especially in low background images (e.g UV data, Teplitz et al., 2013). To correct for these charge losses in our UV images, we used a pixel-based CTE correction tool provided on the STScI website[3]. The second improvement is in the dark current subtraction from the UV images. As shown in a recent work by Teplitz et al. (2013), the standard WFCS3/UVIS dark subtraction process is not sufficient for removing dark structures and hot pixels, mainly due to the low background level in the UV data. This regular technique leaves a background gradient and blotchy patterns in the final science image. Therefore, we used a new methodology introduced by Rafelski et al. (2015) for subtracting the dark current and masking the hot pixels properly. A detailed description of this technique is presented in Rafelski et al. (2015).

After making the modified calibrated UV images, we use the PYRAF/DrizzlePac package to drizzle these images to the same pixel scale of 60 mas and astrometrically align with the optical and NIR data. The `AstroDrizzle` program subtracts the background, rejects the cosmic rays, and corrects the input images for the geometric distortion due to the non-linear mapping of the sky onto the detector. In addition to the science output images, `AstroDrizzle` generates an inverse variance map (IVM) which we used later to make the weight images and to calculate the image depths. A summary of all the images and their depths is given in Table 3.1.

[3] `http://www.stsci.edu/hst/wfc3/tools/cte$_$tools`

3.2.2 A1689 Observations and Data Reduction

In addition to the two HFF clusters, we observed the A1689 cluster. This cluster has been observed in three WFC3/UVIS bandpasses (F225W, F275W and F336W) as part of program IDs 12201 and 12931 (PI: B. Siana), taken in cycle 18 in December 2010 and cycle 20 in February and March 2012, respectively. The cycle 18 data (30 orbits in F275W, 4 orbits in F336W) were used in A14 to measure the UV LF of lensed, dwarf galaxies at $z \sim 2$. In cycle 20, we added an F225W image (10 orbits) and deeper F336W data (14 orbits, for a total of 18 orbits) to expand our redshift range from $1 < z < 3$.

The data calibration and reduction are the same as explained above for the HFF UV images. These data are corrected for the CTE degradation and dark subtraction, as well. Moreover, A1689 is observed with ACS/WFC in 5 optical bandpasses (F475W, F625W, F775W, F814W and F850LP), which were calibrated and reduced as was described in A14. The A1689 images are all mapped to the same pixel scale of 40 mas pixel^{-1}.

3.3 Object Photometry

A detailed description for the A1689 photometry is given in A14. Here we provide the details of the photometric measurements for the HFF data. Since our HFF data cover a large range of wavelengths (from UV up to NIR), the width of the point spread function (PSF) changes considerably. To do multiband photometry, we match the PSF of all of the images to the F160W band, which has the largest PSF. We used the IDL routine `StarFinder` (Diolaiti et al., 2000) to stack all of the unsaturated stars in the field and extract the PSF. We fit a simple Gaussian function to each extracted PSF using the IRAF imexamine task, and then derive the PSF matched images by convolving each band with a Gaussian kernel of appropriate width. We use `SExtractor` (Bertin and Arnouts, 1996) to perform object detection and photometry. The final catalog areas are 4.81, 5.74, and 6.42 arcmin^2 where the WFC3 and ACS images are available for A2744, MACSJ0717 and A1689, respectively.

Table 3.1. Observations and Image Depths

Cluster	A2744(HFF)		MACSJ0717(HFF)		A1689	
Instrument/Filter	Orbits	Depth[a]	Orbits	Depth[a]	Orbits	Depth[a]
WFC3/F225W	···	···	···	···	10	27.71
WFC3/F275W	8	27.80	8	27.43	30	28.14
WFC3/F336W	8	28.20	8	27.86	18	28.36
ACS/F435W	18	28.70	19	28.46	···	···
ACS/F475W	···	···	···	···	4	28.04
ACS/F606W	9	28.70	11	28.59	···	···
ACS/F625W	···	···	···	···	4	27.76
ACS/F775W	···	···	···	···	5	27.69
ACS/F814W	41	29.02	46	28.87	28	28.72
ACS/F805LP	···	···	···	···	7	27.30
WFC3/F105W	24.5	28.97	27	29.02	···	···
WFC3/F125W	12	28.64	13	28.60	···	···
WFC3/F140W	10	28.76	12	28.61	···	···
WFC3/F160W	24.5	28.77	26	28.65	···	···

[a]5σ limit in a $0.2''$ radius aperture

We run SExtractor in dual image mode, with F475W and F435W bands as detection images for A1689 and HFF clusters, respectively. We use F435W band to minimize contamination from the cluster galaxies and intracluster light, as this filter probes below the 4000 Å break, where the galaxies are considerably fainter. To improve the detection of faint objects and to avoid detecting spurious sources (i.e., over-blended from very bright galaxies), for the SExtractor parameters, we set DETECT_MINAREA to 4(5) and DETECT_THRESH to 0.9σ (1.0σ) significance for A2744 (MACSJ0717). The minimum contrast parameter for deblending (DEBLENS_MINCONT) is set to 0.02 for both cluster fields. The fluxes are measured in isophotal (ISO) apertures. The IVM images produced by the drizzling process as mentioned in Section 3.2.1, were converted to the RMS_MAPs by taking their inverse square root. SExtractor uses these RMS_MAPs to derive the flux uncertainties. We correct these RMS_MAPs for the correlated noise (A14, Casertano et al., 2000) from drizzling the mosaics. Finally, we correct our photometry for the Galactic extinction toward each cluster using the Schlafly and Finkbeiner (2011) IR dust maps. To account for systematic error (i.e., due to uncertainty in the Galactic extinction, the zero point values, PSF-matched photometry), we add, in quadrature, a 3% flux error (Dahlen et al., 2010; Vargas et al., 2014) in all bands for all three cluster fields.

3.4 Photometric Redshifts

We use a template fitting function code, EAZY, (Brammer et al., 2008) to estimate the photometric redshift of galaxies in all of our lensing fields. EAZY has two characteristic features that distinguish it from the other photometric redshift codes. First, it derives the optimized default template set from semianalytical models with perfect completeness down to very faint magnitudes rather than using biased spectroscopic samples. Second, it has the ability to fit to a linear combination of basis templates rather than fitting to a single template, which is usually not a good representation of a real galaxy. We varied several EAZY input parameters to find the optimal values. Running EAZY using a variety of empirical

(Coleman et al., 1980; Kinney et al., 1996) or stellar synthetic templates (Grazian et al., 2006; Blanton and Roweis, 2007) allows us to find the set of models where the output photometric redshifts are in the best agreement with the spectroscopic redshifts. We use PÉGASE (Fioc and Rocca-Volmerange, 1997) stellar synthetic templates, which provide a self-consistent treatment of nebular emission lines and include a wide variety of star formation histories (constant, exponentially declining) and a Calzetti dust attenuation curve (Calzetti et al., 2000). We do not use template error function capability in EAZY because it causes poorer agreement with spectroscopic redshifts. We also do not use the magnitude priors, as these functions do not cover the faint luminosities targeted in this work. `EAZY` uses the Madau (1995) prescription for absorption from the intergalactic medium.

For the HFFs (A1689), we derive the photometric redshifts using the complete 9(8) photometry bands of F275W, F336W,F435W, F606W,F814W, F105W, F125W, F140W and F160W (F225W, F275W, F336W,F475W, F625W, F775W, F814W, F850LP) with the central wavelengths covering from 0.27-1.54 (0.24-0.91) μm. Figure 3.1 shows the comparison between the photometric redshifts and the spectroscopic redshifts for all three clusters. For both of the HFF clusters, we use the spectroscopic redshifts from the GLASS program, which obtained grism spectroscopy of 10 massive clusters including the HFFs (Schmidt et al., 2014a; Treu et al., 2015). We note that we only include their measurements with high quality parameter (i.e., quality$>$ 4) for a secure redshift estimate. In addition, for A2744, we also use the spectroscopic redshifts from the literature (Owers et al., 2011; Richard et al., 2014; Wang et al., 2015). For MACSJ0717, we add the spectroscopic redshifts from our Keck/MOSFIRE spectral observations as well as the redshfits from the literature (Limousin et al., 2012; Ebeling et al., 2014). Most of the spectroscopic redshifts of A1689 were described in A14, but here we also include our new measurements from our Keck/MOSFIRE spectra taken on January 2015. A detailed study of spectroscopic data for these samples will be presented in a future paper. From all 186 galaxies with spectroscopic redshifts, 68 are within our target redshift range of $1 < z < 3$. For these galaxies with spectroscopic redshift

of $1 < z_{spec} < 3$, we calculate normalized median absolute deviation[4] to be $\sigma_{NMAD} = 0.025$ (Ilbert et al., 2006) and find six outliers defined to have $\Delta z/(1+z_{spec}) > 5\sigma_{NMAD}$ (Brammer et al., 2008). The median and mean values of fractional redshift error, $\Delta z/(1 + z_{spec})$, after excluding outliers are 0.02 and 0.03, respectively.

Though the agreement between the photometric and spectroscopic redshifts is strong evidence for reliability of our redshift estimates, it is restricted to the brighter galaxies. While our photometric redshift samples contain galaxies as faint as F606W (F625W for A1689) = 30 AB magnitudes, our spectroscopic samples cover magnitudes down to F606W (F625W for A1689) = 26.46. We note that among these objects, we have 5 galaxies at $1.2 < z_{spec} < 2.2$ with very faint magnitudes of $-15.4 < M_{UV} < -14$, where their spectroscopic and photometric redshifts agree well with mean $\Delta z/(1 + z_{spec}) = 0.04$. To further investigate the reliability of our photometric redshift estimates of the faint galaxies[5], where the spectroscopic redshifts are not available, we use a redshift quality parameter, Q [6]. It is a statistical estimate of the reliability of the photometric redshift outputs of EAZY. Brammer et al. (2008) find that the photometric redshift scatter (i.e., difference between photometric redshift and spectroscopic redshift) is an increasing function of Q parameter with a sharp increase above Q=2-3. We calculate the Q parameter for our faint galaxies, as well as for the galaxies with spectroscopic redshifts of $1 < z < 3$. A comparison between these two sub-samples shows that the distributions of Q values are similar (i.e., the faint galaxies are *not* skewed toward higher values of Q), such that the spectroscopic galaxies have median Q of 0.9, 1.1 and 1.5 relative to the faint galaxies with median Q of 0.6, 1.1 and 2.2 for $z \sim 1.3$, 2.2 and 2.6 samples, respectively. We note that these values are within the safe regime for Q parameter (i.e., $Q < 3$, as explained above).

[4] The normalized median absolute deviation is defined as $\sigma_{NMAD} = 1.48 \times \text{median}(|\Delta z - \text{median}(\Delta z)|/(1+z))$ (Ilbert et al., 2006; Brammer et al., 2008). Unlike the usual standard deviation, σ_{NMAD} is not sensitive to the presence of outliers.

[5] We define the faint galaxies based on the limiting magnitude used in our sample selection criteria (see Section 3.6). They are defined to have S/N< 5 in either detection filter or the rest-frame 1500 Å filter.

[6] Q parameter (see Equation 8 in Brammer et al. (2008)) combines the reduced-χ^2 of the fitting procedure with the width of the 68% confidence interval of the redshift probability distribution function to present an estimate of the reliability of the output redshift.

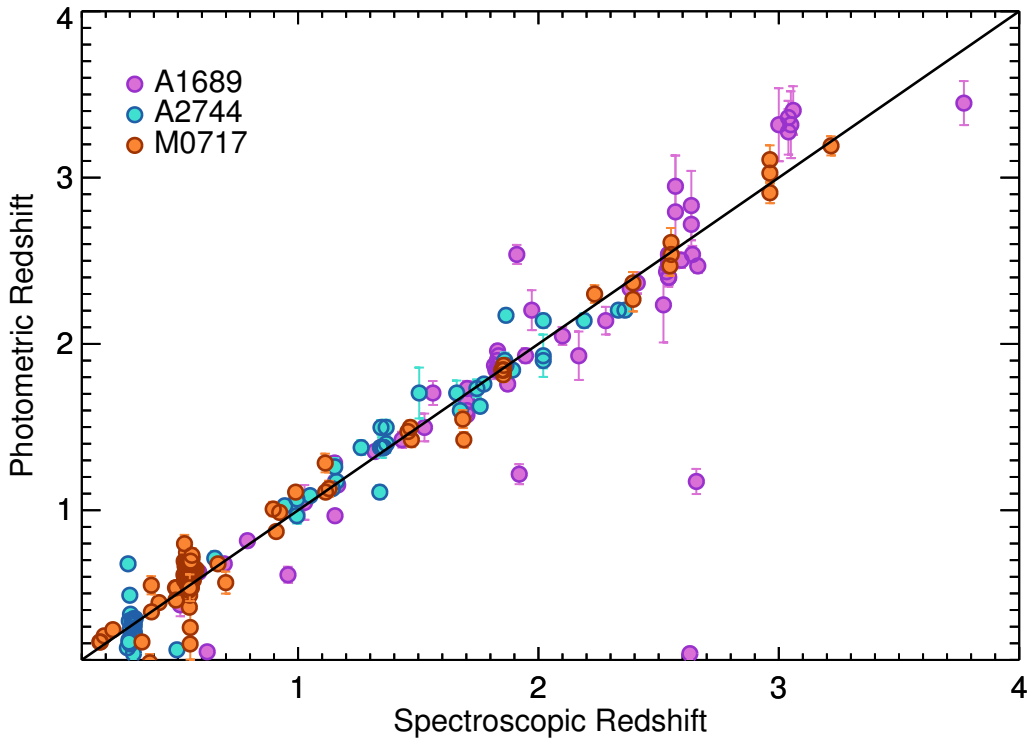

Figure 3.1: Comparison between the photometric and spectroscopic redshifts for 244 galaxies in all three lensing fields. The spectroscopic redshifts are either from our Keck/MOSFIRE and Keck/LRIS data or from the literature (for more details see the text). The purple, orange and cyan circles show the measurements for the A1689, MACSJ0717 and A2744 cluster fields, respectively.

3.5 Lens Models

In order to estimate intrinsic properties (i.e., luminosity) of the background lensed galaxies in our samples, we require an accurate mass model of the galaxy cluster to calculate the lensing magnification. For the HFF program, there are several groups working independently to use deep HFF optical and NIR imaging to model the mass distribution for all of the six clusters (Bradač et al., 2005; Liesenborgs et al., 2006; Diego et al., 2007; Jullo et al., 2007; Jullo and Kneib, 2009; Merten et al., 2009; Zitrin et al., 2009; Oguri, 2010; Merten et al., 2011; Zitrin et al., 2013; Sendra et al., 2014). The main distinction between these models is that some groups assume light traces mass and parametrize the total mass distribution as a combination of individual cluster members and large scale cluster halo components, while the other groups use a non-parametric mass modeling technique, avoiding any priors on the light distribution. In a recent study, Priewe et al. (2016) provide a comparison between these different lens models. All of these models are constrained by the location and the redshift of known multiply imaged systems. Besides observational constraints from strong gravitational lensing, several teams also incorporate the weak lensing shear profile from ground-based observations. All of the HFF lens models and the methodologies adopted by each team are publicly available via the STScI website[7]. In this section, we briefly review the mass models that we used for each of our lensing clusters.

3.5.1 HFF Lensing Models

For the HFF clusters, we utilize the lens models produced by the Clusters As TelescopeS (CATS) collaboration (Co-PIs J.-P. Kneib and P. Natarajan; Admin PI H. Ebeling) who use the `Lenstool` software[8] (Jullo et al., 2007) to parameterize the lens mass distribution. `Lenstool` is a hybrid code which combines both strong- and weak-lensing data to constrain the lens mass model. `Lenstool` models each cluster's mass as a composition of one or more large cluster halos plus smaller subhalos associated with individual galaxies identified

[7] https://archive.stsci.edu/prepds/frontier/lensmodels/
[8] https://projets.lam.fr/projects/lenstool/wiki

either spectroscopically or photometrically as cluster members. The output best model from `Lenstool` is parameterized through a Bayesian approach.

For A2744, we use the strong lensing model of Jauzac et al. (2015), which uses 61 multiply-imaged systems found in the complete HFF optical and NIR data. For MACS J0717, we use the strong lensing model of Limousin et al. (2016), which uses 55 multiply-imaged systems found in the complete HFF optical and NIR data.

3.5.2 A1689 Lensing Model

As in A14, the lens model that we use for A1689 is from Limousin et al. (2007). Similar to the mass reconstruction techniques for the HFF clusters, Limousin et al. (2007) optimize a parametric model implemented in the `Lenstool` using 32 multiply imaged systems behind A1689. Their optimized lens model for A1689 is a composite of two large-scale halos and the subhalos of cluster member galaxies.

3.5.3 Multiply Imaged Systems

Finding more multiply imaged systems is critical for improving a lens model, as the lens model is constrained by the location and redshift of these systems. In addition, identifying the multiple images is important as we need to remove them from the galaxy number counts. We run `Lenstool` using each previously described lens model as an input, to look for the potential counter-images for each lensed galaxy in the sample.

Currently, there is no automated process for identifying multiple imaged systems. Here, we summarize the approach that we took to find new multiply imaged systems. 1) We run `Lenstool` entering the coordinates and the photometric redshift of each galaxy to predict the location of its potential counter-images. In this step, `Lenstool` first de-lenses the galaxy image to its original position in the source plane at the given photometric redshift, and then re-lenses it back to all of the possible multiple image positions in the image plane. 2) We search for the objects with the same color and symmetry in the morphology near the predicted positions. 3) If we find any nearby candidate from step 2, we then repeat

the first step to check if the potential counter-images of the candidate match with the first object. 4) Finally, we require the same photometric redshifts (within 1σ accuracy), for all of the newly found multiple images. This final criterion exhibits the importance of covering rest-frame UV wavelengths, which enables us to identify the Lyman break to distinguish the high redshift objects (in this case $1 < z < 3$) from the lower redshift interlopers, since both often have flat, featureless SEDs at rest-frame optical wavelengths.

Following this procedure for all the galaxies, we find 5 and 3 new multiply imaged systems behind A1689 and MACSJ0717, respectively. Our new findings in cluster MACSJ0717 added new systems 21, 80 and 82 to the list reported in Limousin et al. (2016). We introduce the new A1689 multiply imaged systems in appendix A3.

3.6 Sample Selection

We use the photometric redshift estimates to construct our galaxy samples in three redshift ranges of $1.0 < z < 1.6$, $1.6 < z < 2.2$ and $2.2 < z < 3.0$. To ensure the reliability of our photometric redshifts and to avoid selecting spurious objects in the sample, we require 3σ detections in the detection filter and the rest-frame 1500 Å filter. The selection criteria for the lower redshift range are:

a. $1.0 < z_{phot} < 1.6$

b. $S/N > 3$ in the F275W and F336W bands.

selecting 70, 134 and 93 candidates in A1689, A2744 and MACSJ0717, respectively. The selection criteria for the middle redshift range are:

a. $1.6 < z_{phot} < 2.2$

b. $S/N > 3$ in the F336W and F435W (F475W) bands for the HFFs (A1689).

selecting 128, 121 and 69 candidates in A1689, A2744 and MACSJ0717, respectively. And finally, the selection criteria for the higher redshift range are:

a. $2.2 < z_{phot} < 3.0$

b. $S/N > 3$ in the F435W and F606W bands for the HFFs.

selecting 176 and 102 galaxies in the A2744 and MACSJ0717 fields, respectively. We should note that we do not include data from A1689 for the highest redshift ($z \sim 2.6$) analysis because, due to the cluster redshift of $z = 0.18$, the Balmer break of faint cluster members (like globular clusters, Alamo-Martínez et al., 2013) can mimic the Lyman break at $z \sim 3$.

In total, we have 297, 318 and 278 candidates at $1 < z < 1.6$, $1.6 < z < 2.2$ and $2.2 < z < 3.0$, respectively. As explained in Section 3.5.3, we must clean our samples of multiple images. Among each multiply imaged system, we keep the brightest image and remove the rest of the images from our samples. However, if the brightest image has a magnification higher than 3.0 magnitudes, we then select the next brightest image. This condition on magnification is considered to ensure the reliability of the magnification value predicted from the lensing models.

Furthermore, to ensure purity of the samples, we consider different possibilities of contamination in the photometric redshift selected samples. First, to find possible contamination from stars, we use the Pickles (1998) stellar spectra library to predict stellar colors for a variety of stars and compare with the color of our candidate galaxies. In the case of similar colors, we visually inspect the objects. We found only 1 ($\sim 0.3\%$), 2 ($\sim 0.6\%$) and 0 stars in the $1.0 < z < 1.6$, $1.6 < z < 2.2$ and $2.2 < z < 3.0$ samples, respectively. We also visually inspect all of the galaxies to exclude objects associated with diffraction spikes and nearby bright galaxies. The contamination is only 2 ($\sim 0.7\%$), 3 ($\sim 0.9\%$) and 0 for the $1.0 < z < 1.6$, $1.6 < z < 2.2$ and $2.2 < z < 3.0$ samples, respectively. Finally, after excluding all of the multiple images and the contamination, we have 277, 269 and 252 galaxies at $1.0 < z < 1.6$, $1.6 < z < 2.2$ and $2.2 < z < 3.0$, respectively.

With the aim to measure the UV luminosity function, we use the F336W, F435W and F606W bands for the HFFs and F336W and F475W bands for the A1689 samples to measure

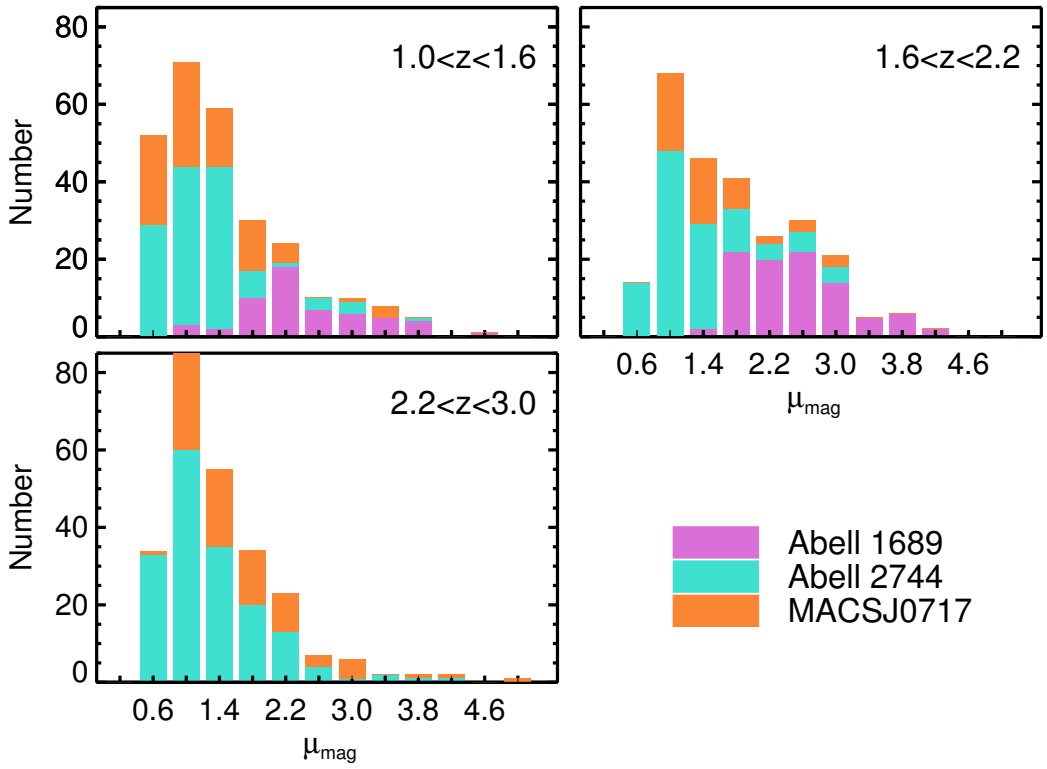

Figure 3.2: The magnification distribution of galaxies expressed in magnitude units. The purple, orange and cyan colors show the number of candidate galaxies for each magnification bin on A1689, A2744 and MACSJ0717, respectively. These clusters provide a large range of magnifications, with higher values mostly from A1689 (see the text).

the absolute magnitude at rest-frame 1500 Å ($M_{UV} = M_{1500}$) at redshifts $1.0 < z < 1.6$, $1.6 < z < 2.2$ and $2.2 < z < 3.0$, respectively. As we did in A14, we determine the intrinsic absolute magnitudes of M_{1500} by applying the magnification corrections computed from the lens models discussed in Section 3.5.

$$M_{1500} = m + \mu_{\rm mag} - 5\log(d_L/10\ {\rm pc}) + 2.5\log(1+z) \tag{3.1}$$

Where $\mu_{\rm mag}$ is the predicted magnification in magnitude units from the lensing model of each cluster. We limit our samples to galaxies brighter than $M_{1500} < -12.5$ magnitudes, to ensure a reliable absolute magnitude measurement. All of the galaxies brighter than this

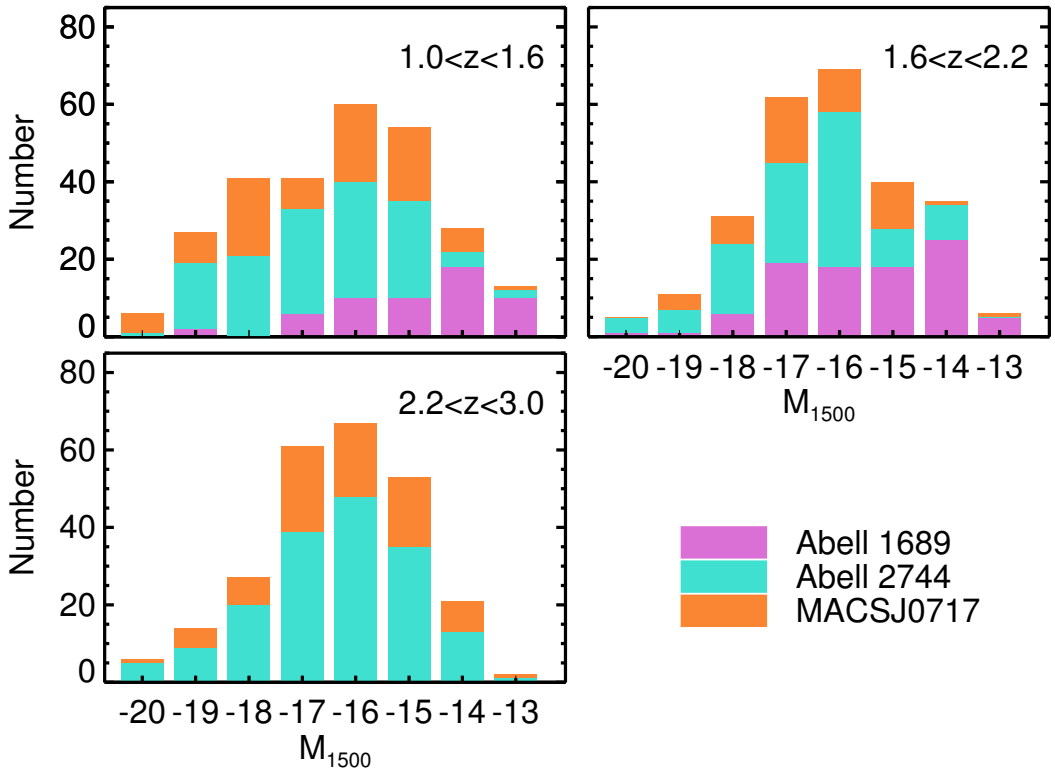

Figure 3.3: The intrinsic absolute UV magnitude (i.e., corrected for the lensing magnification) distribution of all galaxies in our three redshift slices. The colors are similar to Figure 3.2 and they show the number of candidate galaxies for each absolute magnitude bin. We cover a large luminosity range by combing the HFFs with A1689, which finds the faintest galaxies ($M_{1500} > -14.5$).

limit have magnification uncertainty from lensing models below 0.5 magnitudes with mean value of 0.03 magnitudes. But the galaxies fainter than $M_{1500} > -12.5$ have magnification uncertainties above 2.0 magnitudes. This limit excludes 7 (2.5%), 10 (3.7%) and 1 (0.4%) galaxies from the $1.0 < z < 1.6$, $1.6 < z < 2.2$ and $2.2 < z < 3.0$ samples, respectively.

Figure 3.2 shows the distributions of magnifications for galaxies in three photometric redshift samples. The magnification values range between $\mu_{\rm mag} = 0.5 - 4.8$ (equivalent to $1.58 - 83$ in flux density units) with median values of $\mu_{\rm mag} = 1.27$, 1.61 and 1.24 for $z \sim 1.3$, 1.9 and 2.6 samples, respectively. As shown in Figure 3.2, most of the highly magnified galaxies ($\mu_{\rm mag} > 2.5$) in the $z \sim 1.3$ and $z \sim 1.9$ samples are from A1689. We note

that, because A1689 has a large Einstein radius, it provides high magnification (i.e., median $\mu_{\rm mag} = 2.0$) over large area in the source plane. Therefore, objects with high magnification in A1689 are not required to be close to the critical lines, where the magnification formally diverges. For example, the galaxies with high magnification ($\mu_{\rm mag} = 2.5 - 4$) in the A1689 sample are on average 15 arcsec (with median of 10 arcsec) from the critical lines whose positions are predicted with a precision of 2.87 arcsec by the lens model (Limousin et al., 2007). Therefore, these magnification estimates are not strongly affected by uncertainties in the location of the critical lines.

In Figure 3.3, we show the histograms of absolute UV magnitudes for each lensing cluster in three redshift bins. This figure emphasizes the importance of including A1689, since it dominates the number of galaxies at the faintest magnitudes, $M_{1500} > -14.5$.

3.7 Completeness Simulations

In order to connect the observed galaxies to the underlying population of all star-forming galaxies, we need to precisely estimate the completeness of our sample. This is more critical for low luminosity bins, where the galaxies are close to the detection limits. An approach commonly used in the blank field studies to estimate the completeness (e.g., Oesch et al., 2010a; Grazian et al., 2011; Bowler et al., 2015; Finkelstein et al., 2015), is to generate artificial galaxies with properties similar to the real galaxies and then apply an identical selection technique as for the observed candidates to calculate the fraction of recovered simulated galaxies in a given magnitude and redshift bin. This technique is also applicable in gravitationally lensed studies (e.g., Atek et al., 2015b,a). However, one needs to incorporate the added complexity due to the strong lensing amplification.

In this work, we adopt a Monte Carlo simulation following the methodology presented in detail in A14. Here, we briefly describe these completeness simulations, and we provide additional details where our approach deviates from what was done in A14.

We compute the completeness in a 3-D grid of redshift, magnitude and lensing magnification. For each point in this 3-D space, we assign a redshifted and magnified template galaxy spectrum, which is generated by Bruzual and Charlot (2003) (hearafter BC03) synthetic stellar population models assuming a 0.2 $Z_{\odot}$ metallicity and an age of 100 Myr. A detailed justification for these assumptions is given in A14. The SED is dust attenuated using the Calzetti extinction curve (Calzetti et al., 2000) and a random color excess, E(B-V), value taken from a Gaussian distribution centered at 0.15 as measured in A14 and other studies (Steidel et al., 1999; Reddy and Steidel, 2009; Hathi et al., 2013) with a standard deviation of 0.1. In order to understand the effect of a changing reddening distribution, we also examined the completeness for a model in which the dust reddening linearly decreases toward fainter luminosities. To derive this linear function, we measured the relation between UV spectral slope and M_{1500} magnitude for our galaxies and we calculate the dust reddening values assuming a Calzetti reddening curve. The final completeness corrections from this examination show only negligible changes relative to our original simulations. [9]

We then create transmission curves (as a function of wavelength) for 300 lines of sight through the intergalactic medium (IGM) at that redshift. The IGM opacity is calculated using a Monte Carlo simulation to randomly place Hydrogen absorbers in each line of sight as described in A14 (see also Siana et al., 2008a). Our completeness simulation is modified relative to A14 in the following two ways.

Updating the Size Distribution of Star-forming Galaxies: One of the key factors in estimating the incompleteness is the assumed size distribution for galaxies. As shown in Grazian et al. (2011), the completeness correction at low luminosities depends critically on the adopted size distribution in the simulation, as using too small (large) a size distribution can cause one to over- (under-) estimates the completeness. As reported in various observational studies (e.g., Bouwens et al., 2004; Ferguson et al., 2004; Huang et al., 2013), the rest-frame UV sizes of high redshift Lyman break galaxies follow a log-normal distribution.

[9] We note that for the same experiment, the effective volumes of the LBG samples (see Appendix A2) show slightly larger change at bright luminosities. This can be understood by considering that the color-color criteria select against very reddened galaxies. However, our final estimates of the best-fit LFs (for both sample selections) are robust against these different initial assumptions of dust reddening distribution.

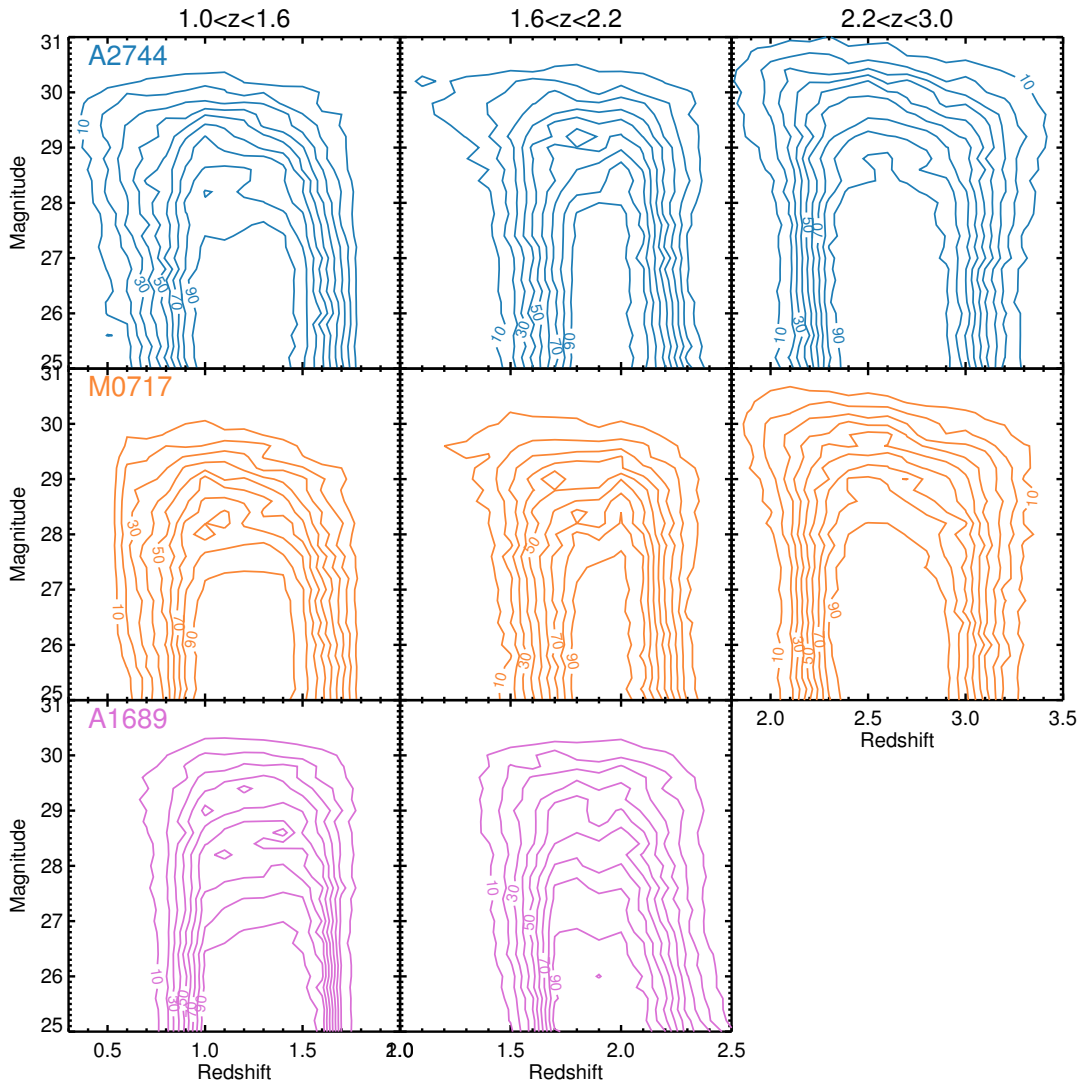

Figure 3.4: Completeness as a function of intrinsic apparent magnitude on the y-axis and redshift on the x-axis. The blue, orange and purple contours show the completeness simulation values for A2744, MACSJ0717 and A1689, respectively. The left, middle and right columns represent the completeness contours for photometric redshift samples at $1.0 < z < 1.6$, $1.6 < z < 2.2$ and $2.2 < z < 3.0$, respectively. These contours are drawn for magnification of $\mu_{\rm mag} = 2.0$ magnitudes.

In a recent work, Shibuya et al. (2015) measured the size distribution of a large sample of galaxies at $0 < z < 8$, using the 3D-HST and CANDELS data. They showed that the circularized effective radius[10] (r_e) distribution of star-forming galaxies at $0 < z < 8$ is well represented by a log-normal distribution whose median decreases toward high redshifts (at a given luminosity) and changes with luminosity as $r_e \propto (L_{UV})^{\alpha}$ with $\alpha = 0.27$ for all redshifts. For our completeness simulation, we generate random galaxy sizes at each luminosity and redshift using the corresponding log-normal distribution from Table 8 in Shibuya et al. (2015). We extrapolate their measurements below $M_{UV} < -16$. Using the randomly selected r_e values, we then adopt a Sersic profile with index n=1.5 as suggested by Shibuya et al. (2015). Other LF studies at both low (Oesch et al., 2010a) and high redshifts (Oesch et al., 2010b; Grazian et al., 2011; Atek et al., 2015a; Finkelstein et al., 2015) have also assumed a log-normal size distribution. Our size distribution assumption in this work is different from A14, where we assumed a normal (not a log-normal) distribution centered at 0.7 kpc with a standard deviation of 0.2 kpc (Law et al., 2012).

Updating the The Effect of Lensing Magnification and Shear: The next step in the simulation is to add the lensing effect by amplifying the flux and enlarging the size of the galaxies. The way that gravitational lensing distorts the image of a galaxy is a combination of convergence (i.e., κ, stretching a source isotropically) and shear (i.e., γ, stretching a source along a privileged direction). As discussed in other works (e.g., Oesch et al., 2015), it is crucial to account for the effect of lensing distortion. In A14, we did include the effect of convergence in distorting our simulated galaxies. For this work, we do a more complete and complex analysis such that the shape of the final distorted image can be described using tangential ($\mu_t = (1 - \kappa - \gamma)^{-1}$) and radial ($\mu_r = (1 - \kappa + \gamma)^{-1}$) magnification.

[10] The circularized effective radius is defined as $r_e = r_{e,major}\sqrt{q}$, where $r_{e,major}$ is the half-light radius along the semi-major axis and q is the axis ratio. The circularized radius has been extensively used in other high redshift size measurements (e.g., Mosleh et al., 2012; Ono et al., 2013)

As formulated in Bartelmann (2010), a circular source with a circularized radius of r_e becomes an elliptical image with semi-major(a) and -minor(b) axises as below:

$$a = \mu_r r_e \tag{3.2}$$

$$b = \mu_t r_e \tag{3.3}$$

We use the lensing models to construct the μ_t and μ_r maps at source plane for desired redshifts. We then use these maps to select random (μ_t, μ_r) pairs and distort the image of our simulated galaxies. We also increase the flux with a magnification factor of $\mu = \mu_t.\mu_r$. To mimic the same condition as real galaxies, we should note that we exclude the large cluster members from our source plane area reconstruction as the real galaxies behind these low-z intervening galaxies can not be observed.

The corresponding synthetic SED assigned to each simulated source is multiplied by the same filter curves as used in the observations to generate artificial catalogs. We then add random photometric noise to the distorted image of each galaxy for each band. To detect the galaxies and generate the artificial catalogs, we use the same detection parameters as we used in `SExtractor` for our real galaxies.

Finally, for each cell of the 3-D grid, we have a `SExtractor` output catalog for 300 artificially created galaxies in random lines of sight, with random sizes and dust attenuation values sampled from the corresponding distributions explained above. We then run the `EAZY` code on these simulated catalogs and adopt the same selection criteria as we did for the real sources (see Section 3.6). Consequently, we calculate the completeness correction factor, $C(m, z, \mu_{\rm mag})$, as a function of intrinsic apparent magnitude (i.e., before magnification, m), redshift (z) and magnification ($\mu_{\rm mag}$) by counting the fraction of recovered artificial galaxies. Figure 3.4 shows the completeness contours as a function of intrinsic apparent magnitude, m, on the y-axis and redshift on the x-axis for each redshift interval and for each lensing cluster with different colors. The contours are plotted for a magnification of $\mu_{\rm mag} = 2.0$ mag. We can see the difference between HFFs and A1689 completeness values at the lower redshift

range ($1.0 < z < 1.6$), where F225W photometry in A1689 helps to better constrain the redshift and avoids contamination from galaxies with input redshifts below 1.0. As seen in this figure, the recovered redshift distribution from completeness simulations is in agreement with our targeted redshift ranges for each sample.

3.7.1 The Effective Survey Volume

We incorporate the completeness corrections in the computation of the effective survey volume, V_{eff}, in each magnitude bin as below:

$$V_{\rm eff}(m) = \int_0^\infty \int_0^\infty \frac{dV_{com}}{dz d\Omega} C(z, m, \mu) \Omega(\mu, z) {\rm d}z {\rm d}\mu \tag{3.4}$$

where dV_{com} is the comoving volume element at redshift z per unit area, $d\Omega$. In this equation, $C(z, m, \mu)$ is the completeness function that depends on redshift (z), intrinsic apparent magnitude (m) and magnification (μ). $\Omega(\mu, z)$ is the area element in the source plane at z which is magnified by a factor of μ. We run `Lenstool` for each aforementioned cluster mass model to generate the de-lensed magnification maps at different redshifts. We then use these maps to estimate the $\Omega(\mu, z)$ of each cluster at each redshift. Similar to our completeness simulations (see Section 3.7), we subtract the area occupied by the large cluster members from our source plane area reconstruction.

Figure 3.5 represents the effective volumes versus the absolute magnitude at 1500 Å, M_{UV}, for each cluster at three redshift ranges. This plot clearly shows the importance of including A1689 for finding the faintest galaxies ($M_{UV} > -14.5$).

We should emphasize that the small volumes at faint luminosities are not necessarily due to a large incompleteness but because of small area available at these magnitudes. For the volume calculation at each magnitude, unlike the field studies where the full area is available, here only a portion of area (i.e., effective area) with enough magnification (i.e., minimum magnification required for detection at each magnitude) is used. Therefore, at very faint luminosities, only a tiny fraction of area is available for the volume measurements.

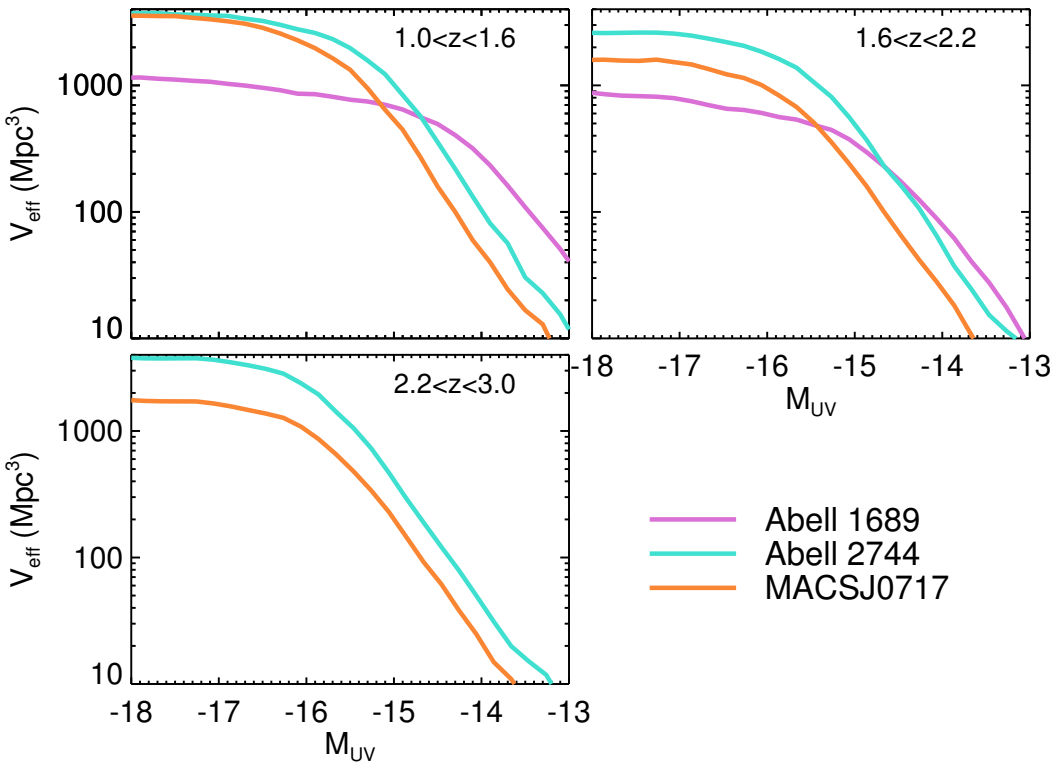

Figure 3.5: The effective volume estimates at each redshift slice in each field. The HFF clusters provide a large volume over faint magnitudes ($M_{UV} < -15.5$), while the A1689 cluster enables to probe even fainter galaxies ($M_{UV} > -14.5$) beyond the HFFs magnification limits.

3.8 Luminosity Function of Photometric Redshift Samples

Using the effective volumes, we construct the UV luminosity function of our photometric redshift selected galaxies at the peak epoch of cosmic star formation rate density. To be consistent with other studies at the same redshift ranges (e.g., Oesch et al., 2010a; Parsa et al., 2016) and at higher redshifts (e.g., Bouwens et al., 2007; Finkelstein et al., 2015), we measure the UV luminosities at rest-frame 1500 Å.

The galaxy luminosity function is commonly fitted by a Schechter function (Schechter, 1976) characterized by an exponential behavior at luminosities brighter than a characteristic magnitude, M^*, and a power-law at the faint end with slope α as below:

$$\phi(M) = 0.4\ln(10)\phi^* 10^{-0.4(M-M^*)(1+\alpha)} e^{-10^{-0.4(M-M^*)}} \tag{3.5}$$

where ϕ^* is the normalization of this function.

In this section, we first calculate and compare binned UV LFs of each cluster field and then we find the best-fit Schechter parameters for the combined LF using a maximum likelihood approach on the unbinned data.

3.8.1 The Binned UV LFs

The LF at each M_{1500} bin is derived using the measured V_{eff} values which account for the completeness corrections. This is the commonly used V_{eff} method (e.g., A14, Oesch et al., 2010a) where one calculates the number density of galaxies in each bin by dividing the number of galaxies in the corresponding absolute magnitude bin by the effective volume of that bin. But the effective volume might change significantly from one side of the magnitude bin to the other. Therefore, we estimate the effective volume for each individual galaxy and then sum up over all the galaxies within each bin, as shown below:

$$\phi(M_i)dM_i = \sum_{j=1}^{N} \frac{1}{V_{\rm eff}(M_j)} \tag{3.6}$$

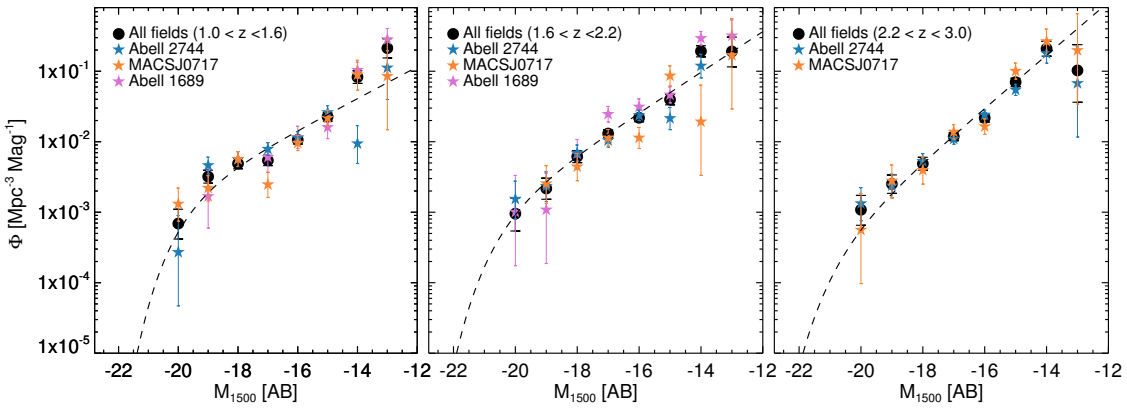

Figure 3.6: The rest-frame UV luminosity function for each lensing cluster at $1.0 < z < 1.6$, $1.6 < z < 2.2$ and $2.2 < z < 3.0$ in the left, middle and right panels, respectively. The purple, blue and orange stars show the binned LF of A1689, A2744 and MACSJ0717, respectively. The black circles are the binned LFs after combining all of the three lensing clusters. The dashed line is the best-fit Schechter function (see Section 3.8.2).

As illustrated in Figure 3.6, we estimate the binned LFs of each lensing field separately as well as a total LF combining all of the cluster fields. For the combined LF, the V_{eff} is a sum of the effective volumes over all of the cluster fields.

For each bin with a large number of galaxies ($N > 50$), we assign an uncertainty of $\frac{\phi_i}{\sqrt{N}}$ using Poisson statistics. In the case where less than 50 galaxies are in the bin, we compute the Poisson approximation, Δ_P, from Gehrels (1986) and assign an uncertainty of $\frac{\phi_i \Delta_P}{N}$ to each bin. Each bin has a width of $\Delta M_{UV} = 1$ magnitude and our faintest magnitude bin is centered at $M_{UV} = -13$ (i.e., a magnitude cut at $M_{UV} = -12.5$, see Section 3.6). The values of the binned LFs, and the number of galaxies at each bin are listed in Table 3.2.

The binned LFs are good for visualization but poor for inference because of arbitrary bin widths, bin centers and loss of information within each bin. Therefore, instead of using binned estimators, we use an unbiased, unbinned maximum likelihood estimator as explained in the next section.

Table 3.2. Binned UV LFs

z	M_{UV}	Number of sources	ϕ ($\times 10^{-2}$Mpc^{-3}mag^{-1})
		Photometric redshift LFs	
$1.0 < z < 1.6$	-20.0	6	$0.069^{+0.041}_{-0.027}$
	-19.0	27	$0.320^{+0.074}_{-0.061}$
	-18.0	41	$0.490^{+0.089}_{-0.076}$
	-17.0	41	$0.543^{+0.099}_{-0.084}$
	-16.0	60	$1.064^{+0.137}_{-0.137}$
	-15.0	54	$2.266^{+0.308}_{-0.308}$
	-14.0	28	$8.275^{+1.877}_{-1.554}$
	-13.0	13	$21.279^{+7.693}_{-5.826}$
$1.6 < z < 2.2$	-20.0	5	$0.095^{+0.064}_{-0.041}$
	-19.0	11	$0.217^{+0.087}_{-0.064}$
	-18.0	31	$0.615^{+0.131}_{-0.110}$
	-17.0	62	$1.307^{+0.166}_{-0.166}$
	-16.0	69	$2.186^{+0.263}_{-0.263}$
	-15.0	40	$3.964^{+0.731}_{-0.624}$
	-14.0	35	$19.223^{+3.828}_{-3.235}$
	-13.0	6	$19.104^{+11.412}_{-7.578}$
$2.2 < z < 3.0$	-20.0	6	$0.108^{+0.065}_{-0.043}$
	-19.0	14	$0.252^{+0.087}_{-0.066}$
	-18.0	27	$0.488^{+0.113}_{-0.093}$
	-17.0	61	$1.186^{+0.152}_{-0.152}$
	-16.0	67	$2.170^{+0.265}_{-0.265}$
	-15.0	53	$7.003^{+0.962}_{-0.962}$
	-14.0	21	$20.915^{+5.637}_{-4.532}$
	-13.0	2	$10.271^{+13.547}_{-6.635}$
		LBG LFs	
$z \sim 1.65$	-18.0	3	$0.527^{+0.513}_{-0.287}$

Table 3.2 (cont'd)

z	M_{UV}	Number of sources	ϕ ($\times 10^{-2}$Mpc^{-3}mag^{-1})
	-17.0	4	$0.733^{+0.579}_{-0.351}$
	-16.0	5	$1.329^{+0.899}_{-0.574}$
	-15.0	2	$1.150^{+1.517}_{-0.743}$
	-14.0	3	$8.566^{+8.332}_{-4.663}$
	-13.0	1	$10.477^{+24.098}_{-8.665}$
$z \sim 2.0$	-20.0	3	$0.058^{+0.057}_{-0.032}$
	-19.0	10	$0.199^{+0.085}_{-0.062}$
	-18.0	34	$0.768^{+0.156}_{-0.131}$
	-17.0	50	$1.617^{+0.263}_{-0.228}$
	-16.0	40	$3.556^{+0.656}_{-0.560}$
	-15.0	20	$5.736^{+1.592}_{-1.271}$
	-14.0	13	$20.106^{+7.269}_{-5.504}$
	-13.0	2	$25.922^{+34.192}_{-16.746}$
$z \sim 2.7$	-20.0	6	$0.112^{+0.067}_{-0.045}$
	-19.0	10	$0.186^{+0.079}_{-0.058}$
	-18.0	21	$0.409^{+0.110}_{-0.089}$
	-17.0	46	$1.309^{+0.223}_{-0.192}$
	-16.0	37	$4.218^{+0.814}_{-0.691}$
	-15.0	14	$7.796^{+2.690}_{-2.060}$
	-14.0	5	$32.106^{+21.716}_{-13.870}$
	-13.0	1	$24.187^{+55.631}_{-20.003}$

3.8.2 The Unbinned Maximum Likelihood Estimator

In this section, we explain our methodology to estimate the best Schechter function parameters by maximizing the likelihood function of the unbinned data. The standard maximum likelihood (MLE) technique was first used by Sandage et al. (1979, STY79), and later by many other studies to derive the best-fit parameters for UV LFs at intermediate redshifts (A14), high redshifts (e.g., McLure et al., 2013; Bouwens et al., 2015) and for the Hα LF (Mehta et al., 2015). Here, we adopt a similar approach as in A14 where we modify the standard STY79 MLE technique to account for uncertainties in the measurements of the absolute magnitude. This modified methodology is also used in Mehta et al. (2015).

In the MLE technique, the best fit is found through maximizing the joint likelihood function L defined as below.

$$\mathcal{L} = \prod_{i=1}^{N} P(M_i) \tag{3.7}$$

where in the standard MLE, $P(M_i)$ defined as below:

$$P(M_i) = \frac{\phi(M_i)V_{\rm eff}(M_i)}{\int_{-\infty}^{M_{\rm limit}} \phi(M)V_{\rm eff}(M){\rm d}M} \tag{3.8}$$

where N is the total number of objects in each sample. $P(M_i)$ is the probability of finding a galaxy with absolute magnitude M_i in a corresponding effective volume, $V_{eff}(M_i)$. We calculate this probability value for all of the galaxies in each of our samples. $\phi(M_i)$ is the parametric luminosity function assuming a Schechter function. The M_{limit} is defined for each sample to be the faintest absolute magnitude (i.e., corrected for the magnification). The M_{limit} values are -12.88, -12.12 and -13.40 for z=1.3, 1.9 and 2.6 samples, respectively.

To incorporate absolute magnitude uncertainties in the LF analysis, we assume a Gaussian probability distribution $G(M|M_i, \sigma_i)$ for each object centered at the object's absolute magnitude M_i and a standard deviation equal to the object's absolute magnitude uncertainty σ_i. We then modify the Equation 4.2 as below:

$$P(M_i) = \frac{\int_{-\infty}^{+\infty} \phi(M)V_{\rm eff}(M)G(M|M_i, \sigma_i){\rm d}M}{\int_{-\infty}^{M_{\rm limit}} \phi(M)V_{\rm eff}(M){\rm d}M} \tag{3.9}$$

with

$$G(M|M_i, \sigma_i) = \frac{1}{\sqrt{2\pi}\sigma_i} exp(-\frac{(M - M_i)^2}{2\sigma_i^2}) \tag{3.10}$$

As also considered in A14, for our lensed galaxies, the total uncertainty, σ_i, of intrinsic absolute magnitude is due to the uncertainty in photometric measurements (σ_m), photometric redshifts (σ_z) and the lens models (σ_{model}). Below, we investigate in detail these different sources of uncertainties.

a. σ_m: The photometric uncertainties are calculated using the `SExtractor` output of flux uncertainties.

b. $\sigma_{z(total)}$: The photometric redshift uncertainty, σ_z, for each galaxy is computed as 1σ confidence interval of its redshift probability distribution from `EAZY`. This redshift uncertainty impacts the measured intrinsic absolute magnitude in two ways. First, since the distance modulus is dependent on the redshift, we estimate the effect of redshift uncertainty on the absolute magnitude through an error propagation of Equation 3.1. Second, the magnification value of each galaxy is estimated through running `Lenstool` while incorporating its photometric redshift as an input. Therefore, a redshift uncertainty causes a magnification uncertainty, $\sigma_{\mu(z)}$. To estimate $\sigma_{\mu(z)}$ for each galaxy, we run `Lenstool` for 100 random redshifts generated from a Gaussian redshift distribution centered at the galaxy's photometric redshift with standard deviation equal to σ_z. The distribution of output random magnifications for each galaxy is fitted with a Gaussian function to derive $\sigma_{\mu(z)}$. Because σ_z and $\sigma_{\mu(z)}$ are correlated, we calculate the total redshift uncertainty as a sum over them, $\sigma_{z(total)} = \sigma_z + \sigma_{\mu(z)}$

c. $\sigma_{\mu(model)}$: The final source of uncertainty is related to the lensing models. To estimate this uncertainty, we randomly sample the parameter space of each lens model. A detailed description of these measurements is given in A14.

We calculate the total uncertainty of intrinsic absolute magnitude by adding all these uncertainties in quadrature.

Substituting Equation 3.9 in Equation 3.7, we calculate the likelihood function over a grid of faint-end slope (α) and characteristic magnitude (M^*). The small survey areas probed in this study, limits the number of bright galaxies (i.e., $M < M^*$). Therefore, to constrain M^*, we combine our $z \sim 1.3$ and $z \sim 1.9$ samples with the samples from a wider survey from Oesch et al. (2010a). To be consistent with our samples, we use their photometric redshift selected galaxies at $1.0 < z < 1.5$ and $1.5 < z < 2.0$.

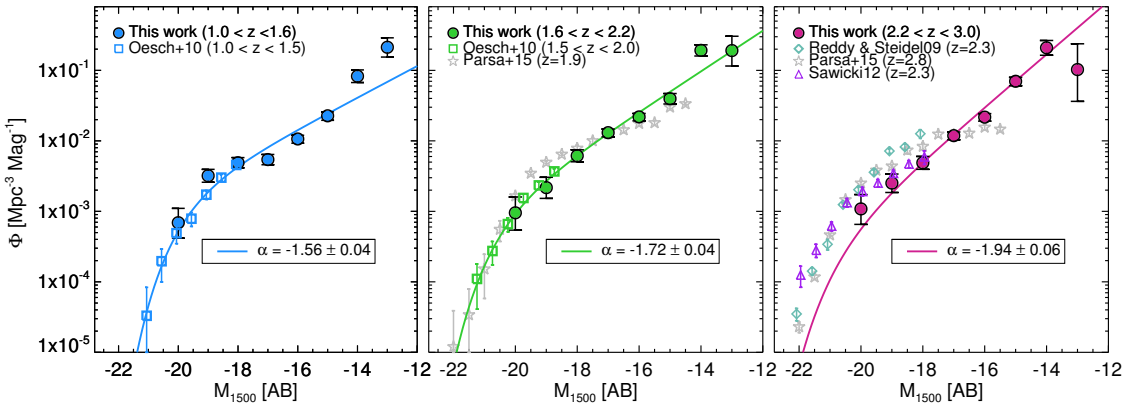

Figure 3.7: Rest-frame UV luminosity functions at $z \sim 1.3$ (left), $z \sim 1.9$(middle) and $z \sim 2.6$(right). The blue, green and red circles are our binned LFs combining all three lensing clusters (see Section 3.8.1). The blue and green squares are the LFs from Oesch et al. (2010a) at $1.0 < z < 1.5$ and $1.5 < z < 2.0$, respectively, of which the individual data were used for our MLE fitting. The light blue diamonds are the LFs from Reddy and Steidel (2009) based on a BX selected sample of star-forming galaxies. The gray stars and purple triangles are the results from Parsa et al. (2016) (photometric redshift selection) and Sawicki (2012) (BX selection), respectively. The solid line in all three panels shows our best Schechter fit through a MLE technique.

Table 3.3. Best-fit Schechter Parameters for UV LFs

z	α	M*	$\phi^*(10^{-3}\mathrm{Mpc}^{-3}\ \mathrm{mag}^{-1})$
Photometric redshift LF, MLE fitting			
$1.0 < z < 1.6$[a]	-1.56±0.04	-19.74±0.18	2.32±0.49
$1.6 < z < 2.2$[a]	-1.72±0.04	-20.41±0.20	1.50±0.37
$2.2 < z < 3.0$[b]	-1.94±0.06	-20.71±0.11(prior)	0.55±0.14
LBG LF, χ^2 fitting			
$z \sim 1.65$[c]	-1.50±0.16	-19.85±0.41	2.21±1.32
$z \sim 2.0$[d]	-1.80±0.06	-20.39±0.31	1.46±0.65
$z \sim 2.7$[e]	-2.01±0.08	-20.70(fixed)	0.48±0.15

[a]Maximum likelihood fit to the whole sample including individual galaxies from all three lensing clusters as well as the bright-end galaxies from Oesch et al. (2010a).

[b]Maximum likelihood fit to the individual galaxies from the HFF clusters assuming a Gaussian prior for M^* (see Section 3.8.2)

[c]χ^2 fitting to the binned data from A1689 as well as the bright-end LBGs from Oesch et al. (2010a)

[d]χ^2 fitting to the binned data from all three lensing clusters as well as the bright-end LBGs from Oesch et al. (2010a)

[e]χ^2 fitting to the binned data from the HFF clusters assuming a fixed M^* (see Section 3.9).

For our $2.2 < z < 3.0$ sample, our brightest LF bins are lower than the values from the literature. Furthermore, we do not have access to the individual galaxies from the literature. Therefore, we adopt a different approach to find the best-fit LF. We multiply the likelihood function by an M^* prior to compute the posterior function. Utilizing the best Schechter parameters reported in Reddy and Steidel (2009), we define the prior as a Gaussian function centered at -20.70 with standard deviation of 0.11. We should note that this discrepancy between the LFs at bright luminosities, is not due to our completeness correction, as our $z \sim 2.6$ sample is $> 90\%$ complete at these luminosities (see Figures 3.4 and 3.5). Considering that we only have two clusters at this redshift range, and consequently we probe a small area, it is not unlikely that this low number density may be due to a presence of an underdense region of galaxies. The reason that this under-density appears to

be affecting the bright end more than the faint end can be understood by different spatial clustering of the bright galaxies relative to the faint ones (e.g., Zehavi et al., 2005).[11]

The best estimates of Schechter parameters are derived via marginalization of posterior functions at all redshifts. Figure 3.7 shows the binned LFs along with our best MLE determinations at each redshift range. The best Schechter parameters are tabulated in Table 3.3. Our MLE estimates reveal steep faint-end slopes of $\alpha = -1.56 \pm 0.04$, -1.72 ± 0.04 and -1.94 ± 0.06 for $z \sim 1.3$, $z \sim 1.9$ and $z \sim 2.6$ samples, respectively. We emphasize that our estimate of the faint-end slope at $z \sim 2.6$ is mostly independent of our choice of the M^* prior, as we derive $\alpha = -1.97 \pm 0.06$ in the absence of a prior. Our steep LFs show no sign of turnover down to $M_{UV} = -12.5$ mag.

The contours in Figure 3.8 illustrate the correlation between the faint-end slope (α) and the characteristic magnitude (M^*). The best Shechter parameters derived through marginalization are shown with filled blue, green and red circles for $z \sim 1.3$, $z \sim 1.9$ and $z \sim 2.6$ samples, respectively. We are also overplotting our best LFs (filled black circles) from LBG samples (see Section 3.9). The red dashed contours show the Likelihood function at $z \sim 2.6$, before incorporating the M^* prior.

The systematic uncertainties – particularly in the size distribution assumption at faint luminosities – may affect the completeness corrections and thus the LF measurements at these magnitudes. This concern is also expressed in a recent paper by Bouwens (2016), where they measure very small sizes (160-240 pc) for ultra-faint galaxies ($M_{UV} = -15$) at $2 < z < 8$ and then discuss the possible effects due to uncertain size assumptions on the LF measurements. We should emphasize that they present their conclusions for a large redshift range of $z = 2 - 6$, while we expect the lower redshift galaxies ($z \sim 2$) to be on average larger than their high redshift counterparts (as seen at higher luminosities, Shibuya et al. (2015)). Our assumed size distribution for ultra-faint galaxies is the closest to the Bouwens (2016) measurements, relative to the other LF studies. We run some experiments

[11] In the future, when we complete the UV survey of HFFs, we will add 4 more clusters and consequently triple our sample size at $z = 2.6$. Therefore, our number density measurement for bright galaxies at this redshift would be more accurate.

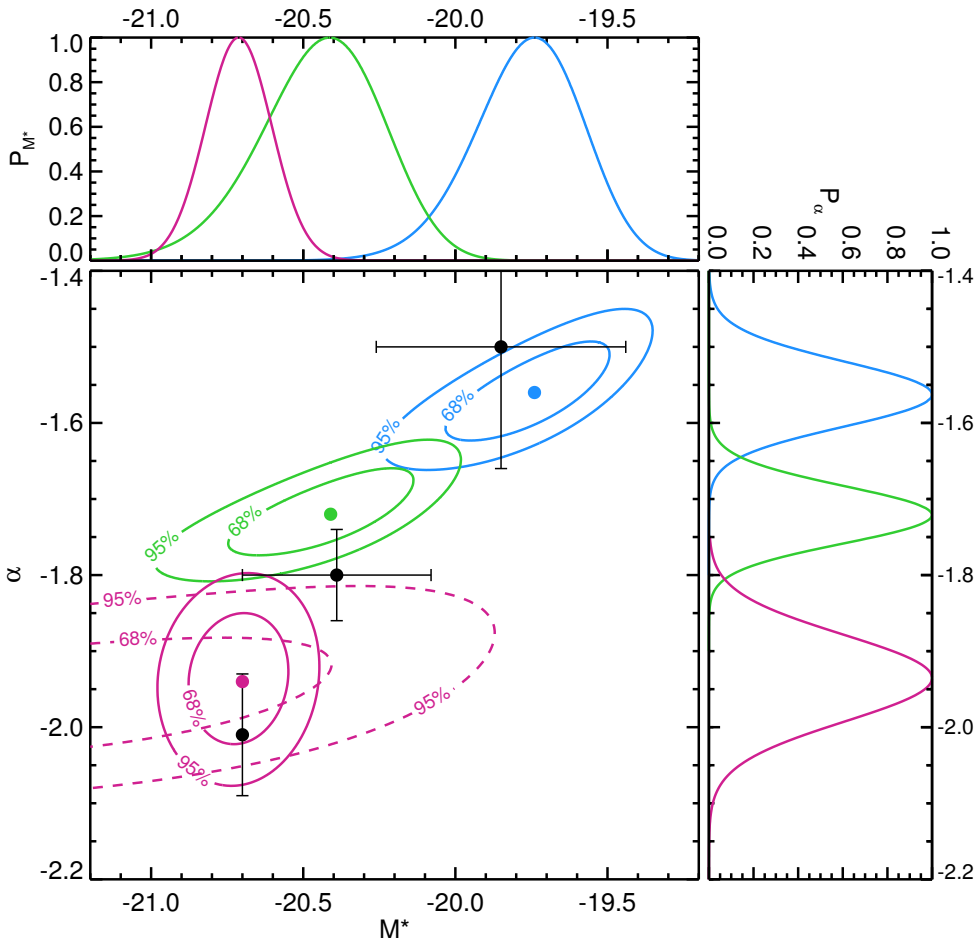

Figure 3.8: The 68% and 95% contours of the $z \sim 1.3$, $z \sim 1.9$ and $z \sim 2.6$ photometric redshift LFs are shown with blue, green and red colors, respectively. The red dashed line shows the contours for $z \sim 2.6$ LF before adding the M^* prior (see Section 3.8.2). The marginalized probability distribution of each parameter $P(\alpha)$ and $P(M^*)$ are also plotted on the right and top sides, respectively. The best-fit values of Schechter parameters for each LF is shown with a filled circle. The black filled circles with error bars denote the best-fit values for the LBG LFs (see Section 3.9).

to investigate whether the faint galaxies with large completeness corrections (i.e., where the systematic uncertainty dominates), are dictating our best-fit LFs by excluding all of our galaxies with completeness below 50%. This reduces the size of our $z \sim 1.3$, $z \sim 1.9$ and $z \sim 2.6$ samples by 33%, 53% and 44%, such that our final "complete" samples have 186, 127 and 141 galaxies, respectively. To be consistent, we also remove the corresponding volumes from our total volume estimates. We then re-fit the LFs and measure faint-end slopes of $\alpha = -1.55 \pm 0.06$, $\alpha = -1.69 \pm 0.07$ and $\alpha = -1.79 \pm 0.08$ at $1 < z < 1.6$, $1.6 < z < 2.2$ and $2.2 < z < 3.0$, respectively. These estimates are all steep and show the same trend of steeper slopes toward higher redshifts, though with slightly shallower slopes. We note that, although the $z \sim 1.3$ and $z \sim 1.9$ faint-end slopes measured from the "complete" sample are consistent with the slopes measured from the full sample, the $z \sim 2.6$ slope from the "complete" sample is significantly shallower by $\sim 1.5\times$ the individual errors added in quadrature (though the measurements aren't completely independent, so adding in quadrature will slightly overestimate the uncertainties). The probability of obtaining such a deviation in at least one of the three slope measurements is small (10%), and suggests that the systematic uncertainties are not negligible. Consequently, as also emphasized in Bouwens (2016), the size measurements of very faint galaxies will need to be more accurately determined for higher quality LF measurements.

3.9 Luminosity Function of LBG Samples

As discussed in Section 3.1, one of the goals of the present paper is to understand the effect of two widely used selection techniques. To this end, we have also performed a parallel determination of the UV luminosity function based on the Lyman break "dropout" selection at equivalent redshift ranges. A complete description of our color-color selection, sample contamination and the completeness simulation for dropouts is given in Appendix A1. As explained there, our LBG samples consist of 19 F225W-, 178 F275W- and 142 F336W-dropouts at $z \sim 1.65$, $z \sim 2.0$ and $z \sim 2.7$, respectively. We note that our LBG samples

have fewer galaxies than our photometric redshift samples, because we require 5σ detection in the detection filter for these samples (see Appendix A1), whereas the photometric redshift samples only require a 3σ detection (see Section 3.6). To ensure accurate detection of a break, we restrict our sample to objects where the imaging depth is sufficient to detect at least a one magnitude break (at 1 sigma) between the dropout filter (F225W, F275W, and F336W at $z \sim$1.65, 2.0, and 2.7, respectively) compared to the adjacent longer wavelength filter. This cut only removes two galaxies from the A2744 F336W-dropout LF and it does not change the rest of the LBG samples.

The effective volume including the completeness corrections is calculated for these samples using Equation 3.4. In order to estimate the binned UV LF for our LBG samples, we use the same methodology as we used for our primary photometric redshift samples. Similarly, we restrict our dropout samples to galaxies with $M_{1500} < -12.5$ for the same reasons that were mentioned before (see Section 3.6). This limit excludes 1 ($\sim 5.3\%$), 6 ($\sim 3.4\%$) and 0 galaxies from the F225W-, F275W-, F336W-dropout LFs, respectively. Finally, we have 18, 172 and 140 galaxies for the $z \sim 1.65$, $z \sim 2.0$ and $z \sim 2.7$ LBG LFs, respectively.

Furthermore, to constrain the bright-end of our F225W and F275W-dropout LFs, we incorporate the binned measurements from Oesch et al. (2010a) LBG samples. Here, we do not use the MLE technique because we do not have individual measurements for all of these bright-end LBG samples. We determine the best Schechter parameters only using the simple χ^2 technique, considering that these two methods of fitting (MLE vs χ^2) show good agreement for the photometric redshift LFs. For our F336W-dropout LF, we only fit to our binned data keeping the characteristic magnitude $M*$ at a fixed value of -20.7, similar to what we used for our $z \sim 2.6$ photometric redshift LF. The binned values and the best-fitting Schechter parameters for the LBG LFs are given in Tables 3.2 and 3.3, respectively.

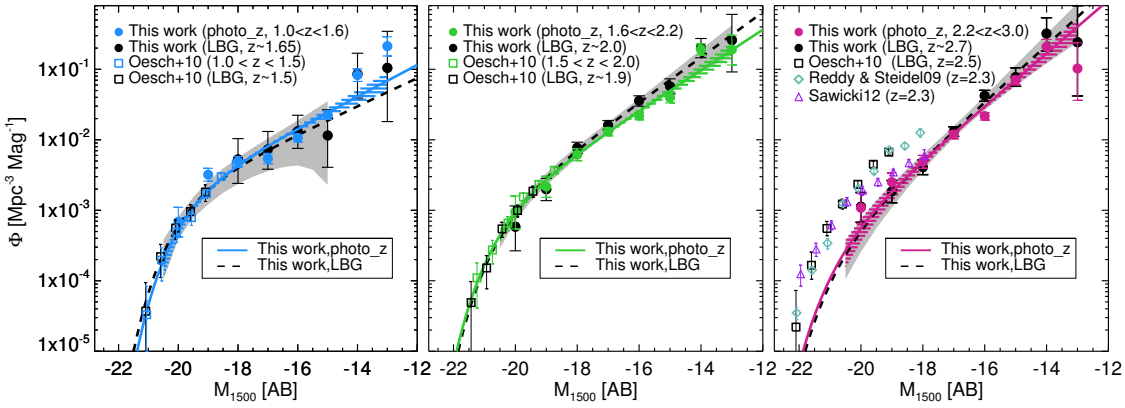

Figure 3.9: Comparing the UV LF of the LBG and photometric redshift samples. The black filled circles are the binned LBG LF for our F225W-, F275W- and F336W-dropout samples from left to right panels, respectively. The black dashed line in each panel represents the best-fit Schechter function for the corresponding LBG LF. The gray regions indicate the $\pm 2\sigma$ confidence region for each fit derived via Monte Carlo simulation. We over-plot the binned and best-fit LFs derived from our photometric redshift samples as shown before in Figure 3.7. The hatched region denotes the $\pm 2\sigma$ confidence region of the best-fit photometric redshift LF. The black open squares are the binned LBG LFs from Oesch et al. (2010a). The rest of the colors and symbols are as in Figure 3.7. For each redshift range, our binned and best-fit LFs are in consistent within the 2σ error bars.

3.10 Discussion

3.10.1 Comparing the UV LFs of Photometric redshift and LBG Samples

Figure 3.9 compares our LF results derived for the photometric redshift and UV-dropout selections. From left to right, the F225W-, F275W- and F336W-dropout LFs shown with black circles are compared with the photometric redshift LFs at $z \sim 1.3$ (blue circles), $z \sim 1.9$ (green circles) and $z \sim 2.6$ (red circles), respectively. Together with our data points for each redshift range, we also show the bright-end LFs of Oesch et al. (2010a) derived from their photometric redshift (blue, green and red squares) and UV-dropout (black squares) samples. In addition, we include the LF results from several relevant studies (Reddy and Steidel, 2009; Sawicki, 2012; Parsa et al., 2016). To compare these LF measurements, we run a set of Monte Carlo simulations and estimate the 2σ confidence interval from each best-fit Schechter function. The gray and hatched regions in Figure 3.9 encompass the 2σ uncertainties of the LBG and photometric redshift LFs, respectively. Because our LBG samples have fewer galaxies than the photometric redshift samples, the corresponding LFs are more uncertain. Our LFs are in agreement within these confidence regions. Indeed, similar agreement between LFs derived from these two selection techniques at higher redshifts has been shown before (McLure et al., 2013; Schenker et al., 2013). However, the lack of a robust knowledge of various systematic effects such as intrinsic size distribution and dust reddening at these faint luminosities still introduces moderate differences between these two LF measurements.

3.10.2 Evolution of the LF Schechter parameters

In order to understand the evolution of luminosity function parameters with redshift, we compare our best-fit Schechter parameters with other determinations of the rest-frame UV luminosity function at higher and lower redshifts in Figure 3.10. We summarize the evolution of LF parameters as below:

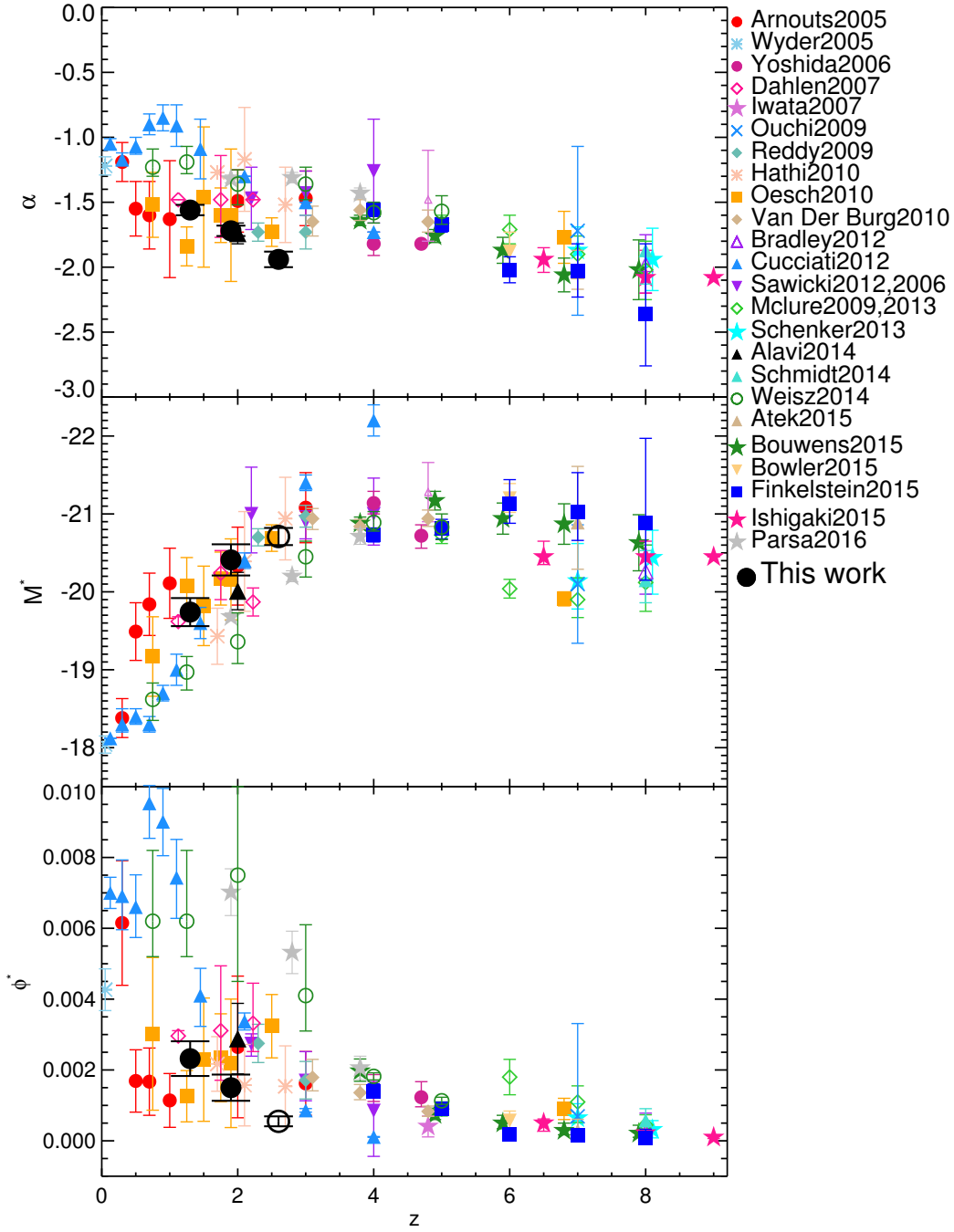

Figure 3.10: The redshift evolution of the Schechter parameters α(top), M^*(middle) and ϕ^*(bottom). The present determinations are shown with black filled circles. Our measurements of M^* and ϕ^* at $z \sim 2.6$ are shown with black open circles, as they are dependent on our choice of the M^* prior. All symbols from the literature are summarized in the right-hand side of the plot. A detailed description about each parameter evolution is given in the text (see Section 3.10.2).

Exploiting the magnification from strong gravitational lensing and consequently extending the UV LF to very low luminosities, enables a robust estimate of the faint-end slope. In the context of recent UV LF studies, there are not as many measurements at $z = 1 - 1.5$ to compare with our estimates, but as can be seen in Figure 3.10, our inferred value of the faint-end slope ($\alpha = -1.56 \pm 0.04$) at $z \sim 1.3$ is consistent with other results from Arnouts et al. (2005) and Oesch et al. (2010a) given their large uncertainties. We should note that we are in better agreement with the Oesch et al. (2010a) estimate for their LBG LF (at $z \sim 1.5$), as their photometric redshift LF has a very steep faint-end slope. Regarding our estimate for the $z \sim 1.9$ LF, we are again in good agreement with several other results, particularly both LBG and photometric redshift LFs of Oesch et al. (2010a) and also the $z = 2.3$ LF from Reddy and Steidel (2009). We note that we are also in agreement with our previous $z \sim 2$ LBG LF from A14 ($\alpha = -1.74 \pm 0.08$). Finally regarding our estimate for the $z \sim 2.6$ LF, we derive a faint-end slope steeper than previous determinations and more similar to the steep faint-end slopes favored at higher redshifts. As a consequence, we conclude a rapid evolution in the faint-end slope toward shallower values during the 2.2 Gyr from $z = 2.6$ to $z = 1.3$ which seems to continue to $z = 0$. We also refer the reader to a recent work by Parsa et al. (2016) (see gray filled stars in Figure 3.10) who study the UV LF between $z = 2-4$. For both $z = 1.9$ and $z = 2.8$, they derive a value of $\alpha = -1.32 \pm 0.04$ which is considerably shallower than most of the other studies including ours. Consequently, they derive fainter M^* and larger ϕ^* values relative to all of the other works at $z = 2 - 3$ in the literature. We note that they do not use the filter that samples the Lyman break at $z \sim 2$.

In addition to the observed LFs, we compare our results with the LFs from local group (LG) fossil records by Weisz et al. (2014) (open green circles in Figure 3.10). Using the SFHs of LG galaxies, they reconstruct the UV LFs down to very faint magnitudes of $M_{UV} \sim -1.5$. Comparing to our results, they estimate shallower faint-end slopes ($\alpha > -1.4$) for their $z = 1.25$ and 2.0 LFs, but they derive steeper faint-end slopes when they restrict their calculations to the luminosities where their data are complete. Although, for an exact

Table 3.4. UV Luminosity Density[a]

z	$M < -10$	$M < -17.475(0.04L^*_{z=3})$[b]	$-18.5 < M < -12.5$
$1.0 < z < 1.6$	$1.57^{+0.08}_{-0.08} \times 10^{26}$	$0.90^{+0.06}_{-0.06} \times 10^{26}$	$0.90^{+0.04}_{-0.05} \times 10^{26}$
$1.6 < z < 2.2$	$2.84^{+0.15}_{-0.15} \times 10^{26}$	$1.50^{+0.09}_{-0.09} \times 10^{26}$	$1.57^{+0.08}_{-0.10} \times 10^{26}$
$2.2 < z < 3.0$	$3.13^{+0.22}_{-0.24} \times 10^{26}$	$1.03^{+0.14}_{-0.19} \times 10^{26}$	$1.84^{+0.13}_{-0.15} \times 10^{26}$

[a]These values are in units of erg s^{-1} Hz^{-1} Mpc^{-3}.

[b]For $L^*_{z=3}$ we use the measurement from Reddy and Steidel (2009).

comparison, we need to consider the different uncertainties (i.e, small sample size) and systematic errors (i.e, uncertainty in the stellar models used for the SFHs) in their results, as well. This discrepancy between the faint-end slopes can be interpreted as a different evolution for the LG dwarfs relative to the field galaxies.

As seen in the middle panel of Figure 3.10, our characteristic UV magnitude, M^*, becomes brighter, $\Delta M^* = -0.7$, at $z = 1.9$ relative to $z = 1.3$. Also, our characteristic number density, ϕ^*, (lower panel of Figure 3.10) decreases by a factor of 1.5 over this time period. However, both of these measurements are dependent on data from other surveys, as our data only sample galaxies fainter than M^*.

3.10.3 UV Luminosity Density

We use our best LF determinations to derive the comoving UV luminosity density, ρ_{UV}, as below:

$$\rho_{UV} = \int_{L_{\rm faint}}^{\infty} L\phi(L)\mathrm{d}L = \int_{-\infty}^{M_{\rm faint}} L(M)\phi(M)\mathrm{d}M \tag{3.11}$$

where $\phi(L)(\phi(M))$ is the LF assuming a Schechter function. As an important consequence of the steep faint-end slope of the UV luminosity functions at $1 < z < 3$, the faint star-forming galaxies have a significant contribution to the total unobscured UV luminosity density at these redshifts. To quantify this, we calculate the cumulative UV luminosity density down to various UV luminosity limits. Figure 3.11 shows these results for our three redshift ranges.

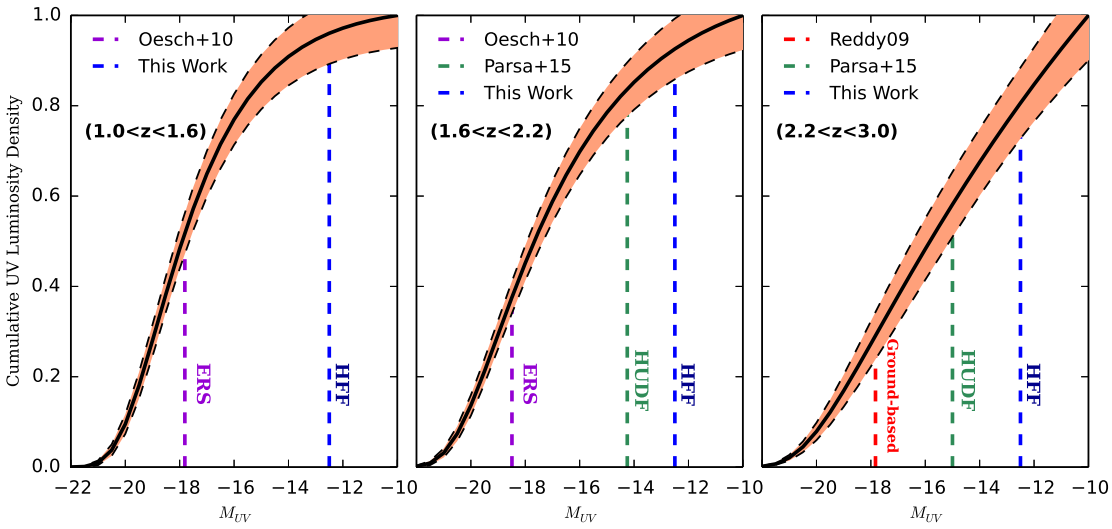

Figure 3.11: The cumulative UV luminosity density at $1.0 < z < 1.6$ (left), $1.6 < z < 2.2$ (middle) and $2.2 < z < 3.0$ (right). The purple, green and blue dashed lines show the UV limiting magnitudes for the ERS (Oesch et al., 2010a), Hubble Ultra Deep Field (Parsa et al., 2016) and our samples. The orange region represents the 1σ uncertainty measured at each M_{UV}. We have measured the LF of galaxies responsible for 58%, 55% and 59% of total UV luminosity density at $z \sim 1.3$, $z \sim 1.9$ and $z \sim 2.6$, respectively.

We note that all of these calculations are from our photometric redshift LFs, as they have smaller statistical uncertainties. We normalized our cumulative UV luminosity densities to the corresponding value at M_{UV}=-10 assuming that there is no turnover in the LF down to this absolute magnitude. To estimate the 1σ uncertainty at each M_{UV}, we run a Gibbs sampler (i.e., Markov Chain Monte Carlo sampling) to obtain a sequence of random pairs of (α,M^*) using their 2D joint probability function and then calculate the distribution of UV luminosity density and the corresponding uncertainty. We also incorporate the Poisson uncertainty in quadrature. These 1σ uncertainty regions are shaded orange in Figure 3.11. The unobscured UV luminosity density measurements are tabulated in Table 3.4. To be consistent with previous studies, we also provide the UV luminosity density values integrated down to $0.04L^*_{z=3}$.

The faint dwarf galaxies with UV magnitudes of $-18.5 < M_{1500} < -12.5$ covered in this work, comprise the majority of the unobscured UV luminosity density at the redshifts of peak star formation activity (58%, 55%, and 59% of the total UV luminosity density at $z \sim 1.3$, $z \sim 1.9$, and $z \sim 2.6$, respectively). Therefore, these dwarf galaxies may contribute significantly to the total *intrinsic* UV luminosity density and thus to the star formation rate density at these epochs. However, to quantify this, we need to incorporate the effect of dust reddening and its dependence on galaxy luminosity.

In order to understand the evolution of the UV luminosity density, we compare our ρ_{UV} measurements with other studies at various redshifts. As the value of ρ_{UV} depends on the limiting luminosity, i.e., L_{faint} in Equation 3.11, we use the published Schechter parameters from the literature and calculate the UV luminosity densities and corresponding uncertainties by integrating down to the same $M_{\rm faint} = -10$. We should note that there is no straightforward way to estimate the ρ_{UV} uncertainties as necessary information for these measurements such as covariance between Schechter parameters are not usually provided in the literature. But to assign uncertainty to each ρ_{UV} measurement in a consistent way, we use the same methodology as Madau and Dickinson (2014). We assume that the fractional error, i.e., $\Delta\rho_{UV}/\rho_{UV}$, provided by each author is fixed and thus derive the corresponding uncertainty for our ρ_{UV} value with $M_{faint} = -10$. Figure 3.12 illustrates these measurements. As seen in many previous studies (e.g., Cucciati et al., 2012), the unobscured (i.e, uncorrected for dust extinction) UV luminosity density rises from $z = 0$ to $z = 2.0$ where it reaches its peak and starts to decline after $z = 3$ (e.g., Oesch et al., 2010a; Finkelstein et al., 2015). As shown in Figure 3.12, our ρ_{UV} points (black filled circles) follow the similar trend as seen by previous determinations. However, our measurements show a more rapid evolution from $z = 1.3$ to $z = 1.9$ followed by a slower evolution up to $z = 2.6$.

We emphasize that the unobscured ρ_{UV} evolution rate and the exact location of the peak depends on the wavelength (Trenti et al., 2012) where ρ_{UV} is being measured, and the limiting luminosity, i.e., L_{faint} in Equation 3.11. Therefore, to find the best-fitting function describing the evolution of unobscured UV luminosity density between $z = 0 - 2.6$, we only

include the results from the literature at the same wavelength (1500Å) and integrated down to the same magnitude of $M_{UV} = -10$ through our own compilation. Fitting a power law, we find $\rho_{UV} = 25.58 \times (1+z)^{1.74}$ incorporating the data points from Schiminovich et al. (2005)(red filled circle); Dahlen et al. (2007) (pink open diamond); Oesch et al. (2010a) (for photometric redshift sample, orange filled square) and Cucciati et al. (2012) (blue filled triangle).

In addition, to study the evolution of ρ_{UV} for the whole redshift range from $z = 0$ to $z = 8$, we fit a function used by Madau and Dickinson (2014) as shown below. For the higher redshifts, we incorporate the data points from McLure et al. (2009, 2013)(green open diamond), Bouwens et al. (2015)(green filled star) and Parsa et al. (2016)(gray filled star), as well as the data points that we used for the power law.

$$\rho_{UV}(z) = a\frac{(1+z)^b}{1+[(1+z)/d]^c}\text{erg s}^{-1}\text{ Hz}^{-1}\text{ Mpc}^{-3} \tag{3.12}$$

where we derive $a = 0.34 \pm 0.04$, $b = 2.14 \pm 0.27$, $c = 3.41 \pm 0.23$ and $d = 3.86 \pm 0.63$. We emphasize that these best-fit values describe the ρ_{UV} evolution assuming a limiting magnitude of $M_{UV} = -10$, dramatically fainter than typical limits used in previous studies ($\sim$-17.5, Madau and Dickinson, 2014). Because we do not account for an increase in the uncertainty of ρ_{UV} at low luminosities, we add in quadrature 12% uncertainty to all of the data points to keep the reduced chi-squared equal to one.

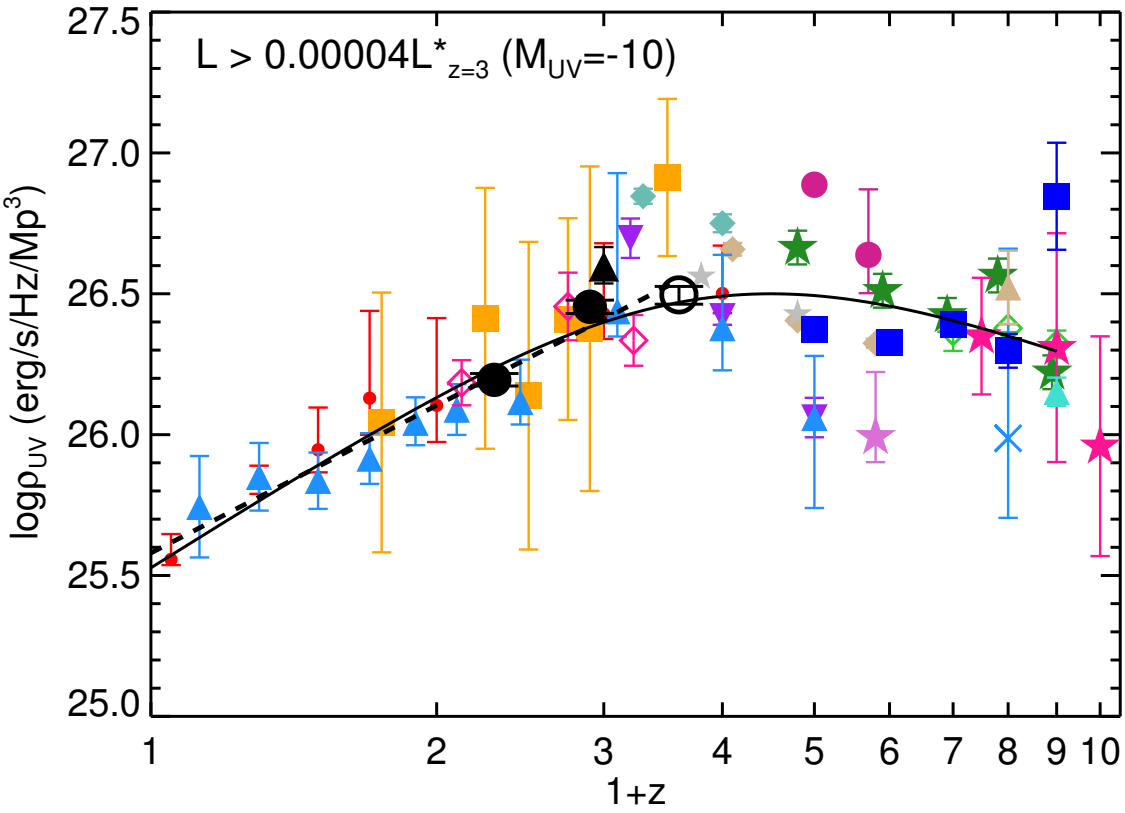

Figure 3.12: Redshift evolution of the unobscured UV luminosity density measured at rest-frame wavelength of 1500 Å . To estimate the ρ_{UV} values, the LFs are integrated down to $M_{UV} = -10$ at all redshifts. The uncertainty for each data point is derived by retaining the fractional error of published ρ_{UV} values from each author. The black filled circles are derived from our photometric redshift LF estimates. Similar to Figure 3.10, we show our ρ_{UV} measurement at $z = 2.6$ with a black open circle as it depends on the choice of M^* prior. The rest of the symbols are similar to Figure 3.10, except the red filled circles which are from Schiminovich et al. (2005) using the LF estimates from Arnouts et al. (2005); Wyder et al. (2005) (shown with red filled circle and blue asterisk in Figure 3.10, respectively). The dashed line indicates the best-fitting power law to the data points at $z < 2.6$. The solid line shows the best-fitting function (see Equation 3.12) for the redshift range of $0 < z < 8$.

3.10.4 No Turnover in the UV LF

Our observations have now reached the very faint luminosities where some simulations predict a turnover in the UV LF. Though our steep LFs extend down to $M_{UV} = -12.5$ and we showed that the faint bins with large completeness corrections are not affecting the faint-end slope fit (see 3.8.2), they may affect our interpretation of whether or not there is a turnover. As see in Figure 3.7, we can rule out the possibility of a turnover in the LF at magnitudes brighter than $M_{UV} < -14$, because one would need an unphysical large systematic effect to cause a turnover at this magnitude. This conclusion is in conflict with the results of recent cosmological hydrodynamical simulation by Kuhlen et al. (2013), who predict a turnover at $M_{UV} = -16$ in the $z \sim 2.5$ UV LF. Implementing an H_2-regulated star formation model, they predict that the star formation is suppressed in dwarf galaxies ($M_{UV} > -16$), because their gas surface density is below what is required to build a substantial molecular fraction. A similar tension between the observed UV LF and the turnover predicted by recent theoretical results has also been seen at higher redshifts (e.g., Jaacks et al., 2013; Livermore et al., 2016).

The presence of a turnover in the UV LF might also be used to constrain warm dark matter (WDM) models. Menci et al. (2016) provide a limit on the WDM particle mass by comparing the WDM halo mass function and the number density of ultra-faint galaxies derived from the UV LF in A14. The constraints can now be significantly improved given the much larger sample in this survey.

3.11 Summary

We have obtained deep near-UV imaging of three lensing clusters, two from the HFF surveys (A2744 and MACSJ0717) and A1689, to study the evolution of the UV LF during the peak epoch of cosmic star formation at $1 < z < 3$. Combining deep data with strong gravitational lensing magnification, we obtain a large sample (780) of ultra-faint galaxies with $M_{UV} < -12.5$ at $1 < z < 3$, using the photometric redshift selection. We perform

an extensive set of simulations to compute the completeness correction required for the LF measurements. We summarize our conclusions below:

- We derive the best Schechter fit to each UV LF using a maximum likelihood technique considering various sources of uncertainty including the lensing models. Thanks to the lensing magnification, we can extend the UV LF measurements down to very faint luminosities of $M_{UV} = -12.5$ at $1 < z < 3$. Consequently, we find a robust estimate of the UV LF faint-end slope to be $\alpha = -1.56 \pm 0.04$, $\alpha = -1.72 \pm 0.04$ and $\alpha = -1.94 \pm 0.06$ for $1.0 < z < 1.6$, $1.6 < z < 2.2$ and $2.2 < z < 3.0$, respectively. Our α measurements at $z \sim 1.3$ and $z \sim 1.9$ are consistent with previous studies of Reddy and Steidel (2009); Oesch et al. (2010a). But for $z \sim 2.3$, we have a steeper faint-end slope than previous studies. Our determinations of the UV LFs show a rapid evolution in the faint-end slope toward steeper values from $z = 1.3$ to $z = 2.6$. In addition, when we run a test to minimize the systematic effects by excluding galaxies and volumes $< 50\%$ completeness, we still derive steep faint-end slopes of $\alpha = -1.55 \pm 0.06$, -1.69 ± 0.07 and -1.79 ± 0.08 for $z \sim 1.3$, 1.9 and 2.6, respectively. However, for a better determination of the LF parameters, we need a better understanding of the size and color distribution of these faint galaxies.

- To understand the effect of different selection techniques on the UV LF, we use a two color “dropout" selection of Lyman break galaxies at redshifts similar to our photometric redshift samples. After correcting for incompleteness and then finding the best fit Schechter parameters, our LBG and photometric redshift LFs are in 2σ agreement.

- We integrate our UV LFs down to a magnitude limit of $M_{UV} = -10$ and find the UV luminosity density to be $\rho_{UV} = 1.57^{+0.08}_{-0.08} \times 10^{26}$, $2.84^{+0.15}_{-0.15} \times 10^{26}$ and $3.13^{+0.22}_{-0.24} \times 10^{26}$ erg s^{-1} Hz^{-1} Mpc^{-3} at $z \sim 1.3$, $z \sim 1.9$ and $z \sim 2.6$, respectively. We show that the faint star-forming galaxies with $-18.5 < M_{UV} < -12.5$, contribute the majority of the total unobscured UV luminosity density during the peak epoch of cosmic star formation.

- Though some models of warm dark matter and some prescriptions for H_2-regulated star-formation predict a turnover in the UV LF, we see no evidence for a turnover down to $M_{UV} = -14$ at $1 < z < 3$.

This study highlights the power of gravitational lensing to produce a robust constraint on the faint-end of the LF. However, as mentioned in Section 3.10.1, this analysis still suffers from uncertainties that are systematic, rather than statistical. To overcome these uncertainties, in the future, we require precise measurements of size distribution and dust reddening at low luminosities.

We thank the referee for a careful reading and useful comments that improved this paper. The authors are grateful to the STScI and HFF team for obtaining and reducing the *HST* images. A.A. would like to thank Pascal Oesch for providing their individual measurements for photometric redshift LFs, Takatoshi Shibuya for sending size measurements, Jose Diego for providing us a list of A1689 multiple images, as well as John Blakeslee and Karla Kalamo for providing us a list of globular clusters of A1698. A.A. also thanks Daniel Weisz for his valuable comments as well as Naveen Reddy, Nader Shakibay Senobari, Mario De Leo, Ali Ahmad Khostovan and Kaveh Vasei for useful conversations. MJ acknowledges support from the Science and Technology Facilities Council [grant number ST/L00075X/1 & ST/F001166/1]. ML acknowledges the Centre National de la Recherche Scientifique (CNRS) for its support. This work is based on observations with the NASA/ESA Hubble Space Telescope, obtained at the Space Telescope Science Institute, which is operated by the Association of Universities for Research in Astronomy, Inc., under NASA contract NAS 5-26555.

Appendix

A1 Lyman break Selection

In this section, we outline our selection criteria to find Lyman break galaxies (Steidel et al., 1999). We adopted a standard color-color diagram to sample the UV continuum break in the SED of high redshift galaxies. As shown in Figure 3.13, the selection region is defined based on the location of tracks of star forming galaxies in the color-color plot. The star-forming tracks are predictions from (Bruzual and Charlot, 2003) synthetic stellar population models assuming a constant star formation history, 0.2 $Z_{\odot}$ and an age of 100 Myr with different color excess of E(B-V)=[0,0.1,0.2,0.3]. In the next subsection, we summarize the selection criteria we use to identify the z $\sim 1-3$ galaxies. As A1689 is observed with different sets of filters than the HFFs, it is not possible to use the same color criteria for all of these fields. Therefore, we construct analogous selection criteria as below.

For F225W dropout sources, considering that A1689 is the only field where F225W images are available, the selection criteria are as below,

$$F225W - F275W > 0.75$$

$$F275W - F336W < 1.4$$

$$F225W - F275W > 1.67(F275W - F336W) - 0.42$$

$$S/N(F275W) > 5 \quad , \quad S/N(F336W) > 5 \tag{3.13}$$

These color criteria, which are identical to Oesch et al. (2010a) find 31 galaxy candidates in A1689.

For F275W dropout sources, the selection criteria for A1689 with F625W-band imaging are

$$F275W - F336W > 1$$

$$F336W - F625W < 1.3$$

$$F275W - F336W > 2.67(F336W - F625W) - 1.67$$

$$S/N(F336W) > 5 \quad , \quad S/N(F625W) > 5$$

(3.14)

These color criteria, which are identical to what we used before in A14 find 99 galaxy candidates in A1689. For F275W dropout sources, the selection criteria for HFFs where F606W-band imaging are available instead of F625W-band data, we use identical selection criteria as for A1689. In total, these color criteria find 230 galaxy candidate over three clusters. 99 of these candidates are from A1689 in comparison with 84 candidates in A14, because we added 14 orbits to the 4 orbits of F336W image that we used in A14.

For F336W dropout sources, the selection criteria for HFFs are

$$F336W - F435W > 1$$

$$F435W - 814W < 1.2$$

$$F336W - F435W > 2.4(F435W - F814W) - 0.68$$

$$S/N(F435W) > 5 \quad , \quad S/N(F814W) > 5$$

(3.15)

These criteria find 189 galaxy candidates over HFFs. Similar to our $z \sim 2.6$ photometric redshift sample (see Section 3.6), we do not include A1689 in our F336W-dropout sample as there is contamination from cluster members. As discussed in Section 3.6, we remove all of the multiple images corresponding to a single source except the brightest image. We then use the same identification scheme as our photometric redshift samples to remove contamination from stars, stellar spikes and spurious detections from low-redshift bright galaxies. As seen in Figure 3.13, the stellar sequence (orange asterisks) enters the selection region of F225W- and F336W-dropouts, resulting a contamination of 3.2% and 1.6% of stars, respectively. We also excluded a low contamination of 1.3% and 4.2% from the stellar spikes and spurious objects in the F275W- and F336W-dropouts, respectively.

In addition, our photometric redshift measurements show that the fraction of low-redshift interlopers in the LBG samples are low. We find that only 9.7%, 7.8% and 5.8% of our F225W-, F275W- and F336W-dropout samples are low-redshift interloper with $z < 1.0$, $z < 1.3$ and $z < 1.5$, respectively. As illustrated in Figure 3.14 and explained in next section, we derive these redshift cuts using the expected redshift distribution from our completeness simulations for dropout samples.

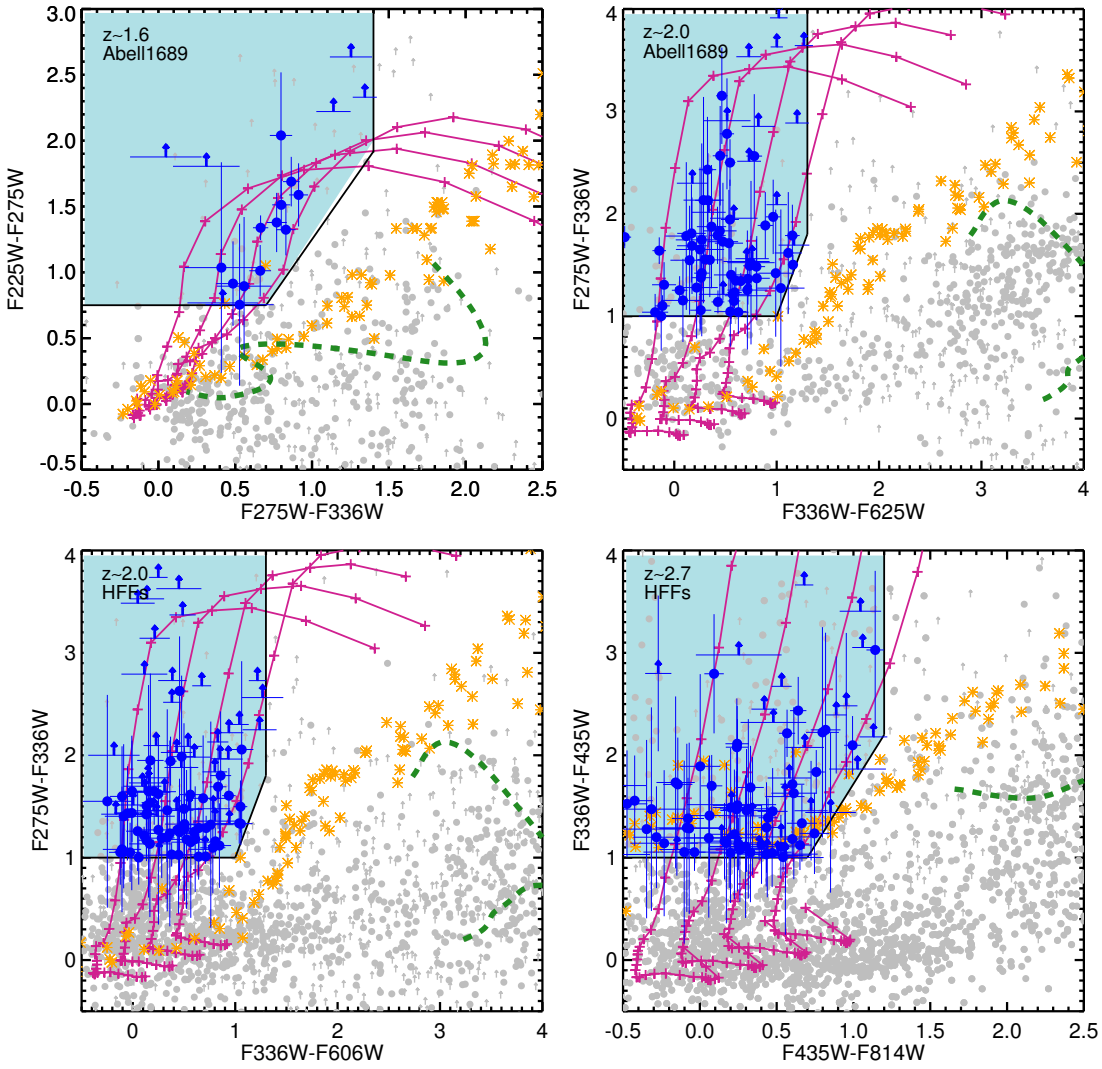

Figure 3.13: Color-color selection of Lyman break galaxies for F225W- (left), F275W- (middle) and F336W-dropouts (right). A1689 and HFF LBG selections are shown separately in the upper and lower panels, respectively. Gray circles are all of the objects in the corresponding catalogs. The orange asterisks are stars from Pickles (1998). The green dashed line shows the color track of low redshift ($0 < z < 1$) elliptical galaxies from Coleman et al. (1980). The violet lines are star-forming tracks with different dust reddening values of E(B-V)=[0,0.1,0.2,0.3]. The blue region shows the selection criteria. The blue symbols are the LBG candidates with 5σ detection in two bands redward of Lyman limit (see text). The blue arrows represent 1σ lower limits.

A2 Completeness Simulation for LBG LF

Following the analysis for our photometric redshift sample, we run the same Monte Carlo simulation to assess the completeness values, C(m, z, $\mu_{\rm mag}$), for the Lyman break samples. As described in details in Section 3.7, after generating the random artificial galaxies with similar properties as observed sources, we require the same selection criteria (Equations A1 to A3) as we used for the observed LBGs. Figure 3.14 illustrates the completeness distribution for two intrinsic apparent magnitudes (i.e., before magnification) of $m_{UV} = 27, 28$ and magnification $\mu_{\rm mag} = 1.0$ mag. To compare with the observed galaxies, we over-plot the photometric redshift distribution of the whole catalog together with the subsample selected as LBG. As seen in this figure, the redshift distribution of LBGs (blue histograms) relative to the redshift distribution of all galaxies in the field (grey histograms) are consistent with the completeness calculations.

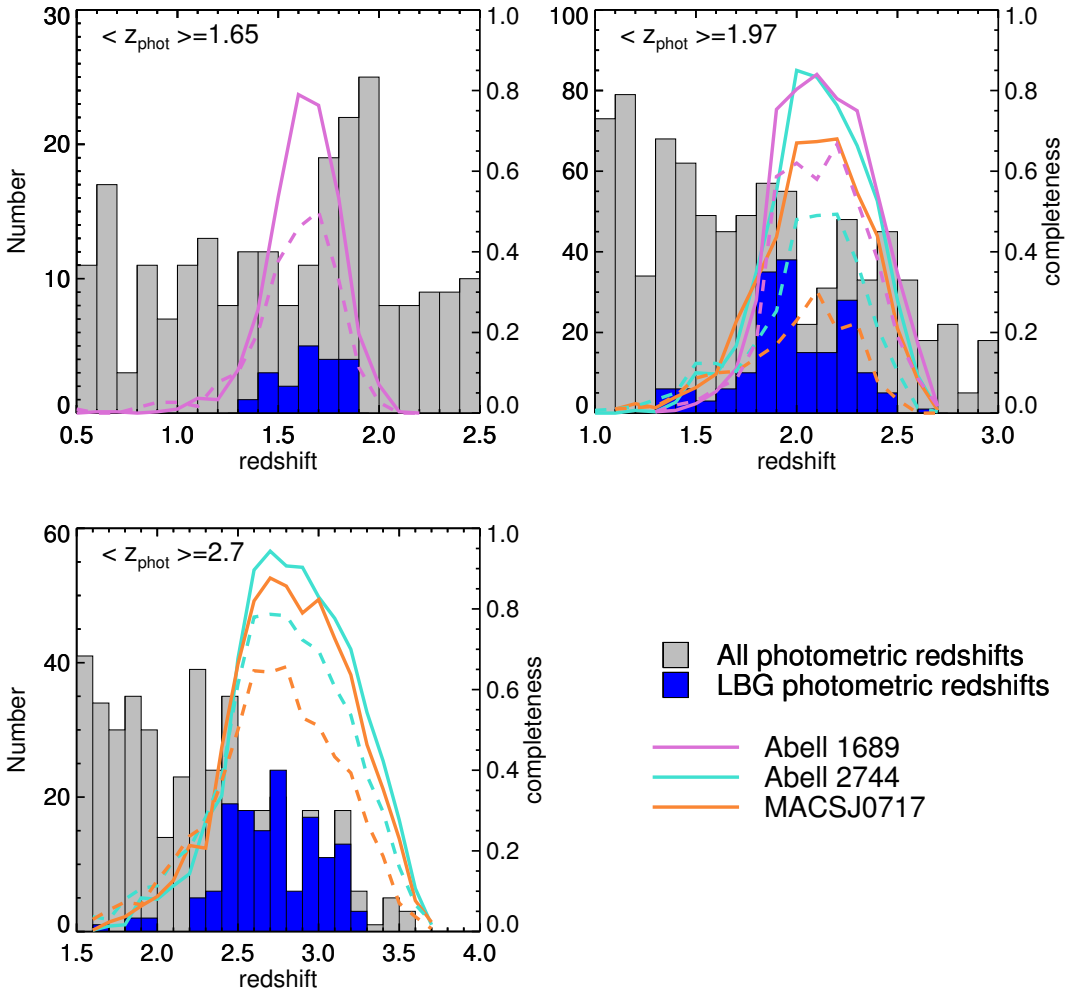

Figure 3.14: Photometric redshift distribution of LBGs. The gray histogram shows the photometric redshift distribution of all objects in the fields. The blue histogram highlights the photometric redshift distribution of those galaxies selected as LBG. The solid and dashed lines show the simulated completeness distribution over redshift for a galaxy with $\mu_{\rm mag} = 1.0$ and $m_{UV} = 27$ and 28, respectively. The purple, blue and orange colors present the completeness distribution for A1689, A2744 and MACSJ0717, respectively. The right-hand axis shows the completeness values.

A3 New Multiply Imaged Systems

As described in Section 3.5.3, we identify 5 new multiply lensed system candidates in A1689. Table 3.5 summarizes these systems where we provide their photometric redshift estimates and color measurements, as well. Because one of the primary indicators of multiple images is their uniform colors (i.e., magnification is independent of wavelength), we show their RGB composite image (see Figure 3.15) combining F814W, F625W and F475W data as red, green and blue filters. In Figure 3.16, we show the positions of all 5 new systems on a color-composite image of A1689. We also overplot the critical lines at $z = 2.5$. The RGB colors are similar to Figure 3.15.

Table 3.5. New Multiply Imaged Systems in A1689

system	R.A.(J2000)	Dec(J2000)	z_{phot}	Δz_{phot}	F336W-F475W	F475W-F625W	F625W-F775W	F775W-F814W
a.1	197.875427	-1.353059	2.33	0.13	0.72±0.12	-0.19±0.12	-0.05±0.15	-0.01±0.12
a.2	197.886612	-1.344707	1.90	0.07	0.30±0.09	-0.09±0.10	-0.08±0.12	0.03±0.10
a.3	197.858505	-1.337834	2.33	0.10	0.67±0.11	-0.11±0.11	-0.12±0.13	-0.02±0.11
a.4	197.880814	-1.335316	2.20	0.17	0.65±0.15	-0.08±0.14	-0.01±0.17	-0.13±0.14
b.1	197.886612	-1.352190	1.87	0.27	0.48±0.29	-0.21±0.33	-0.06±0.41	-0.08±0.33
b.2	197.873810	-1.333846	2.02	0.10	-0.03±0.18	-0.36±0.28	0.06±0.34	-0.13±0.27
c.1	197.875732	-1.350983	2.47	0.10	1.56±0.22	0.07±0.11	0.02±0.12	-0.07±0.10
c.2	197.858337	-1.333123	2.40	0.06	1.30±0.17	0.23±0.10	0.17±0.10	-0.21±0.08
d.1	197.879654	-1.342635	2.61	0.10	1.92±0.30	0.01±0.12	-0.16±0.14	0.01±0.12
d.2	197.878067	-1.342786	2.57	0.19	2.08±0.54	0.02±0.17	-0.02±0.19	0.15±0.15
d.3	197.855209	-1.339240	2.30	0.09	0.62±0.12	0.11±0.11	-0.04±0.12	-0.19±0.10
e.1	197.877899	-1.354296	3.19	0.19	>3.32	0.67±0.09	0.10±0.08	-0.07±0.07
e.2	197.885437	-1.349361	3.23	0.18	>3.65	0.64±0.08	0.05±0.07	0.05±0.06
e.3	197.879929	-1.335399	3.11	0.26	>2.39	0.76±0.17	0.13±0.13	0.04±0.10
e.4	197.857147	-1.340662	3.32	0.23	>2.86 -	0.89±0.13	0.02±0.10	0.08±0.08

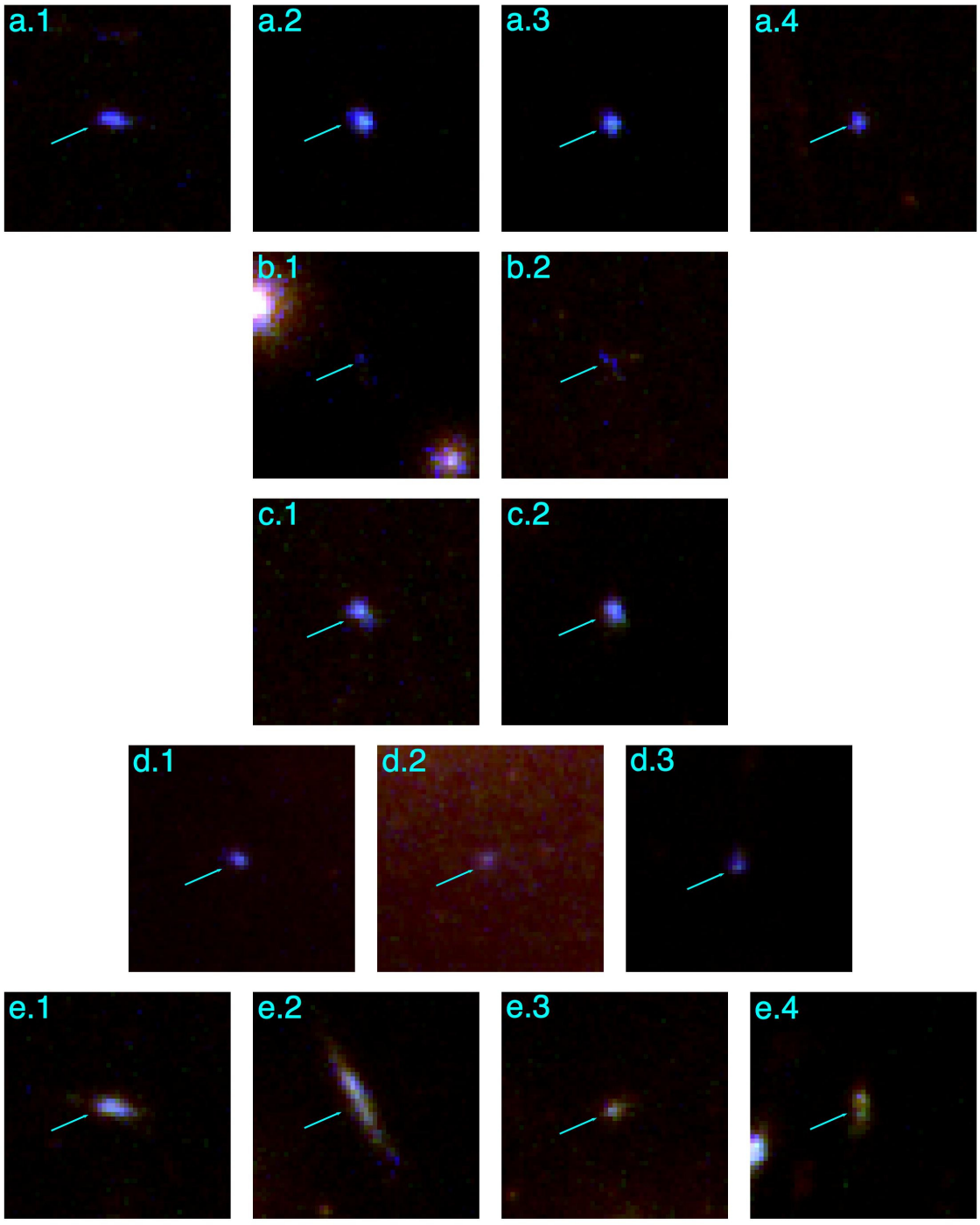

Figure 3.15: Newly-identified multiply imaged systems in A1689. The arrow in each stamp denotes the position of each multiple image. The color image is a combination of F475W(blue), F625W(green) and F814W(red) filters. We note that the reddening in d.2 image is due to a nearby cluster member. The size of each cutout is 2″.

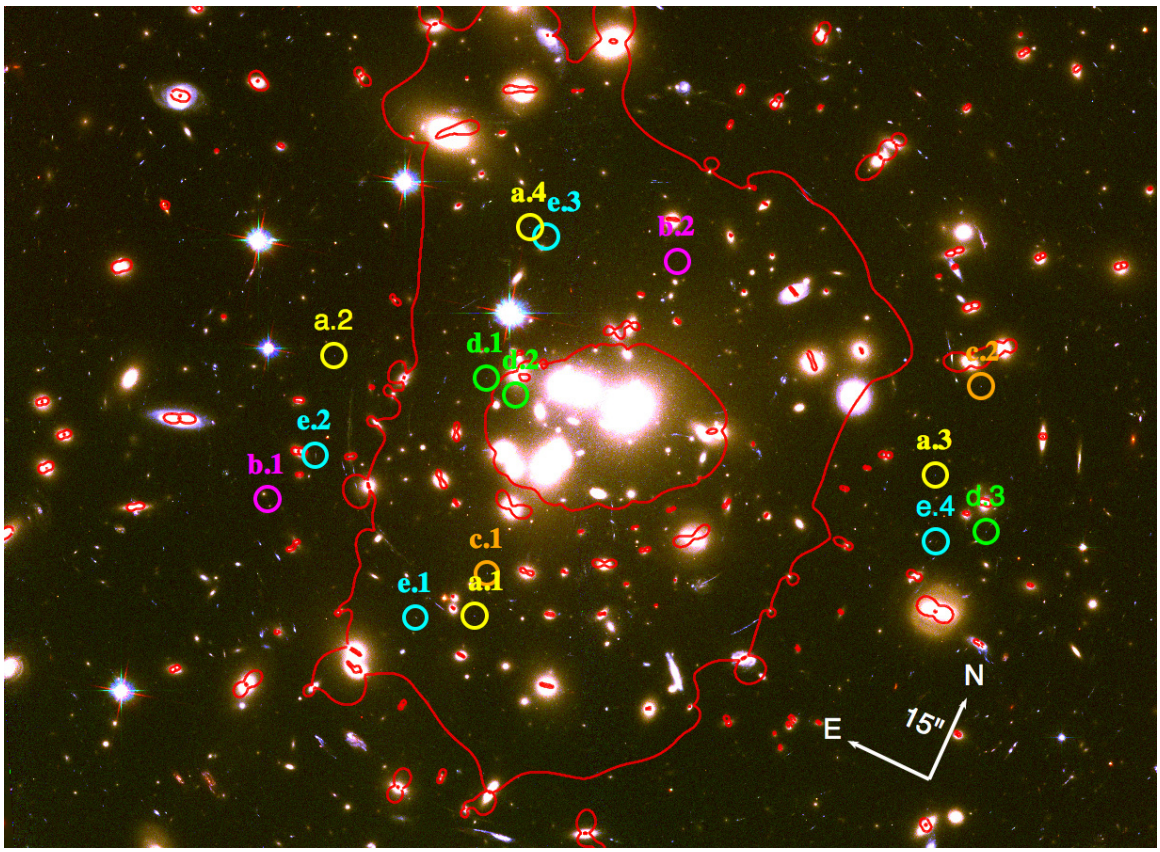

Figure 3.16: The color image is a composite of F475W(blue), F625W(green) and F814W(red) filters. The contours show the critical lines for sources at z=2.5. The circles denote the positions of the newly found multiple images. A compass provides the orientation and the lengths of the arrows show the 15″ scale. Some of the labels have been offset slightly.

Chapter 4

The UV Continuum Slopes of Faint Lensed Star-forming Galaxies

Abstract

We study the evolution of rest-frame ultraviolet colors of very faint galaxies in the epoch of peak star formation at $1 < z < 3$. We measure the UV continuum slopes β for 766 faint galaxies down to an absolute magnitude of $M_{UV} < -12.5$. These galaxies are magnified by strong gravitational lensing from three foreground galaxy clusters, with two from the Hubble Frontier Fields program. We adopt two different methods to measure the UV continuum slopes via either fitting a power-law function to the broad-band photometry or fitting the spectral energy distribution of each object with the best synthetic stellar population models and then measuring the UV spectral slope from the best-fit model. Our final findings are robust against the choice of method. We find a correlation between β and UV absolute magnitude with $-20 < M_{UV} < -12.5$, with slopes of $d\beta/dM_{UV} = -0.07\pm0.02$, -0.12 ± 0.03 and -0.14 ± 0.02 at $1.0 < z < 1.6$, $1.6 < z < 2.2$ and $2.2 < z < 3.0$, respectively. Therefore, at these low luminosity ranges, the galaxies become bluer at fainter M_{UV} magnitudes. For the first time at these low luminosities, we provide robust measurements for intrinsic scatter around $\beta - M_{UV}$ and we find no significant evidence for a changing intrinsic scatter with

luminosity. We find that the median β values of galaxies evolve with redshift and becomes bluer at higher redshifts. However, this evolution is stronger for our fainter magnitude bin of $M_{UV} = -13.75$ with $d\beta/dz = -0.18 \pm 0.12$ than our brighter magnitude bin of $M_{UV} = -17.75$ with $d\beta/dz = -0.06 \pm 0.02$. Finally, we look for a physical interpretation for the large intrinsic scatter in the $\beta - M_{UV}$ relation at faint luminosities. Using a sample of 11 low-stellar mass galaxies (i.e., comparable to our faint galaxies) from hydro-dynamical simulations with bursty star formation history (SFH), we find that the bursty SFHs can generate a large scatter in the β distributions of faint galaxies with $M_{UV} > -16$.

4.1 Introduction

The ultraviolet (UV) light, which is largely emitted by young stars, provides a powerful tool to characterize the build up of galaxies at different redshifts. In particular, the UV continuum color (i.e., UV continuum slope) of galaxies, which is dependent on various galaxy quantities such as dust extinction, metallicty, age and star formation history (SFH), can be used to probe the evolution of galaxies. However, because the first three quantities affect the UV color in the same way such that it becomes redder if they increase, it is challenging to distinguish one parameter from the others.

Over the past two decades, many studies have measured the distribution of UV continuum slopes of galaxies from the local to the very high-redshift universe. Among these studies, many have tried to determine whether the UV color and UV luminosity are correlated both at $z < 3$ (Adelberger and Steidel, 2000; Bouwens et al., 2009; Heinis et al., 2013; Kurczynski et al., 2014; Hathi et al., 2016) and $z > 3$ (Ouchi et al., 2004; Overzier et al., 2008; Bouwens et al., 2009; Lee et al., 2011; Wilkins et al., 2011; Bouwens et al., 2012b; Castellano et al., 2012; Dunlop et al., 2012; Finkelstein et al., 2012; Dunlop et al., 2013; Rogers et al., 2013; Bouwens et al., 2014). Broadly, most of these studies have found a significant correlation between UV color and UV luminosity such that the bright galaxies at a given redshift seem to be redder than faint galaxies. However, some of these studies do not see this correlation (Dunlop et al., 2013), but rather they report a relation between UV continuum slope and stellar masses (Hathi et al., 2016; Finkelstein et al., 2012). In addition, comparing the UV slope measurements at different redshifts, it is found that high-redshift galaxies tend to be bluer than low-redshift galaxies. These two trends of changing UV continuum slopes with luminosity and redshift, have been explained as a result of different amount of dust extinction, with a lower value for higher redshifts and fainter galaxies. As discussed in different studies (e.g., Bouwens et al., 2012b; Finkelstein et al., 2012), the change in the other galaxy quantities such as stellar age and metallicity can not generate the observed evolution in the UV continuum slope .

The aforementioned correlation between the UV continuum color and luminosity is often parametrized as a linear relationship with some scatter. The slope of this relation tells us about how dust extinction, metallicity and age changes with luminosity. However, the scatter is mainly due to different dust extinction and stellar populations (i.e., star formation history) in individual galaxies (Bouwens et al., 2012b).

The cosmic star formation density peaks at some time between $1 < z < 3$. Therefore, this epoch is an important time in galaxy formation and evolution. Since Meurer et al. (1999) examined the UV continuum slope of galaxies at $z = 3$, many studies have been allocated to UV color measurements at $1 < z < 3$. Specifically, some of these studies have examined the UV slope-luminosity relation and its evolution with redshift (Bouwens et al., 2009; Heinis et al., 2013; Kurczynski et al., 2014; Hathi et al., 2016). Bouwens et al. (2009) found a strong UV slope-magnitude relation at z=2.5 for galaxies with $M_{UV} < -18.5$. However, later, both Heinis et al. (2013) and Hathi et al. (2016) found that the average UV slope is independent of UV luminosity for $M_{UV} < -18.5$ and -18.0 at z=1.5 and $2.0 < z < 2.5$, respectively. While these studies are limited to only bright galaxies, Kurczynski et al. (2014) recently used deep UV data from the Hubble Ultradeep Field (UVUDF, Teplitz et al. (2013)) and extended the UV color measurements down to $M_{UV} = -14$ and -15.5 at $1 < z < 2$ and $2 < z < 3$, respectively. Broadly consistent with the literature, they also found that the UV continuum slope is bluer for fainter galaxies, and higher redshifts. In this regard, in Alavi et al. (2014, hereafter A14), we used a very deep UV imaging of a galaxy cluster (Abell 1689) to measure the UV properties of a sample of ultra-faint galaxies with magnitudes down to $M_{UV} = -13$ at $z \sim 2$. Our findings for the UV continuum color of these faint galaxies were consistent with the general trend where the fainter galaxies have more negative UV colors and thus they are bluer.

Although good progress has been made in establishing the UV continuum slope distribution of faint galaxies during the peak epoch, it is clear that a comprehensive and consistent determination of these distributions and their evolutions is still needed. The main goal of this manuscript is to provide these analyses. To this end, we take advantage of mag-

nification due to strong gravitational lensing from foreground galaxy clusters to push the detection limits of current surveys to much fainter luminosities. We applied a similar technique in A14, where we targeted the galaxies behind a lensing cluster A1689 and thus we were able to identify a sample of very faint galaxies (i.e., up to 100× fainter than previous determinations).

The Hubble Frontier Fields (hereafter HFFs) program, which targets 6 lensing galaxy clusters, has a great potential to map out the faint galaxies. In the present paper, we use deep WFC3/UVIS data of two clusters from the HFFs as well as our previous deep UV imaging of the A1689 cluster to compile a large sample of very faint galaxies at $1 < z < 3$ and thus provide a robust estimate of UV continuum slope and its evolution during this important era in cosmic history. The plan for this paper is as follows. In Section 4.2, we provide a brief summary of our observations and sample selection. In Section 4.3, we describe and compare two methodologies that we have adopted to measure the UV continuum color. We apply a maximum likelihood approach to investigate the relation between UV continuum slope and UV magnitudes, in Section 4.4. In Section 4.5, we provide a comparison with previous determinations at various redshifts and we study the evolution of UV color distribution with redshift in Section 4.6. Finally in Section 4.7, we discuss the implication of such UV color distribution for star formation histories of faint galaxies. In this section we present a comparison with hydro-dynamical simulations of low-mass galaxies comparable with our observed lensed faint samples.

In this paper, all magnitudes are quoted in the AB system (Oke and Gunn, 1983). For the cosmological parameters, we adopt $\Omega = 0.3_M$, $\Omega_\Lambda = 0.7$ and H_0=70 km s^{-1} Mpc^{-1}.

4.2 Data and Sample Selection

In this paper, we use the data, photometric catalogs and the samples from our recent work Alavi et al. (2016, hereafter A16). Here, we provide a short summary of our data and sample selection criteria. We utilize the deep multi-band data of three lensing clusters, Abell 2744

(hereafter A2744), MACSJ0717 (hereafter M0717) and Abell 1689 (hereafter A1689). The first two clusters, which are from the HFFs program, are observed in 9 *HST* bands of F275W, F336W, F435W, F606W, F814W, F105W, F125W, F140W and F160W. The last cluster is observed in 8 *HST* bands of F225W, F275W, F336W, F475W, F625W, F775W, F814W and F850LP. A complete description of data reduction and photometry are given in A14 and A16.

Using these photometric catalogs, we run the `EAZY` code (Brammer et al., 2008) to estimate photometric redshifts for objects in each of our three lensing fields. We construct three galaxy samples at $z \sim 1.3$ ($1.0 < z < 1.6$), $z \sim 1.9$ ($1.6 < z < 2.2$) and $z \sim 2.6$ ($2.2 < z < 3.0$) using the photometric redshifts. Our selection criteria require 3σ detection in all of the filters redward of the Lyman break, which will eventually be used for the UV spectral slope measurements (see Section 4.3). This criterion is slightly different than what we had in A16 where we required 3σ detection in only the detection filter (i.e., the filter immediately redward of the Lyman break) and the rest-frame 1500 Å filter. Our final samples comprise 269, 251 and 246 galaxies at $z = 1.3$, $z = 1.9$ and $z = 2.2$, respectively. We note that the magnification due to strong gravitational lensing from these galaxy clusters enables us to probe very faint luminosities, such that our samples extend down to intrinsic UV magnitude of $M_{UV} = -12.5$.

4.3 UV Spectral Slope

The rest-frame UV continuum spectra of galaxies can be parametrized by a power-law function as $f_\lambda \propto \lambda^\beta$, where f_λ is the flux density per wavelength and β is the UV continuum slope (Calzetti et al., 1994). As defined in Calzetti et al. (1994), we adopt the wavelength range of $\lambda = 1250 - 2600$ Å for our UV slope measurements. This parametrization was originally presented for the UV continuum spectroscopy of galaxies, but the β values of high-redshift galaxies are often measured from the broad-band photometry, because of the lack of rest-frame UV spectroscopic data. In this section, we describe two methodologies

and explore their relative merit for measuring the UV spectral slopes of our lensed galaxies at $1 < z < 3$.

4.3.1 Power Law Fitting

In this technique, which has been used in several other studies (e.g., Bouwens et al., 2009; Finkelstein et al., 2012; Rogers et al., 2013), we use the photometric redshift of each galaxy to choose the broad-band filters between rest-frame $\lambda = 1250 - 2600$ Å. We then fit a power law to the selected broad-band photometry. To this end, a broad-band filter is considered if the mean wavelength[1] of the corresponding filter is within this wavelength range. In addition, to avoid contamination from the Lyα emission line, we exclude a filter whose transmission at the redshifted Lyα wavelength is above 50% of its maximum transmission. As a consequence, at each redshift, only a specific group of filters satisfy all of these criteria.

In this method, we build a grid of power-law SEDs with different β values assuming the photometric redshift of each object. We then calculate the synthetic photometry via multiplying each SED with the transmission curves of corresponding group of filters (i.e., chosen from the above criteria). Comparing the synthetic and the observed colors for each galaxy, we yield a grid of $\chi^2(\beta)$, which is then minimized to derive the best β value and the corresponding uncertainty.

An advantage of this technique is that it directly uses the observed colors without any assumption about the intrinsic physical properties (i.e., SFH, IMF, metallicity) of galaxies. However, due to the limited number of passbands, most of our β values are from only single color measurements and they therefore have large uncertainties. Throughout the rest of the paper, we will refer to these measurements as $\beta_{\rm power}$.

4.3.2 SED Fitting

To make full use of available photometry, 0.27-1.54 μm for HFFs and 0.24-0.91 μm for A1689, we measure β via fitting to the best spectral energy distribution (SED) of each

[1] The mean wavelength is defined as $\lambda_{mean} = \int \lambda T_\lambda d\lambda \,/\, \int T_\lambda d\lambda$

galaxy (Finkelstein et al., 2012; Rogers et al., 2013). To this end, we use the code Fitting and Assessment of Synthetic Templates (`FAST`, Kriek et al., 2009) to perform the SED fitting of multi-band photometry. FAST uses the Bruzual and Charlot (hereafter BC03 2003) synthetic stellar population models and determines the best-fit SED via a χ^2 fitting. For the input parameters to `FAST`, we assume a Chabrier (2003) IMF, an age of 10 Myr up to the age of the universe at that redshift, a metallicity range of [0.2 $Z_\odot$, 0.4 $Z_\odot$] and a dust extinction of $0 < A_v < 3$. As justified in Reddy et al. (2012) for high-redshift galaxies at $z > 2$, we assume an exponentially-increasing star formation history (i.e., SFH $\propto e^{t/\tau}$) with $8 < \log(\tau) < 11$. We fix the redshifts to the output photometric redshifts from `EAZY`, as these two codes are compatible.

To avoid the effect of absorption and emission features, Calzetti et al. (1994) suggested 10 spectral windows between 1250-2600 Å to be used for β measurements. Using the best-fit SED of each object, we calculate the mean wavelength and flux within these windows and then find the β via a linear fit to $\log(f_\lambda)$ versus $\log(\lambda)$. We estimate the β uncertainties by running a series of Monte Carlo simulations where the observed fluxes are randomly modified according to their uncertainties, re-running `FAST`, re-fitting the β values and calculating the 68% confidence interval. Throughout the rest of the paper, we will refer to these measurements as $\beta_{\rm SED}$.

An advantage of the SED-fitting method is that it uses more colors to compute the $\beta_{\rm SED}$ values. However, the disadvantage is that the $\beta_{\rm SED}$ measurements are limited to the allowable values from the stellar population models, that have been used for the SED fitting. In particular, the bluest UV spectral slope value among our models is -2.91 and therefore the $\beta_{\rm SED}$ value for an observed galaxy with bluer UV continuum will not be estimated accurately.

4.3.3 Comparing the Methods

As shown in the upper panel of Figure 4.1 , the two β measurements generally agree, with median $|\Delta\beta| < 0.1$ for all of the three redshift ranges. This is expected as the SED

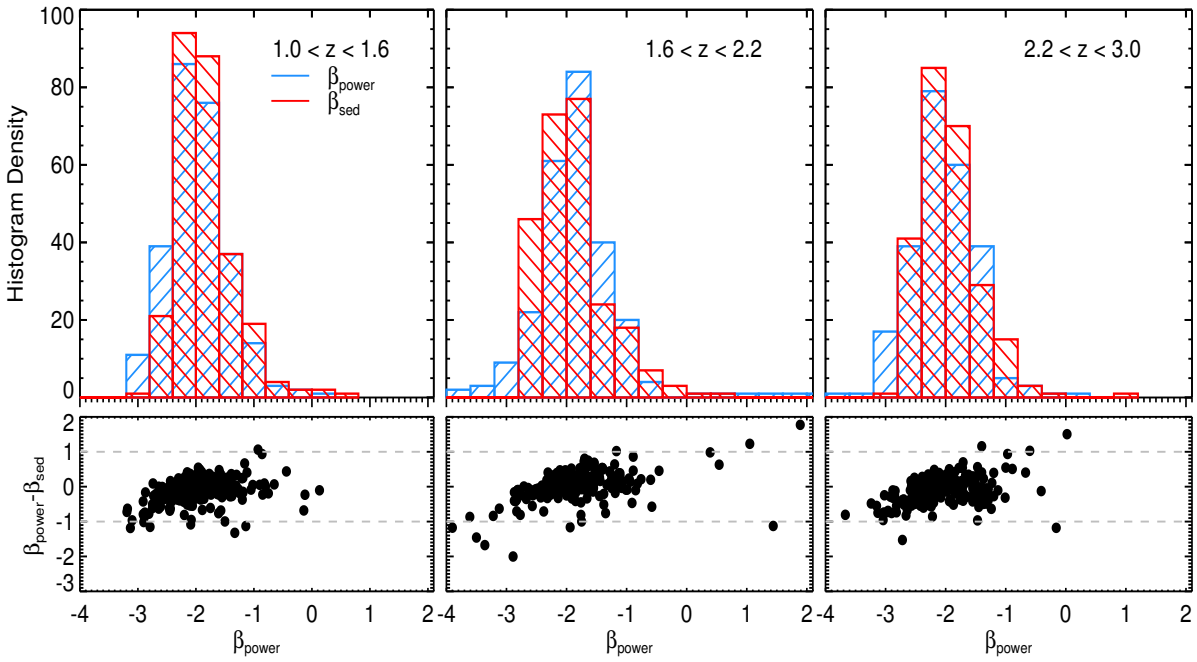

Figure 4.1: Comparing the $\beta_{\rm power}$ and $\beta_{\rm SED}$ values. Upper row: The distribution of $\beta_{\rm power}$ and $\beta_{\rm SED}$ values are shown with the blue and red histograms, respectively. As seen here, while the two distributions agree well in general, the $\beta_{\rm power}$ estimates extend to bluer values (i.e, $\beta_{\rm power} < -2.91$) than the $\beta_{\rm SED}$ measurements. Lower row: The difference between the $\beta_{\rm power}$ and $\beta_{\rm SED}$ measurements versus the $\beta_{\rm power}$ values on the x-axis. The gray dashed lines define the region beyond which we identify the outliers to be excluded from our samples.

fitting is performed on the same broad-band photometries that are used for the power-law measurements. However, as explained above, at very blue $\beta_{\rm power}$ values, the difference becomes larger where the stellar population models can not recover as blue $\beta_{\rm SED}$ values.

The lower panel of Figure 4.1 shows the difference between the $\beta_{\rm power}$ and $\beta_{\rm SED}$ measurements. We identify 7 (2.6%), 10 (4.0%) and 5 (2.0%) outliers, defined to have $|\Delta\beta| = |\beta_{\rm power} - \beta_{\rm SED}| > 1$, from the $z = 1.3$, $z = 1.9$ and $z = 2.6$ samples. For half of these outliers, the measurements are uncertain and a 2175 Å bump is likely affecting one of the filters and thus it results in a deviation from a power-law approximation. The other half of these outliers consists of very red galaxies whose $\beta_{\rm power}$ values are measured from a single color and are thus uncertain.

4.4 Dependence of β on UV Magnitude

We study the distribution of UV continuum slopes over a wide range of UV absolute magnitudes. Similar to the analysis in A16, we measure the UV absolute magnitude ($M_{UV} = M_{1500}$) at rest-frame 1500 Å using the F336W, F435W (F475W) and F606W filters for the HFF (A1689) galaxies at $1.0 < z < 1.6$, $1.6 < z < 2.2$ and $2.2 < z < 3.0$ samples, respectively. We note that these absolute magnitude values are corrected for the magnification from the strong gravitational lensing. In Figure 4.2, we present the UV spectral slope $\beta - M_{1500}$ distributions of our samples in three redshift ranges. For each sample, we show the β values from the power-law and SED-fitting approaches in the left and right panels, respectively. We also include some comparable measurements from Bouwens et al. (2009) probing the bright galaxies with $M_{UV} < -18.5$ at $z \sim 2.5$ as well as a recent study by Kurczynski et al. (2014) probing fainter galaxies with $M_{UV} < -14$ (-16) at $1 < z < 2$ $(2 < z < 3)$ utilizing the deep UVUDF data. However, taking advantage of the lensing magnification and deep *HST* data, our β measurements extend to an unprecedented magnitude of $M_{UV} = -12.5$ for the entire redshift range targeted in this study. Therefore, we study

the galaxies with UV luminosities 4× and 25× fainter than previous studies at $z < 2$ and $z > 2$, respectively.

In this section we quantify the relation between UV spectral slope β and M_{UV} for our faint samples. For this purpose, we start with calculating the Spearman's correlation coefficient to measure how significant these two parameters are correlated. As summarized in Table 4.1, a negative correlation between β and M_{UV} is found with a deviation of $4.4-7.2\sigma$ from a null hypothesis of no correlation. The existence of a correlation between β and M_{UV} has also been suggested in other studies at similar (e.g., Bouwens et al., 2009; Alavi et al., 2014; Kurczynski et al., 2014) or high redshifts (e.g., Bouwens et al., 2009, 2012b; Rogers et al., 2013; Bouwens et al., 2014). However, some other studies such as Hathi et al. (2016) at $2.0 < z < 2.5$ and Finkelstein et al. (2012); Dunlop et al. (2012, 2013) at higher redshifts, find no significant trend between their β and M_{UV} measurements. In this section, we first explain our methodology for quantifying this correlation and then we provide our best linear-fit parameters for the $\beta - M_{UV}$ distribution at each redshift.

4.4.1 Methodology

Similar to other studies in the literature, we parametrize the $\beta - M_{UV}$ relation using a linear fit. However, as discussed in different papers (e.g., Rogers et al., 2014), the $\beta - M_{UV}$ distribution includes an intrinsic scatter, which should be incorporated in the fitting procedure. We caution that a fitting model that does not account for the intrinsic scatter may result in a biased fit (Weiner et al., 2006). As described in Tremaine et al. (2002), for example, a precise data point (i.e., with small measurement error) located far from the actual fit (i.e., because of intrinsic scatter) can dictate the final fitting parameters, if we do not consider the intrinsic scatter in the data themselves.

Different studies follow different approaches to measure the best linear fit and the corresponding intrinsic scatter for the $\beta - M_{UV}$ distribution. Focusing on studies probing redshifts similar to our samples, (Bouwens et al., 2009; Kurczynski et al., 2014; Hathi et al., 2016), all perform a linear fit to their measurements without incorporating the intrinsic scatter

directly in their fitting approach. However, unlike Kurczynski et al. (2014) who use the individual measurements, Bouwens et al. (2009) and Hathi et al. (2016) fit to their biweight mean and median β determinations. In this work, we use a maximum likelihood (MLE) approach presented in Weiner et al. (2006) to incorporate the intrinsic scatter as an additional parameter in the linear-fitting procedure. This technique uses the same concept as the generalization of the χ^2 least-squares fitting formula, which has been used in Tremaine et al. (2002) and Williams et al. (2009). For a linear model of $\beta = aM_{UV} + b$, the probability distribution is define as below,

$$P(\beta_i, M_i) = \frac{1}{\sqrt{2\pi}\sigma_i}\exp(\frac{-(\beta_i - \beta_{\rm model})^2}{2\sigma_i^2}) \tag{4.1}$$

where $\beta_{\rm model}$ is the linear model, and σ_i is the total error computed as below,

$$\sigma_i^2 = \sigma_{\beta,i}^2 + a^2\sigma_{M,i}^2 + \sigma_{\rm int}^2 \tag{4.2}$$

where $\sigma_{\rm int}$ is the intrinsic scatter, which is added in quadrature to the observational uncertainties of $\sigma_{\beta,i}$ and $\sigma_{M,i}$. We note that the $\sigma_{M,i}$ value as the uncertainty in the absolute magnitude, accounts for uncertainty from photometric measurements, photometric redshifts as well as the lens models (Alavi et al., 2016). We then define the likelihood as the multiplication of probability distributions of all galaxies in the sample. Our best values of three parameters (a, b, $\sigma_{\rm int}$) and their uncertainties are derived via marginalizing the likelihood function. We present these values in Table 4.1 for all of our three samples and for both $\beta_{\rm power}$ and $\beta_{\rm SED}$ measurements.

Figure 4.2 compares our best linear fits (black solid line) for the $\beta_{\rm power} - M_{UV}$ and $\beta_{\rm SED} - M_{UV}$ relations on the left and right panels, respectively. It can be seen from Table 4.1 that the two linear fits (i.e., comparing best slopes and intercepts of $\beta_{\rm power}$ and $\beta_{\rm SED}$) are consistent for each sample. In addition, the estimate of intrinsic scatter for $\beta_{\rm power}$ distributions are comparable to or smaller than that of the $\beta_{\rm SED}$ distributions. We note that some caution must be taken when using the best linear fit parameters, particularly the

Table 4.1. β measurements

Redshift	$\rho_{Spear}(\sigma_{Spear})$[a]	slope[b]	intercept[c]	$\sigma_{\rm int}$[d]	β_1[e]	β_2[f]	β_3[g]
			Power-law fitting ($\beta_{\rm power}$)				
$1.0 < z < 1.6$	-0.27(4.4)	-0.07±0.02	-3.04±0.31	0.41±0.03	$-1.93^{-1.79}_{-1.97}$	$-2.00^{-1.91}_{-2.11}$	$-2.04^{-1.91}_{-2.18}$
$1.6 < z < 2.2$	-0.33(5.1)	-0.12±0.03	-3.78±0.41	0.39±0.03	$-1.70^{-1.64}_{-1.70}$	$-1.92^{-1.85}_{-2.05}$	$-2.21^{-1.72}_{-2.41}$
$2.2 < z < 3.0$	-0.39(6.1)	-0.14±0.02	-4.38±0.37	0.29±0.03	$-1.90^{-1.75}_{-1.96}$	$-2.22^{-2.11}_{-2.36}$	$-2.27^{-1.89}_{-2.46}$
			SED fitting ($\beta_{\rm SED}$)				
$1.0 < z < 1.6$	-0.31(5.0)	-0.09±0.02	-3.26±0.27	0.44±0.02	$-1.81^{-1.73}_{-1.90}$	$-1.98^{-1.89}_{-2.04}$	$-2.14^{-1.97}_{-2.16}$
$1.6 < z < 2.2$	-0.34(5.3)	-0.12±0.02	-3.86±0.34	0.45±0.02	$-1.79^{-1.76}_{-1.88}$	$-2.12^{-2.06}_{-2.17}$	$-2.20^{-1.81}_{-2.32}$
$2.2 < z < 3.0$	-0.47(7.2)	-0.16±0.02	-4.64±0.33	0.40±0.02	$-1.74^{-1.65}_{-1.85}$	$-2.09^{-2.06}_{-2.19}$	$-2.28^{-2.18}_{-2.43}$

[a] ρ_{Spear} shows the Spearman correlation coefficient and σ_{Spear} is the standard deviation from null hypothesis.

[b] The slope of the best linear fit to the $\beta - M_{UV}$ relation.

[c] The intercept of the best linear fit to the $\beta - M_{UV}$ relation.

[d] The intrinsic scatter around the best linear fit to the $\beta - M_{UV}$ relation.

[e] Median β for the magnitude bin of $M_{UV} = -17.75$.

[f] Median β for the magnitude bin of $M_{UV} = -15.75$.

[g] Median β for the magnitude bin of $M_{UV} = -13.75$.

intrinsic scatter, of the $\beta_{\rm SED}$ distributions. This is because, first, the uncertainty in $\beta_{\rm SED}$ values may be underestimated and thus the intrinsic scatter overestimated, as we do not include the errors associated with the stellar population models in SED fitting. Second, as a condition of our likelihood approach, the observed distribution (i.e., the $\beta - M_{UV}$ here) should be free of selection effects. However, as explained before, the SED approach can not recover the very blue spectral slopes accurately. Therefore, considering these caveats, throughout the rest of the paper, we focus more on our $\beta_{\rm power}$ measurements.

4.4.2 Compare a Constant and Changing Intrinsic Scatter

In our primary calculations of $\beta - M_{UV}$ relation, we assumed a null hypothesis that intrinsic scatter does not change with the UV magnitude. In order to quantify, how significant this assumption is relative to an alternative model where intrinsic scatter changes with luminosity, we run a likelihood ratio test. To this end, we first calculate the likelihood function as explained above but with an assumption of $\sigma_{int} = cM_{UV} + d$. We then calculate the likelihood ratio (i.e., a test statistic) as below,

$$D = 2\ln(\frac{L_{\rm alternative}}{L_{\rm null\ hypothesis}}) \tag{4.3}$$

where the likelihood is the maximum likelihood for each model. We estimate the D values for our $\beta_{\rm power}$ likelihoods to be D=2.51, 1.54, 0.27. Considering a degree of freedom of one[2], we derive the p-values to be p-value=0.11, 0.22 and 0.60. Knowing that a p-value of 0.05 is often used as cutoff for significant deviation from null model, our p-values indicate that the data do not require an intrinsic scatter that changes with luminosity.

4.5 Comparison to the Other Studies

As we demonstrated in Section 4.4, for all of our samples spanning a wide redshift range of $1 < z < 3$, there is a clear correlation between the β and M_{UV} measurements. Our β

[2] The degree of freedom is calculated as the difference between the free parameters in the alternative and null models.

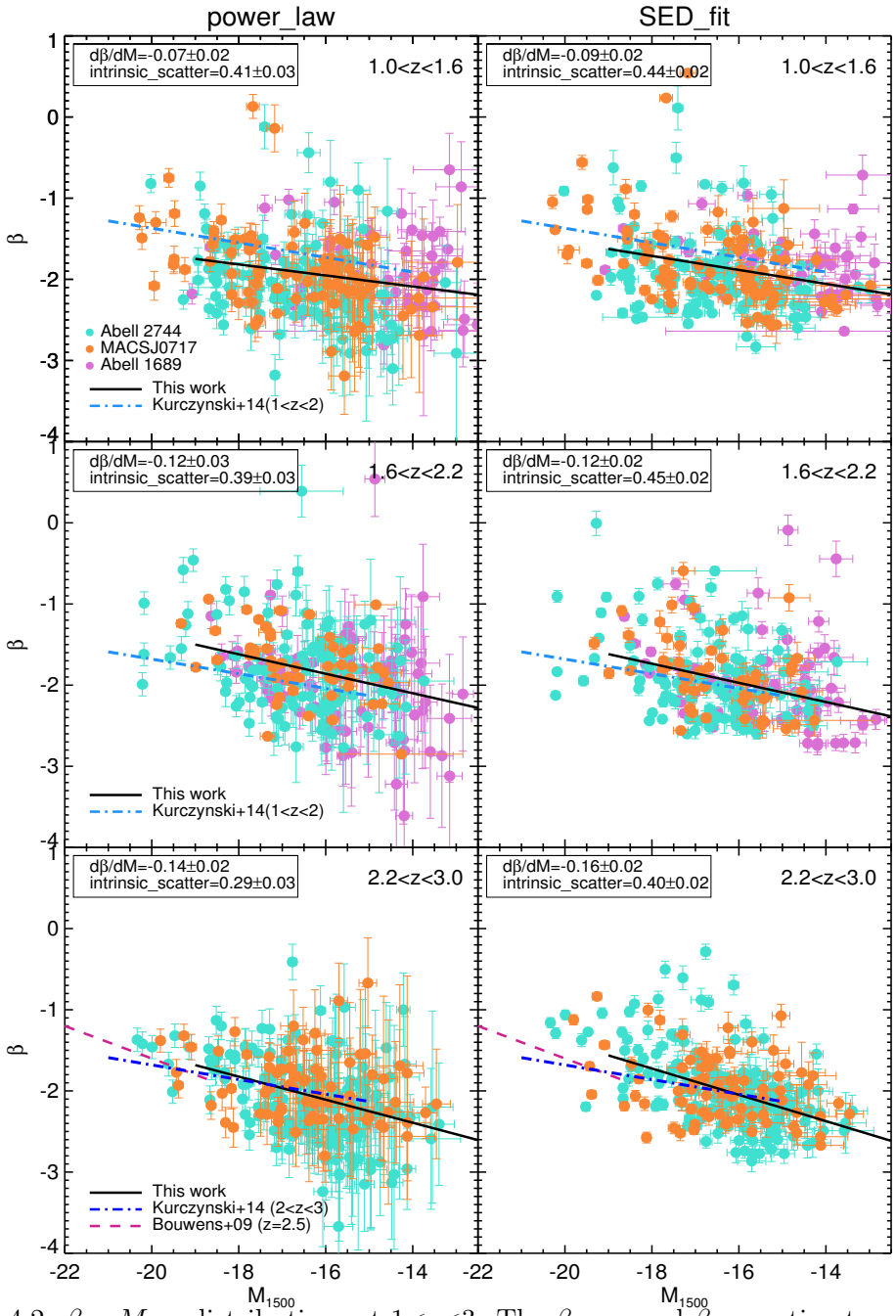

Figure 4.2: $\beta - M_{UV}$ distributions at 1<z<3. The $\beta_{\rm power}$ and $\beta_{\rm SED}$ estimates are shown in the left and right panels, respectively. The filled purple, cyan and orange circles represent the individual UV spectral slope values for A1689, A2744 and M0717 galaxies, respectively. The black solid line in each panel shows the best linear fit via the MLE technique. The slope and intrinsic scatter values from the fitting procedure are shown in the upper-left boxes. In addition, we include the best linear fits from Kurczynski et al. (2014) (dotted-dashed blue lines) and Bouwens et al. (2009) (dashed purple) studies.

estimates, from both approaches, of the faint galaxies follow a trend similar to what has been seen before for brighter galaxies at similar redshifts (Meurer et al., 1999; Labbé et al., 2007; Bouwens et al., 2009; Kurczynski et al., 2014) as well as high redshifts (Bouwens et al., 2009; Lee et al., 2011; Wilkins et al., 2011; Bouwens et al., 2012b; Castellano et al., 2012; Rogers et al., 2013; Bouwens et al., 2014), in the sense that galaxies with lower UV luminosities have on average bluer UV continuum slopes. As presented in Table 4.1, our measurements for the slope ($d\beta/dM_{UV}$) of the $\beta_{\rm power} - M_{UV}$ relations are -0.07 ± 0.02, -0.12 ± 0.03 and -0.14 ± 0.02 for $1.0 < z < 1.6$, $1.6 < z < 2.2$ and $2.2 < z < 3.0$ samples, respectively. First, we compare our results with Kurczynski et al. (2014), because they probe similar redshift and magnitude ranges as our samples. Kurczynski et al. (2014) derive $d\beta/dM_{UV} = -0.09 \pm 0.05$ and -0.09 ± 0.04 for their samples at $z = 1.5$ and 2.5, respectively. Our inferred $d\beta/dM_{UV}$ values at $z = 1.3$ and $z = 1.9$ are consistent with their estimates within the uncertainties. However, our $z = 2.6$ slope is steeper than their estimate at $z = 2.5$. They actually claim that the $d\beta/dM_{UV}$ does not change with redshift and it has an average of -0.11 ± 0.01 at all redshifts between $1 < z < 8$. However, our estimates suggest an evolution with redshift such that the $d\beta/dM_{UV}$ value becomes steeper at higher redshifts. A similar trend for steepening $d\beta/dM_{UV}$ is seen in the calculations of Bouwens et al. (2009, 2012b, 2014) for higher redshifts $z > 4$, as well. Regarding our slope estimate at $z = 2.6$, we have a shallower value than Bouwens et al. (2009) result with a slope of -0.2 ± 0.04 at $z = 2.5$. We note that unlike our faint galaxies, their sample covers only bright galaxies with $M_{UV} < -18.5$. These different luminosity ranges might explain the different inferred slopes because some studies (Bouwens et al., 2014) suggest a piecewise-linear function to describe the $\beta - M_{UV}$ relation, with a weaker slope at faint luminosities.

As discussed in the previous section, we find no significant trend between the intrinsic scatter and the UV luminosity and we derive $\sigma_{\rm int} = 0.41 \pm 0.03$, 0.39 ± 0.03 and 0.29 ± 0.03 for our $z = 1.3$, $z = 1.9$ and $z = 2.6$ samples with $-20.5 < M_{UV} < -12.5$, respectively. Based on these measurements, the intrinsic scatter seems to be larger at $z < 1.9$ than at higher redshift. Similarly, Kurczynski et al. (2014) concluded a larger scatter of $\sigma = 0.43$ for

their β measurements at $z < 2$ than their estimate of $\sigma = 0.36$ at higher redshifts. However, we caution that they use the standard deviation of the β distribution at each magnitude bin as an estimate of the scatter. Because they do not subtract the effect of measurement errors, their intrinsic scatter is likely to be an overestimate. On the other hand, Bouwens et al. (2009) measured the intrinsic scatter via correcting for the photometric errors and derived $\sigma = 0.27 - 0.36$ for a magnitude range of $-21.73 < M_{UV} < -18.73$ at z=2.5. In particular, they estimate $\sigma = 0.36$ at $M_{UV} = -18.73$, which is in general agreement with our estimate of the intrinsic scatter for the $z = 2.6$ sample. However, their results are not directly comparable with ours, because they probe a brighter sample of galaxies. As suggested by several studies including Rogers et al. (2014), the intrinsic scatter in $\beta - M_{UV}$ relation increases with luminosity at bright magnitudes.

4.6 Dependence of β on Redshift

In this section, we investigate the redshift evolution of the UV continuum slope β between $1 < z < 3$ and compare with the higher redshift studies. As we know that the UV continuum slope β changes with luminosity and also the luminosity distribution is different for each redshift, we first define two magnitude bins centered at $M_{UV} = -17.75$ and $M_{UV} = -15.75$ with width of 1 mag for each sample and then study the redshift evolution of the corresponding β values. These magnitude bins are selected such that there is enough number of galaxies for statistical estimates and previous determinations are available for comparison. Binning over magnitude also allows us to understand the luminosity dependence of the redshift evolution.

We calculate the median value of the β distribution for each magnitude bin for each sample. We choose the median as it is a robust statistic against any outlier in the distribution. Similar to the approach used in Finkelstein et al. (2012), the uncertainty on the median value of β for each magnitude bin is calculated via running a Monte Carlo simulation. To this end, we randomly propagate the flux measurements within the photometric

uncertainties for each individual galaxy in that magnitude bin and then refit the UV spectral slope using a power-law function. We then calculate the median value of these random β measurements. This simulation is repeated 1000 times to provide a distribution of median β values. Finally, we compute the uncertainty of the median using the 68% confidence interval of this distribution. We also incorporate the Poisson noise for the number of galaxies within each magnitude bin. To this end, for each random sampling of 1000 realizations, we select N random number of galaxies assuming a Poisson distribution with mean equal to the total number of galaxies in the corresponding bin. In Table 4.1, we present these calculations for each magnitude and redshift bin for both $\beta_{\rm power}$ and $\beta_{\rm SED}$ distributions.

Figure 4.3 illustrates how the median of the β distributions evolves with redshift between $1 < z < 7$. The bright ($M_{UV} = -17.75$), intermediate ($M_{UV} = -15.75$) and faint ($M_{UV} = -13.75$) magnitude bins are shown in the upper and lower panels, respectively. We also include the results from Kurczynski et al. (2014) probing the redshift range of z=1-6 as well as Bouwens et al. (2014) with z=4-7. Although there are other measurements of β distributions at these redshifts in the literature, we use these papers because they are the only samples that probe these magnitudes. We note that the values from Kurczynski et al. (2014) are biweight mean estimates of their β distributions (Figure 4 in their paper). However, for Bouwens et al. (2014), we are using the median values presented in their Table 2. As seen in this Figure, the median β values become bluer (i.e., more negative) with increasing redshift from z=1 to z=7. Combining our median values with the measurements from the other studies shown in Figure 4.3, we derive the best linear fit with slope of $d\beta/dz = -0.06 \pm 0.02$, $d\beta/dz = -0.12 \pm 0.04$ and $d\beta/dz = -0.18 \pm 0.12$ for the bright, intermediate and faint magnitude bins, respectively. From these slope estimates, the evolution of β for the bright galaxies seems to be slower than for the faint galaxies. This can also be seen if we only consider our data points (filled black circles) between $z = 1 - 3$.

There are several different explanations for the reddening of galaxy UV colors with redshift. As we sample galaxies at $1 < z < 3$ in this study, we only focus on the possible explanations of the reddening for this redshift range. In particular, we focus on the magni-

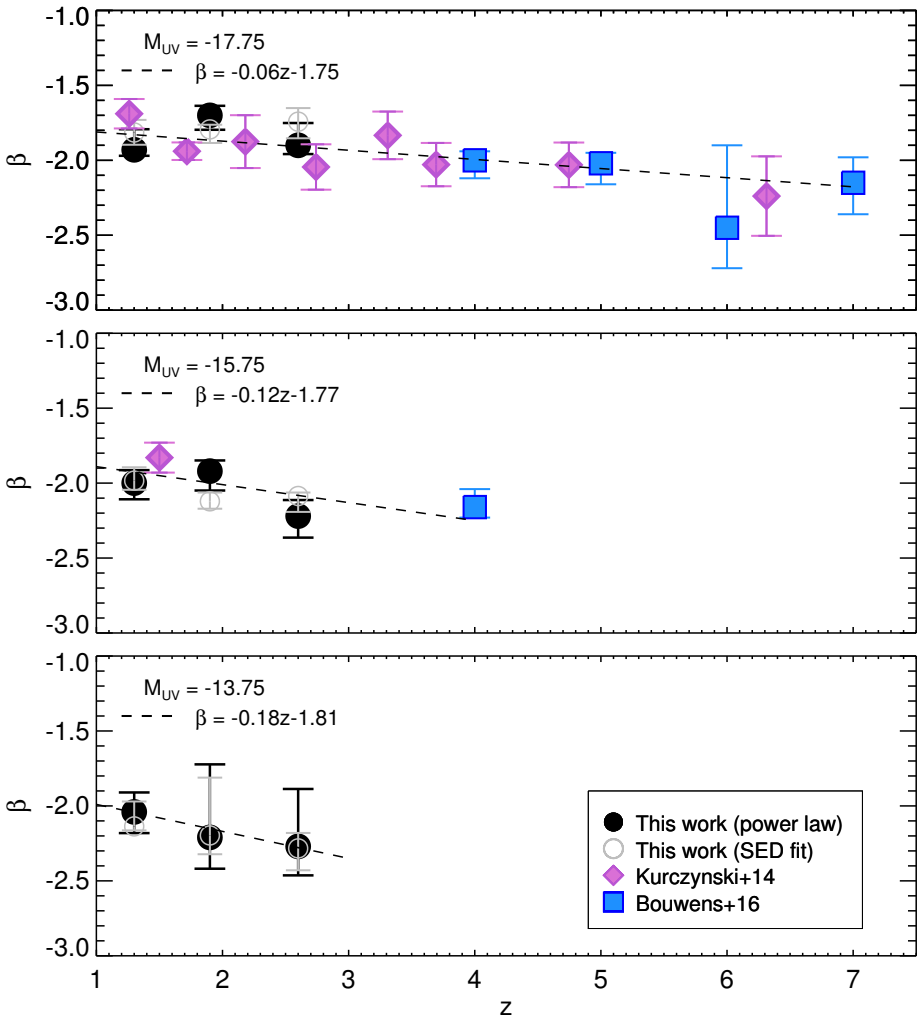

Figure 4.3: The evolution of the median UV-continuum slope with redshift. The filled black circles (open gray circles) represent the median of our $\beta_{\rm power}$ ($\beta_{\rm SED}$) distributions for magnitude bins of $M_{UV} = -17.75$, $M_{UV} = -15.75$ and $M_{UV} = -13.75$ shown in the top, middle and bottom panels, respectively. The blue square and purple diamonds show the median and biweight mean measurements from Kurczynski et al. (2014) and Bouwens et al. (2014), respectively. Our estimates of the best linear fit are shown with dashed lines. There is a clear redshift dependence showing that β slopes become redder at lower redshifts.

tude bins of $M_{UV} = -15.75$ and $M_{UV} = -13.75$, because the change in UV slope is larger, with $\Delta\beta = 0.2$. As shown in many studies (e.g., Labbé et al., 2007; Bouwens et al., 2009, 2012b; Finkelstein et al., 2012), the β slope is affected by various physical properties such as the dust attenuation, stellar metallicity, age and stellar IMF. We do not discuss the effect of varying IMF, as it is difficult to directly constrain the IMF at high redshifts.

To address the other properties, we perform a simple test using the BC03 models. We select a fiducial model with Chabrier IMF (Chabrier, 2003), 0.2 $Z_{\odot}$, an age of 100 Myr and E(B-V)=0.1, to have $\beta = -2.2$ similar to our median β at $z = 2.6$. We then change one parameter each time and calculate its effect on the UV spectral slope. We start with the metallicity because it has the least effect as suggested in several other studies (Bouwens et al., 2009, 2012b; Finkelstein et al., 2012), as well. In order to have a change of $\Delta\beta = 0.2$, we need to increase the metallicity by a factor of 5 to be 1 $Z_{\odot}$. However, this large increase in the metallicity of galaxies between z=1-3 is not supported by the simulations and observations. For example, Ma et al. (2016) who use the FIRE simulations (Hopkins et al., 2014) to study the evolution of mass-metallicity relation at z=1-3, predict a very smaller change, a factor of ~ 1.7, in the metallicity of galaxies with $M_* = 10^8$ (i.e., similar to the stellar mass of our faint galaxies from SED fitting). Such a change in the metallicity would results in a very small change in β compared to our observed difference. This small change in metallicity is also seen in an observational work by Yuan et al. (2013), who use a sample of gravitationally lensed galaxies with $3 \times 10^7 < M_* < 6 \times 10^{10}$, comparable to our samples. They derive a mean rise of 0.055 dex Gyr^{-1} in metallicity for z=2.5 to z=0.8. This change is very similar to what is estimated in Ma et al. (2016).

For the next test, we fix the metallicity and dust extinction but we run BC03 with constant SFH for an age of 1 Gyr. As a consequence, the β value changes with $\Delta\beta \sim 0.2$. This change in the age parameter is comparable to the range of ages covered in our $z \sim 1.3$ and $z \sim 2.6$ samples. Finally, increasing the dust extinction to $E(B-V) = 0.14$ (i.e, a 0.04 mag change relative to our fiducial model), can justify the reddening of the UV color.

Therefore, we conclude that the observed change in the median UV continuum slope β toward redder colors, can be explained via changes in the stellar age and/or the dust extinction. In addition, the metallicity effects could also explain part of the evolution. However, as discussed in various studies (Bouwens et al., 2009, 2012b; Finkelstein et al., 2012), the variations in the UV continuum slope at higher redshifts (i.e., $z > 4$) is often associated only with the dust extinction.

4.7 Discussion

In section 4.4, we presented statistical evidence for the existence of a correlation between the UV spectral slope and UV luminosity with some intrinsic scatter. A physical interpretation of this correlation and its scatter is not straightforward, because many different properties of galaxies can change the UV spectral slope, including dust extinction, metallicity, and star formation history. One would expect these dependencies because galaxies build dust and metals when they grow in luminosity and mass and thus they become redder.

In high-redshift studies of bright galaxies (Bouwens et al., 2009; Wilkins et al., 2011; Bouwens et al., 2012b, 2014), a common interpretation is that the variation and scatter of the mean β with luminosity is due to different levels of dust extinction. Of course the other factors such as metallicity and stellar age vary as well, but they have a small impact on the slope and scatter of the $\beta - M_{UV}$ relation.

In this section, we will discuss how we should interpret the $\beta - M_{UV}$ slope and intrinsic scatter for the faint galaxies targeted in this study. In particular, we more carefully quantify the effect of SFH on the UV continuum colors of faint galaxies and their scatter.

4.7.1 Bursty Star Formation History in Faint Galaxies

Recent hydro-dynamical simulations (e.g., Governato et al., 2012; Hopkins et al., 2014; Trujillo-Gomez et al., 2015) that implement stellar feedback (e.g., supernova and stellar winds), predict frequent dramatic changes in the star formation rate of low-mass galaxies

on very short time scales of < 10 Myr (i.e., time scale similar to the O-type star lifetime). Several studies (e.g., Domínguez et al., 2015; Sparre et al., 2015) have used these simulations with bursty SFHs to examine the effect of these variable short-timescale SFRs on different galaxy properties (i.e., stellar mass, Lyα equivalent width) as well as observational relations (i.e, SFR-M_* relation).

Here, we aim to understand how the bursty SFHs in low-mass galaxies change the UV continuum color and whether they affect the $M_{UV} - \beta$ relation. To this end, we examine a sample of simulated galaxies with bursty SFHs. Recently, Domínguez et al. (2015) used a sample of 11 galaxies from a simulation by Governato et al. (2012) and investigated the consequences of bursty SFHs on dwarf galaxy observables at high redshifts. Here, we use the same galaxies to study the distribution of their UV continuum slope β and compare with our high-redshift faint galaxies. Below, we provide a brief summary of these simulations and galaxies, but a detailed description is given in Domínguez et al. (2015).

These galaxies are from a high-resolution simulation where the energy output from supernova feedback and stellar winds turns off the star formation and thus produces the bursty SFHs in low mass galaxies (i.e., $M_* < 10^9$). In Figures 4.4 and 4.5, we show the bursty SFHs of these galaxies when the universe is between 2.5 and 3.5 Gyr old. The galaxies from top to bottom and left to right are ordered by increasing stellar mass at z=2. This figure clearly shows that the change in the SFR is larger and over shorter time scales for lower mass galaxies than it is for their more massive counterparts. We run the BC03 models implementing these bursty SFHs to build the SEDs and calculate the stellar masses of our simulated galaxies. We note that *no* dust extinction is included here. We measure the stellar masses to be between $6.97 < \log_{10}(M_*/M_\odot) < 9.94$ at $z = 2.0$. To compare with our observed lensed galaxies, we extract the SEDs for every time step of 5 Myr, in total 201 values, at redshifts of $1.97<z<2.74$ (i.e., corresponding to the age of universe between 2.5-3.5 Gyr). We note that we incorporate the effect of nebular emission (continuum and nebular lines) using the prescription given in Salmon et al. (2015). Because nebular emission is directly proportional to the number of ionizing photons, adding the nebular contributions redden the

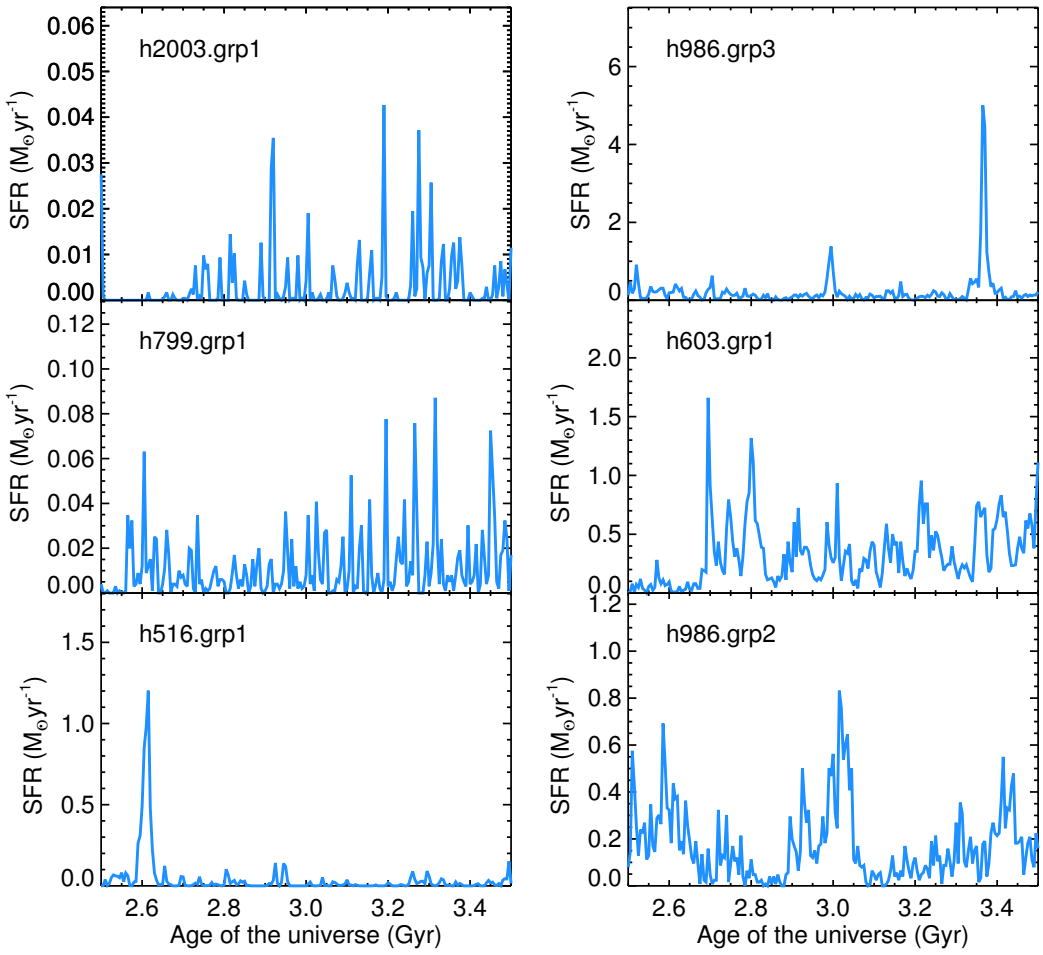

Figure 4.4: This plot shows the bursty SFHs of simulated galaxies when the universe is between 2.5 and 3.5 Gyr old. The value of the stellar masses of these galaxies are given in the text. The galaxies are ordered based on their stellar masses such that the galaxy h2003.grp1 is the least massive galaxy with $\log(M_*/M_\odot) = 6.97$. It is clear that the lower mass galaxies have larger changes in their SFR over short time scales.

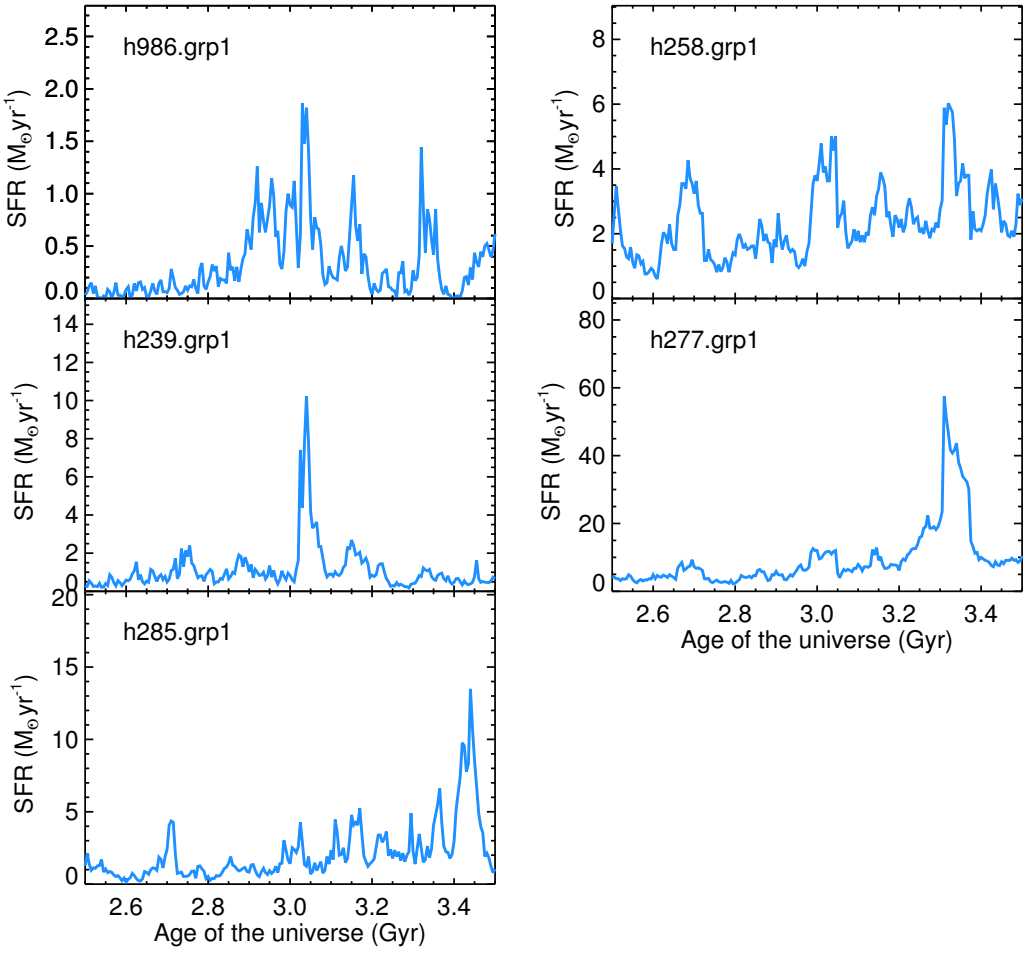

Figure 4.5: Same as Figure 4.4, for the rest of the simulated galaxies.

very blue SEDs more than the red SEDs, however the change is small ($\Delta\beta < 0.2$). Finally, We measure the UV absolute magnitude as well as the UV spectral slope utilizing the same methodology that we did for $\beta_{\rm SED}$ for our observed galaxies. Figure 4.6 shows the $\beta - M_{UV}$ distribution for each simulated galaxy represented by a different color. The name of each galaxy is specified in the inset, from top to bottom ordered by increasing stellar mass at z=2 with $\log(M_*/M_\odot)$=[6.97, 7.07, 7.70, 8.29, 8.35, 8.41, 8.51, 9.09, 9.33, 9.43, 9.94]. Therefore, galaxies h2003grp1 and h277.grp1 shown with blue and red circles are the least and most massive galaxies in the simulation.

Figure 4.6 clearly shows that the bursty SFH can cause dramatic changes in the UV spectral slope β, with larger changes at lower luminosities. The UV continuum slope varies because these galaxies are not constantly replenishing UV-bright stars (i.e., responsible for the β slope). From this plot, we can see that the very low-mass galaxies (e.g., h516.grp1) become very red ($\beta > -1$) when their star formation has been recently quenched.

Using these measurements, we run a Monte Carlo simulation to predict a $\beta - M_{UV}$ distribution that we expect for the real galaxies. First, we randomly sample from an observed stellar-mass function of star-forming galaxies at $z \sim 2$. The stellar-mass function that we adopt here, is from Tomczak et al. (2014) at $2 < z < 2.5$ and described using a single-Schechter function (from their Table 3). For each random stellar mass value, we assign a random β and M_{1500} pair from the simulated $\beta - M_{1500}$ distribution (i.e., Figure 4.6). We then calculate the probability of having this random pair in our magnitude limited samples. In Figure 4.7, the gray squares show the final realizations from the Monte Carlo simulation. For comparison, the observed galaxies with $1.97 < z < 2.74$ are overplotted, as well.

To quantify these changes, we split the simulated $\beta - M_{UV}$ distribution into three magnitude bins of $-20 < M_{UV} < -18$, $-18 < M_{UV} < -16$ and $-16 < M_{UV} < -14$ to be comparable with our observed samples and measure the standard deviation to be σ =0.13, 0.20 and 0.29, respectively. We limit our magnitude bins to $M_{UV} < -14$, because the $\beta - M_{UV}$ distribution from the simulation is incomplete at fainter magnitudes (see Figure 4.6). We also calculate the intrinsic scatter in the β distribution of the observed galaxies at

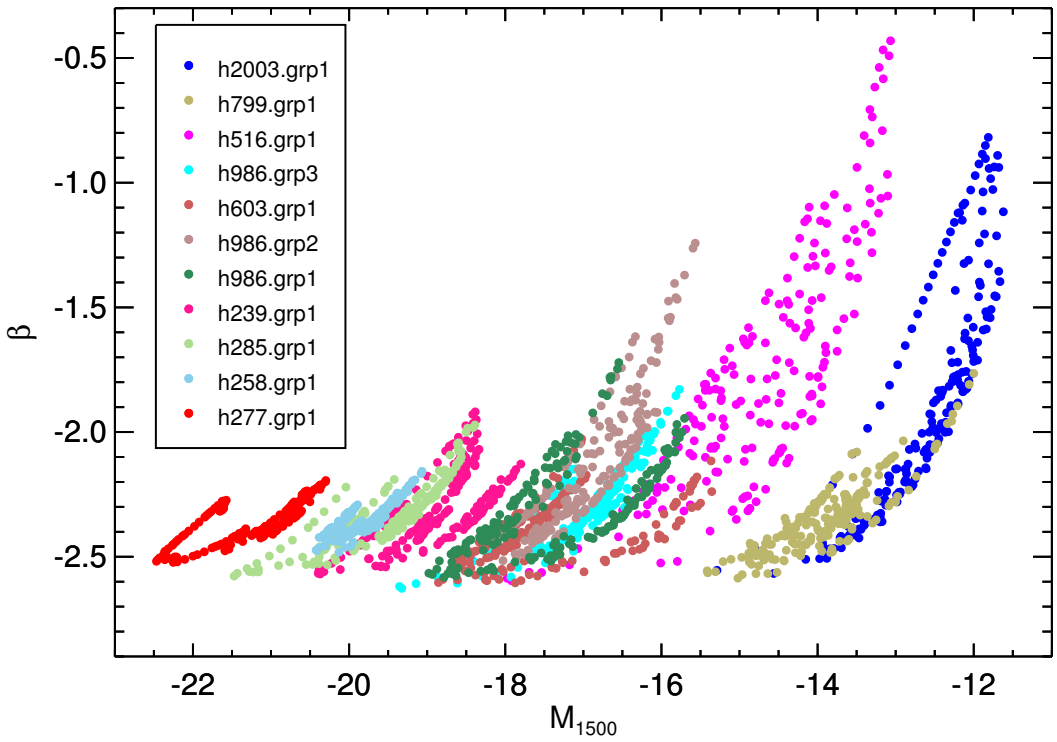

Figure 4.6: $\beta - M_{1500}$ distribution of simulated galaxies with bursty SFHs. Each color shows the measurement for a time step of 5 Myr for each galaxy. The name of the galaxies given in the box are ordered by stellar mass with the lowest mass galaxy first (see text). The change in the UV spectral slope β increases as luminosity decrease (e.g., moving from red symbols toward blue points).

$1.97 < z < 2.74$, shown in Figure 4.7, to be $\sigma_{int} = 0.3 \pm 0.03$, via the same MLE technique that we used in section 4.4.1. For the bright magnitude bins (i.e., with $M_{UV} < -16$), we need to add the effect of dust reddening to explain the true red β values of these galaxies (i.e., shown with the dashed line) relative to the blue β predictions. However, the effect of dust on the intrinsic scatter is more complicated. Naively, one would expect the dust extinction to increase the predicted scatter. However, it is possible that dust could decrease the scatter, if the dust extinction occurs preferentially in the burst phase. This is reasonable, as the stars are more embedded when they are extremely young. For the faint magnitude bin, $-16 < M_{UV} < -14$, the predicted scatter due to the bursty SFHs is consistent with the scatter in the observed galaxies.

4.7.2 Dust reddening, Metallicity and Future Work

As we demonstrated above, the simulated galaxies with bursty SFHs cover a broad range of β values, and thus predict a large scatter around the typical UV continuum slopes that one would expect for a representative SFH (i.e., constant). This indicates that the bursty SFH can explain the red β slopes as well as the intrinsic scatter observed for our lensed faint galaxies. However, this does not rule out the existence of dust extinction in these galaxies. Indeed, to explain the slope of the $\beta - M_{UV}$ relation at faint luminosities, one needs to take into account the effect of dust reddening as well as the metallicity.

To understand which factor is dominating at these low stellar-mass regimes, we need an accurate estimate of dust extinction and metallicity of these faint galaxies. Although, at high-redshift, the UV continuum slope is often used as a direct estimator of dust extinction, it is more complicated for faint galaxies due to their stochastic SFH. Therefore, one needs to measure the dust extinction in a way independent of any initial assumption about the SFH. To this end, we have conducted spectroscopic observations of our faint galaxies using the multi-object near-IR spectrograph MOSFIRE (McLean et al., 2010, 2012) at the Keck Observatory. We have obtained spectra for 132 of our lensed galaxies in A1689 and M0717 as well as another HFF cluster M1149, in Y, J, H and K filters. Measuring the nebular

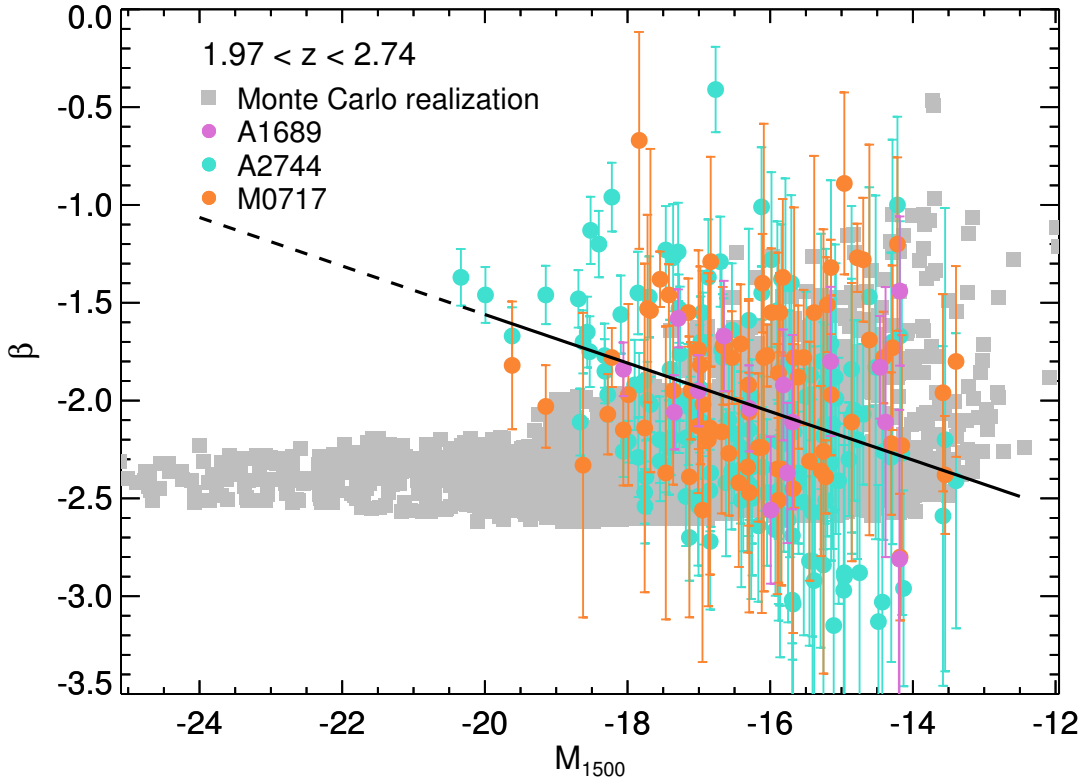

Figure 4.7: Comparing the $\beta - M_{UV}$ distribution from the simulation with bursty SFHs and observed galaxies. The gray filled circles represent the prediction of the $beta - M_{UV}$ distribution from the random realizations of the Monte Carlo simulation. The purple, cyan and orange circles show the observed β measurements at $1.97 < z < 2.74$ for the A1689, A2744 and M0717 clusters, respectively. The solid black line shows the best linear-fit to the observed data.

emission lines, we can precisely estimate the dust extinction via the Balmer decrement ratio (i.e., ratio of Hα/Hβ) as well as the metallicity. This allows us to distinguish the effect of dust extinction and metallicity from the bursty SFHs in reddening the UV continuum colors of faint galaxies.

4.8 Summary

In this paper, we have utilized the deep UV and optical data of three lensing galaxy clusters to quantify the distribution of UV continuum slopes β for faint galaxies at $1 < z < 3$. Because of the magnification of strong gravitational lensing from these foreground clusters, we assemble a large sample of 760 faint galaxies down to $M_{UV} = -12.5$.

We obtain a robust measurement of the UV continuum slopes β for these faint galaxies by fitting a power law function to the broad-band photometry available within the $1250 - 2600$ Å wavelength range. We also estimate the β values by fitting to the best-fit synthetic stellar population model for each galaxy. As discussed in the paper, these two measurements of UV slopes are consistent. We apply a maximum likelihood methodology to compute the slope and intrinsic scatter in the $\beta - M_{UV}$ distributions and then compare our findings with the previous calculations in the literature. Below, we summarize e our conclusions:

- We find that the faint star-forming galaxies with $-20 < M_{UV} < -12.5$ at $1 < z < 3$, lie along a trend between UV spectral slope β and UV absolute magnitude M_{UV}, similar to what has been found for the bright galaxies. At these low luminosity ranges, the galaxies become bluer at fainter M_{UV} magnitudes with a rate of $d\beta/dM_{UV} = -0.07 \pm 0.02$, -0.12 ± 0.03 and -0.14 ± 0.02 at $1.0 < z < 1.6$, $1.6 < z < 2.2$ and $2.2 < z < 3.0$, respectively. These slope estimates are in general agreement with other studies covering the brighter galaxies at similar redshifts (Bouwens et al., 2009; Kurczynski et al., 2014).

- We observed a redshift evolution in the median β values of galaxies with a given UV luminosity, such that galaxies are bluer at higher redshifts. However, focusing on the

redshift ranges covered in this study, this evolution is weak for bright magnitude bins, $M_{UV} = -17.75$, relative to the stronger evolution seen for the faint magnitudes with $M_{UV} = -15.75$. Combining our estimates with the median measurements from the literature extending to z=7, we derive $d\beta/dz = -0.06 \pm 0.02$ and -0.12 ± 0.04 for the magnitude bins of $M_{UV} = -17.75$ and $M_{UV} = -15.75$, respectively. We argue that the changes ($\Delta\beta \sim 0.2$) of the UV continuum slope of faint galaxies with redshift can can be understood via the evolution in the dust reddening (by ΔE(B-V)=0.04) and/or the stellar ages of galaxies (with Δage=0.9 Gyr) between $z = 1 - 3$.

- Our β distributions at all three samples show significant evidence for a large intrinsic scatter in the $\beta - M_{UV}$ relation. For the first time over a wide luminosity range of faint galaxies, we quantify this intrinsic scatter through a maximum likelihood approach. Based on our statistical analyses, we do not find significant evidence for a changing intrinsic scatter with luminosity, and estimate the intrinsic scatter to be 0.41 ± 0.03, 0.39 ± 0.03 and 0.29 ± 0.03 in our $z \sim 1.3$, $z \sim 1.9$ and $z \sim 2.6$ samples, respectively.

- Although many studies of bright galaxies at high redshifts consider dust extinction as the principal parameter explaining the slope and scatter in the $\beta - M_{UV}$ distribution, here we try to find other possible reasons for the observed intrinsic scatter at faint luminosities. We use a hydro-dynamical simulation of dwarf galaxies with largely variable SFRs over cosmic time, to assess whether the burstiness can be used as an alternative explanation. Intriguingly, the bursty SFHs produce a large scatter in the β distribution of each simulated galaxy within its lifetime. Our further quantifications show that while the predicted scatter ($\sigma = 0.13 - 0.20$) due to bursntiness at M_{UV}<-16 is smaller than our measured intrinsic scatter for the observed lensed galaxies ($\sigma_{\rm int} = 0.3 \pm 0.03$), the predicted scatter ($\sigma = 0.29$) at M_{UV}>-16 is consistent with the observations. As a consequence for the brighter galaxies, as suggested in other works (Bouwens et al., 2012b; Rogers et al., 2013), the effect of different levels of dust extinction is likely the main source of scatter in the β values; however, the bursty

SFHs at low luminosities can cause a large scatter without considering any effect of dust reddening.

References

Adelberger, K. L. and Steidel, C. C.: 2000, *ApJ* **544**, 218

Adelberger, K. L., Steidel, C. C., Shapley, A. E., Hunt, M. P., Erb, D. K., Reddy, N. A., and Pettini, M.: 2004, *ApJ* **607**, 226

Alamo-Martínez, K. A., Blakeslee, J. P., Jee, M. J., Côté, P., Ferrarese, L., González-Lópezlira, R. A., Jordán, A., Meurer, G. R., Peng, E. W., and West, M. J.: 2013, *ApJ* **775**, 20

Alavi, A., Siana, B., Richard, J., Rafelski, M., Jauzac, M., Limousin, M., Freeman, W. R., Scarlata, C., Robertson, B., Stark, D. P., Teplitz, H. I., and Desai, V.: 2016, *ArXiv e-prints*

Alavi, A., Siana, B., Richard, J., Stark, D. P., Scarlata, C., Teplitz, H. I., Freeman, W. R., Dominguez, A., Rafelski, M., Robertson, B., and Kewley, L.: 2014, *ApJ* **780**, 143

Arnouts, S., Schiminovich, D., Ilbert, O., Tresse, L., Milliard, B., Treyer, M., Bardelli, S., Budavari, T., Wyder, T. K., Zucca, E., Le Fèvre, O., Martin, D. C., Vettolani, G., Adami, C., Arnaboldi, M., Barlow, T., Bianchi, L., Bolzonella, M., Bottini, D., Byun, Y.-I., Cappi, A., Charlot, S., Contini, T., Donas, J., Forster, K., Foucaud, S., Franzetti, P., Friedman, P. G., Garilli, B., Gavignaud, I., Guzzo, L., Heckman, T. M., Hoopes, C., Iovino, A., Jelinsky, P., Le Brun, V., Lee, Y.-W., Maccagni, D., Madore, B. F., Malina, R., Marano, B., Marinoni, C., McCracken, H. J., Mazure, A., Meneux, B., Merighi, R., Morrissey, P., Neff, S., Paltani, S., Pellò, R., Picat, J. P., Pollo, A., Pozzetti, L., Radovich, M., Rich, R. M., Scaramella, R., Scodeggio, M., Seibert, M., Siegmund, O., Small, T., Szalay, A. S., Welsh, B., Xu, C. K., Zamorani, G., and Zanichelli, A.: 2005, *ApJL* **619**, L43

Atek, H., Richard, J., Jauzac, M., Kneib, J.-P., Natarajan, P., Limousin, M., Schaerer, D., Jullo, E., Ebeling, H., Egami, E., and Clement, B.: 2015a, *ApJ* **814**, 69

Atek, H., Richard, J., Kneib, J.-P., Clement, B., Egami, E., Ebeling, H., Jauzac, M., Jullo, E., Laporte, N., Limousin, M., and Natarajan, P.: 2014, *ApJ* **786**, 60

Atek, H., Richard, J., Kneib, J.-P., Jauzac, M., Schaerer, D., Clement, B., Limousin, M., Jullo, E., Natarajan, P., Egami, E., and Ebeling, H.: 2015b, *ApJ* **800**, 18

Baggett, S. M., Noeske, K., Anderson, J., MacKenty, J. W., and Petro, L.: 2012, in *Society of Photo-Optical Instrumentation Engineers (SPIE) Conference Series*, Vol. 8453 of *Society of Photo-Optical Instrumentation Engineers (SPIE) Conference Series*

Bartelmann, M.: 2010, *Classical and Quantum Gravity* **27(23)**, 233001

Beckwith, S. V. W., Stiavelli, M., Koekemoer, A. M., Caldwell, J. A. R., Ferguson, H. C., Hook, R., Lucas, R. A., Bergeron, L. E., Corbin, M., Jogee, S., Panagia, N., Robberto, M., Royle, P., Somerville, R. S., and Sosey, M.: 2006, *AJ* **132**, 1729

Belli, S., Jones, T., Ellis, R. S., and Richard, J.: 2013, *ApJ* **772**, 141

Benson, A. J., Bower, R. G., Frenk, C. S., Lacey, C. G., Baugh, C. M., and Cole, S.: 2003, *ApJ* **599**, 38

Bertin, E. and Arnouts, S.: 1996, *A&AS* **117**, 393

Blanton, M. R. and Roweis, S.: 2007, *AJ* **133**, 734

Bouwens, R.: 2016, in A. Mesinger (ed.), *Understanding the Epoch of Cosmic Reionization: Challenges and Progress*, Vol. 423 of *Astrophysics and Space Science Library*, p. 111

Bouwens, R., Bradley, L., Zitrin, A., Coe, D., Franx, M., Zheng, W., Smit, R., Host, O., Postman, M., Moustakas, L., Labbe, I., Carrasco, M., Molino, A., Donahue, M., Kelson, D. D., Meneghetti, M., Jha, S., Benitez, N., Lemze, D., Umetsu, K., Broadhurst, T., Moustakas, J., Rosati, P., Bartelmann, M., Ford, H., Graves, G., Grillo, C., Infante, L., Jiminez-Teja, Y., Jouvel, S., Lahav, O., Maoz, D., Medezinski, E., Melchior, P., Merten, J., Nonino, M., Ogaz, S., and Seitz, S.: 2012a, *ArXiv e-prints*

Bouwens, R. J., Illingworth, G. D., Blakeslee, J. P., Broadhurst, T. J., and Franx, M.: 2004, *ApJL* **611**, L1

Bouwens, R. J., Illingworth, G. D., Bradley, L. D., Ford, H., Franx, M., Zheng, W., Broadhurst, T., Coe, D., and Jee, M. J.: 2009, *ApJ* **690**, 1764

Bouwens, R. J., Illingworth, G. D., Franx, M., and Ford, H.: 2007, *ApJ* **670**, 928

Bouwens, R. J., Illingworth, G. D., Oesch, P. A., Franx, M., Labbé, I., Trenti, M., van Dokkum, P., Carollo, C. M., González, V., Smit, R., and Magee, D.: 2012b, *ApJ* **754**, 83

Bouwens, R. J., Illingworth, G. D., Oesch, P. A., Labbé, I., Trenti, M., van Dokkum, P., Franx, M., Stiavelli, M., Carollo, C. M., Magee, D., and Gonzalez, V.: 2011, *ApJ* **737**, 90

Bouwens, R. J., Illingworth, G. D., Oesch, P. A., Labbé, I., van Dokkum, P. G., Trenti, M., Franx, M., Smit, R., Gonzalez, V., and Magee, D.: 2014, *ApJ* **793**, 115

Bouwens, R. J., Illingworth, G. D., Oesch, P. A., Trenti, M., Labbé, I., Bradley, L., Carollo, M., van Dokkum, P. G., Gonzalez, V., Holwerda, B., Franx, M., Spitler, L., Smit, R., and Magee, D.: 2015, *ApJ* **803**, 34

Bovy, J., Hogg, D. W., and Moustakas, J.: 2008, *ApJ* **688**, 198

Bowler, R. A. A., Dunlop, J. S., McLure, R. J., McCracken, H. J., Milvang-Jensen, B., Furusawa, H., Taniguchi, Y., Le Fèvre, O., Fynbo, J. P. U., Jarvis, M. J., and Häußler, B.: 2015, *MNRAS* **452**, 1817

Bradač, M., Schneider, P., Lombardi, M., and Erben, T.: 2005, *A&A* **437**, 39

Bradley, L. D., Bouwens, R. J., Ford, H. C., Illingworth, G. D., Jee, M. J., Benítez, N., Broadhurst, T. J., Franx, M., Frye, B. L., Infante, L., Motta, V., Rosati, P., White, R. L., and Zheng, W.: 2008, *ApJ* **678**, 647

Bradley, L. D., Trenti, M., Oesch, P. A., Stiavelli, M., Treu, T., Bouwens, R. J., Shull, J. M., Holwerda, B. W., and Pirzkal, N.: 2012, *ApJ* **760**, 108

Brammer, G. B., van Dokkum, P. G., and Coppi, P.: 2008, *ApJ* **686**, 1503

Broadhurst, T. J., Taylor, A. N., and Peacock, J. A.: 1995, *ApJ* **438**, 49

Bruzual, G. and Charlot, S.: 2003, *MNRAS* **344**, 1000

Budavári, T., Szalay, A. S., Charlot, S., Seibert, M., Wyder, T. K., Arnouts, S., Barlow, T. A., Bianchi, L., Byun, Y.-I., Donas, J., Forster, K., Friedman, P. G., Heckman, T. M., Jelinsky, P. N., Lee, Y.-W., Madore, B. F., Malina, R. F., Martin, D. C., Milliard, B., Morrissey, P., Neff, S. G., Rich, R. M., Schiminovich, D., Siegmund, O. H. W., Small, T., Treyer, M. A., and Welsh, B.: 2005, *ApJL* **619**, L31

Bunker, A. J., Stanway, E. R., Ellis, R. S., and McMahon, R. G.: 2004, *MNRAS* **355**, 374

Bunker, A. J., Wilkins, S., Ellis, R. S., Stark, D. P., Lorenzoni, S., Chiu, K., Lacy, M., Jarvis, M. J., and Hickey, S.: 2010, *MNRAS* **409**, 855

Calzetti, D., Armus, L., Bohlin, R. C., Kinney, A. L., Koornneef, J., and Storchi-Bergmann, T.: 2000, *ApJ* **533**, 682

Calzetti, D. and Heckman, T. M.: 1999, *ApJ* **519**, 27

Calzetti, D., Kinney, A. L., and Storchi-Bergmann, T.: 1994, *ApJ* **429**, 582

Casertano, S., de Mello, D., Dickinson, M., Ferguson, H. C., Fruchter, A. S., Gonzalez-Lopezlira, R. A., Heyer, I., Hook, R. N., Levay, Z., Lucas, R. A., Mack, J., Makidon, R. B., Mutchler, M., Smith, T. E., Stiavelli, M., Wiggs, M. S., and Williams, R. E.: 2000, *AJ* **120**, 2747

Castellano, M., Fontana, A., Grazian, A., Pentericci, L., Santini, P., Koekemoer, A., Cristiani, S., Galametz, A., Gallerani, S., Vanzella, E., Boutsia, K., Gallozzi, S., Giallongo, E., Maiolino, R., Menci, N., and Paris, D.: 2012, *A&A* **540**, A39

Chabrier, G.: 2003, *PASP* **115**, 763

Charlot, S. and Fall, S. M.: 2000, *ApJ* **539**, 718

Chelouche, D., Koester, B. P., and Bowen, D. V.: 2007, *ApJL* **671**, L97

Coe, D., Benítez, N., Broadhurst, T., and Moustakas, L. A.: 2010, *ApJ* **723**, 1678

Coe, D., Zitrin, A., Carrasco, M., Shu, X., Zheng, W., Postman, M., Bradley, L., Koekemoer, A., Bouwens, R., Broadhurst, T., Monna, A., Host, O., Moustakas, L. A., Ford, H., Moustakas, J., van der Wel, A., Donahue, M., Rodney, S. A., Benítez, N., Jouvel, S., Seitz, S., Kelson, D. D., and Rosati, P.: 2013, *ApJ* **762**, 32

Coleman, G. D., Wu, C.-C., and Weedman, D. W.: 1980, *ApJS* **43**, 393

Conroy, C. and Wechsler, R. H.: 2009, *ApJ* **696**, 620

Conroy, C., Wechsler, R. H., and Kravtsov, A. V.: 2006, *ApJ* **647**, 201

Cucciati, O., Tresse, L., Ilbert, O., Le Fèvre, O., Garilli, B., Le Brun, V., Cassata, P., Franzetti, P., Maccagni, D., Scodeggio, M., Zucca, E., Zamorani, G., Bardelli, S., Bolzonella, M., Bielby, R. M., McCracken, H. J., Zanichelli, A., and Vergani, D.: 2012, *A&A* **539**, A31

Daddi, E., Cimatti, A., Renzini, A., Fontana, A., Mignoli, M., Pozzetti, L., Tozzi, P., and Zamorani, G.: 2004, *ApJ* **617**, 746

Dahlen, T., Mobasher, B., Dickinson, M., Ferguson, H. C., Giavalisco, M., Grogin, N. A., Guo, Y., Koekemoer, A., Lee, K.-S., Lee, S.-K., Nonino, M., Riess, A. G., and Salimbeni, S.: 2010, *ApJ* **724**, 425

Dahlen, T., Mobasher, B., Dickinson, M., Ferguson, H. C., Giavalisco, M., Kretchmer, C., and Ravindranath, S.: 2007, *ApJ* **654**, 172

Dekel, A. and Birnboim, Y.: 2006, *MNRAS* **368**, 2

Dickinson, M., Stern, D., Giavalisco, M., Ferguson, H. C., Tsvetanov, Z., Chornock, R., Cristiani, S., Dawson, S., Dey, A., Filippenko, A. V., Moustakas, L. A., Nonino, M., Papovich, C., Ravindranath, S., Riess, A., Rosati, P., Spinrad, H., and Vanzella, E.: 2004, *ApJL* **600**, L99

Diego, J. M., Tegmark, M., Protopapas, P., and Sandvik, H. B.: 2007, *MNRAS* **375**, 958

Diolaiti, E., Bendinelli, O., Bonaccini, D., Close, L., Currie, D., and Parmeggiani, G.: 2000, in N. Manset, C. Veillet, and D. Crabtree (eds.), *Astronomical Data Analysis Software and Systems IX*, Vol. 216 of *Astronomical Society of the Pacific Conference Series*, p. 623

Domínguez, A., Siana, B., Brooks, A. M., Christensen, C. R., Bruzual, G., Stark, D. P., and Alavi, A.: 2015, *MNRAS* **451**, 839

Dunlop, J. S., McLure, R. J., Robertson, B. E., Ellis, R. S., Stark, D. P., Cirasuolo, M., and de Ravel, L.: 2012, *MNRAS* **420**, 901

Dunlop, J. S., Rogers, A. B., McLure, R. J., Ellis, R. S., Robertson, B. E., Koekemoer, A., Dayal, P., Curtis-Lake, E., Wild, V., Charlot, S., Bowler, R. A. A., Schenker, M. A., Ouchi, M., Ono, Y., Cirasuolo, M., Furlanetto, S. R., Stark, D. P., Targett, T. A., and Schneider, E.: 2013, *MNRAS* **432**, 3520

Ebeling, H., Ma, C.-J., and Barrett, E.: 2014, *ApJS* **211**, 21

Egami, E., Kneib, J.-P., Rieke, G. H., Ellis, R. S., Richard, J., Rigby, J., Papovich, C., Stark, D., Santos, M. R., Huang, J.-S., Dole, H., Le Floc'h, E., and Pérez-González, P. G.: 2005, *ApJL* **618**, L5

Erb, D. K., Shapley, A. E., Pettini, M., Steidel, C. C., Reddy, N. A., and Adelberger, K. L.: 2006, *ApJ* **644**, 813

Ferguson, H. C., Dickinson, M., Giavalisco, M., Kretchmer, C., Ravindranath, S., Idzi, R., Taylor, E., Conselice, C. J., Fall, S. M., Gardner, J. P., Livio, M., Madau, P., Moustakas, L. A., Papovich, C. M., Somerville, R. S., Spinrad, H., and Stern, D.: 2004, *ApJL* **600**, L107

Ferguson, H. C., Dickinson, M., and Williams, R.: 2000, *ARA&A* **38**, 667

Finkelstein, S. L., Papovich, C., Salmon, B., Finlator, K., Dickinson, M., Ferguson, H. C., Giavalisco, M., Koekemoer, A. M., Reddy, N. A., Bassett, R., Conselice, C. J., Dunlop, J. S., Faber, S. M., Grogin, N. A., Hathi, N. P., Kocevski, D. D., Lai, K., Lee, K.-S., McLure, R. J., Mobasher, B., and Newman, J. A.: 2012, *ApJ* **756**, 164

Finkelstein, S. L., Ryan, Jr., R. E., Papovich, C., Dickinson, M., Song, M., Somerville, R. S., Ferguson, H. C., Salmon, B., Giavalisco, M., Koekemoer, A. M., Ashby, M. L. N., Behroozi, P., Castellano, M., Dunlop, J. S., Faber, S. M., Fazio, G. G., Fontana, A., Grogin, N. A., Hathi, N., Jaacks, J., Kocevski, D. D., Livermore, R., McLure, R. J., Merlin, E., Mobasher, B., Newman, J. A., Rafelski, M., Tilvi, V., and Willner, S. P.: 2015, *ApJ* **810**, 71

Fioc, M. and Rocca-Volmerange, B.: 1997, *A&A* **326**, 950

Fynbo, J. P. U., Prochaska, J. X., Sommer-Larsen, J., Dessauges-Zavadsky, M., and Møller, P.: 2008, *ApJ* **683**, 321

Gehrels, N.: 1986, *ApJ* **303**, 336

Gonzaga, S. and et al.: 2012, *The DrizzlePac Handbook*

Governato, F., Zolotov, A., Pontzen, A., Christensen, C., Oh, S. H., Brooks, A. M., Quinn, T., Shen, S., and Wadsley, J.: 2012, *MNRAS* **422**, 1231

Grazian, A., Castellano, M., Koekemoer, A. M., Fontana, A., Pentericci, L., Testa, V., Boutsia, K., Giallongo, E., Giavalisco, M., and Santini, P.: 2011, *A&A* **532**, A33

Grazian, A., Fontana, A., de Santis, C., Nonino, M., Salimbeni, S., Giallongo, E., Cristiani, S., Gallozzi, S., and Vanzella, E.: 2006, *A&A* **449**, 951

Haberzettl, L., Williger, G., Lehnert, M. D., Nesvadba, N., and Davies, L.: 2012, *ApJ* **745**, 96

Haberzettl, L., Williger, G. M., Lauroesch, J. T., Haines, C. P., Valls-Gabaud, D., Harris, K. A., Koekemoer, A. M., Loveday, J., Campusano, L. E., Clowes, R. G., Davé, R., Graham, M. J., and Söchting, I. K.: 2009, *ApJ* **702**, 506

Hathi, N. P., Cohen, S. H., Ryan, Jr., R. E., Finkelstein, S. L., McCarthy, P. J., Windhorst, R. A., Yan, H., Koekemoer, A. M., Rutkowski, M. J., O'Connell, R. W., Straughn, A. N., Balick, B., Bond, H. E., Calzetti, D., Disney, M. J., Dopita, M. A., Frogel, J. A., Hall, D. N. B., Holtzman, J. A., Kimble, R. A., Paresce, F., Saha, A., Silk, J. I., Trauger, J. T., Walker, A. R., Whitmore, B. C., and Young, E. T.: 2013, *ApJ* **765**, 88

Hathi, N. P., Le Fèvre, O., Ilbert, O., Cassata, P., Tasca, L. A. M., Lemaux, B. C., Garilli, B., Le Brun, V., Maccagni, D., Pentericci, L., Thomas, R., Vanzella, E., Zamorani, G., Zucca, E., Amorín, R., Bardelli, S., Cassarà, L. P., Castellano, M., Cimatti, A., Cucciati, O., Durkalec, A., Fontana, A., Giavalisco, M., Grazian, A., Guaita, L., Koekemoer, A., Paltani, S., Pforr, J., Ribeiro, B., Schaerer, D., Scodeggio, M., Sommariva, V., Talia, M., Tresse, L., Vergani, D., Capak, P., Charlot, S., Contini, T., Cuby, J. G., de la Torre, S., Dunlop, J., Fotopoulou, S., López-Sanjuan, C., Mellier, Y., Salvato, M., Scoville, N., Taniguchi, Y., and Wang, P. W.: 2016, *A&A* **588**, A26

Hathi, N. P., Ryan, Jr., R. E., Cohen, S. H., Yan, H., Windhorst, R. A., McCarthy, P. J., O'Connell, R. W., Koekemoer, A. M., Rutkowski, M. J., Balick, B., Bond, H. E., Calzetti, D., Disney, M. J., Dopita, M. A., Frogel, J. A., Hall, D. N. B., Holtzman, J. A., Kimble, R. A., Paresce, F., Saha, A., Silk, J. I., Trauger, J. T., Walker, A. R., Whitmore, B. C., and Young, E. T.: 2010, *ApJ* **720**, 1708

Heinis, S., Buat, V., Béthermin, M., Aussel, H., Bock, J., Boselli, A., Burgarella, D., Conley, A., Cooray, A., Farrah, D., Ibar, E., Ilbert, O., Ivison, R. J., Magdis, G., Marsden, G.,

Oliver, S. J., Page, M. J., Rodighiero, G., Roehlly, Y., Schulz, B., Scott, D., Smith, A. J., Viero, M., Wang, L., and Zemcov, M.: 2013, *MNRAS* **429**, 1113

Hopkins, A. M. and Beacom, J. F.: 2006, *ApJ* **651**, 142

Hopkins, A. M., Connolly, A. J., and Szalay, A. S.: 2000, *AJ* **120**, 2843

Hopkins, P. F., Kereš, D., Oñorbe, J., Faucher-Giguère, C.-A., Quataert, E., Murray, N., and Bullock, J. S.: 2014, *MNRAS* **445**, 581

Huang, K.-H., Ferguson, H. C., Ravindranath, S., and Su, J.: 2013, *ApJ* **765**, 68

Ilbert, O., Arnouts, S., McCracken, H. J., Bolzonella, M., Bertin, E., Le Fèvre, O., Mellier, Y., Zamorani, G., Pellò, R., Iovino, A., Tresse, L., Le Brun, V., Bottini, D., Garilli, B., Maccagni, D., Picat, J. P., Scaramella, R., Scodeggio, M., Vettolani, G., Zanichelli, A., Adami, C., Bardelli, S., Cappi, A., Charlot, S., Ciliegi, P., Contini, T., Cucciati, O., Foucaud, S., Franzetti, P., Gavignaud, I., Guzzo, L., Marano, B., Marinoni, C., Mazure, A., Meneux, B., Merighi, R., Paltani, S., Pollo, A., Pozzetti, L., Radovich, M., Zucca, E., Bondi, M., Bongiorno, A., Busarello, G., de La Torre, S., Gregorini, L., Lamareille, F., Mathez, G., Merluzzi, P., Ripepi, V., Rizzo, D., and Vergani, D.: 2006, *A&A* **457**, 841

Ilbert, O., McCracken, H. J., Le Fèvre, O., Capak, P., Dunlop, J., Karim, A., Renzini, M. A., Caputi, K., Boissier, S., Arnouts, S., Aussel, H., Comparat, J., Guo, Q., Hudelot, P., Kartaltepe, J., Kneib, J. P., Krogager, J. K., Le Floc'h, E., Lilly, S., Mellier, Y., Milvang-Jensen, B., Moutard, T., Onodera, M., Richard, J., Salvato, M., Sanders, D. B., Scoville, N., Silverman, J. D., Taniguchi, Y., Tasca, L., Thomas, R., Toft, S., Tresse, L., Vergani, D., Wolk, M., and Zirm, A.: 2013, *A&A* **556**, A55

Ishigaki, M., Kawamata, R., Ouchi, M., Oguri, M., Shimasaku, K., and Ono, Y.: 2015, *ApJ* **799**, 12

Iwata, I., Ohta, K., Tamura, N., Akiyama, M., Aoki, K., Ando, M., Kiuchi, G., and Sawicki, M.: 2007, *MNRAS* **376**, 1557

Izotov, Y. I., Orlitová, I., Schaerer, D., Thuan, T. X., Verhamme, A., Guseva, N. G., and Worseck, G.: 2016a, *Nat.* **529**, 178

Izotov, Y. I., Schaerer, D., Thuan, T. X., Worseck, G., Guseva, N. G., Orlitová, I., and Verhamme, A.: 2016b, *MNRAS* **461**, 3683

Jaacks, J., Thompson, R., and Nagamine, K.: 2013, *ApJ* **766**, 94

Janknecht, E., Reimers, D., Lopez, S., and Tytler, D.: 2006, *A&A* **458**, 427

Jauzac, M., Richard, J., Jullo, E., Clément, B., Limousin, M., Kneib, J.-P., Ebeling, H., Natarajan, P., Rodney, S., Atek, H., Massey, R., Eckert, D., Egami, E., and Rexroth, M.: 2015, *MNRAS* **452**, 1437

Jones, T., Ellis, R., Jullo, E., and Richard, J.: 2010, *ApJL* **725**, L176

Jullo, E. and Kneib, J.-P.: 2009, *MNRAS* **395**, 1319

Jullo, E., Kneib, J.-P., Limousin, M., Elíasdóttir, Á., Marshall, P. J., and Verdugo, T.: 2007, *New Journal of Physics* **9**, 447

Kennicutt, Jr., R. C.: 1998, *ARA&A* **36**, 189

Kim, T.-S., Hu, E. M., Cowie, L. L., and Songaila, A.: 1997, *AJ* **114**, 1

Kinney, A. L., Calzetti, D., Bohlin, R. C., McQuade, K., Storchi-Bergmann, T., and Schmitt, H. R.: 1996, *ApJ* **467**, 38

Kneib, J.-P., Ellis, R. S., Santos, M. R., and Richard, J.: 2004, *ApJ* **607**, 697

Kneib, J.-P. and Natarajan, P.: 2011, *A&AR* **19**, 47

Koekemoer, A. M., Fruchter, A. S., Hook, R. N., and Hack, W.: 2003, in S. Arribas, A. Koekemoer, and B. Whitmore (eds.), *HST Calibration Workshop : Hubble after the Installation of the ACS and the NICMOS Cooling System*, p. 337

Kriek, M., van Dokkum, P. G., Labbé, I., Franx, M., Illingworth, G. D., Marchesini, D., and Quadri, R. F.: 2009, *ApJ* **700**, 221

Kroupa, P.: 2001, *MNRAS* **322**, 231

Kuhlen, M. and Faucher-Giguère, C.-A.: 2012, *MNRAS* **423**, 862

Kuhlen, M., Madau, P., and Krumholz, M. R.: 2013, *ApJ* **776**, 34

Kurczynski, P., Gawiser, E., Rafelski, M., Teplitz, H. I., Acquaviva, V., Brown, T. M., Coe, D., de Mello, D. F., Finkelstein, S. L., Grogin, N. A., Koekemoer, A. M., Lee, K.-s., Scarlata, C., and Siana, B. D.: 2014, *ApJL* **793**, L5

Labbé, I., Franx, M., Rudnick, G., Schreiber, N. M. F., van Dokkum, P. G., Moorwood, A., Rix, H.-W., Röttgering, H., Trujillo, I., and van der Werf, P.: 2007, *ApJ* **665**, 944

Law, D. R., Steidel, C. C., Shapley, A. E., Nagy, S. R., Reddy, N. A., and Erb, D. K.: 2012, *ApJ* **759**, 29

Lee, K.-S., Dey, A., Reddy, N., Brown, M. J. I., Gonzalez, A. H., Jannuzi, B. T., Cooper, M. C., Fan, X., Bian, F., Glikman, E., Stern, D., Brodwin, M., and Cooray, A.: 2011, *ApJ* **733**, 99

Leitherer, C., Schaerer, D., Goldader, J. D., González Delgado, R. M., Robert, C., Kune, D. F., de Mello, D. F., Devost, D., and Heckman, T. M.: 1999, *ApJS* **123**, 3

Liesenborgs, J., De Rijcke, S., and Dejonghe, H.: 2006, *MNRAS* **367**, 1209

Lilly, S. J., Le Fevre, O., Hammer, F., and Crampton, D.: 1996, *ApJL* **460**, L1

Limousin, M., Ebeling, H., Richard, J., Swinbank, A. M., Smith, G. P., Jauzac, M., Rodionov, S., Ma, C.-J., Smail, I., Edge, A. C., Jullo, E., and Kneib, J.-P.: 2012, *A&A* **544**, A71

Limousin, M., Richard, J., Jullo, E., Jauzac, M., Ebeling, H., Bonamigo, M., Alavi, A., Clément, B., Giocoli, C., Kneib, J.-P., Verdugo, T., Natarajan, P., Siana, B., Atek, H., and Rexroth, M.: 2016, *A&A* **588**, A99

Limousin, M., Richard, J., Jullo, E., Kneib, J.-P., Fort, B., Soucail, G., Elíasdóttir, Á., Natarajan, P., Ellis, R. S., Smail, I., Czoske, O., Smith, G. P., Hudelot, P., Bardeau, S., Ebeling, H., Egami, E., and Knudsen, K. K.: 2007, *ApJ* **668**, 643

Livermore, R. C., Finkelstein, S. L., and Lotz, J. M.: 2016, *ArXiv e-prints*

Lotz, J. M., Koekemoer, A., Coe, D., Grogin, N., Capak, P., Mack, J., Anderson, J., Avila, R., Barker, E. A., Borncamp, D., Brammer, G., Durbin, M., Gunning, H., Hilbert, B., Jenkner, H., Khandrika, H., Levay, Z., Lucas, R. A., MacKenty, J., Ogaz, S., Porterfield, B., Reid, N., Robberto, M., Royle, P., Smith, L. J., Storrie-Lombardi, L. J., Sunnquist, B., Surace, J., Taylor, D. C., Williams, R., Bullock, J., Dickinson, M., Finkelstein, S., Natara-

jan, P., Richard, J., Robertson, B., Tumlinson, J., Zitrin, A., Flanagan, K., Sembach, K., Soifer, B. T., and Mountain, M.: 2016, *ArXiv e-prints*

Ly, C., Malkan, M. A., Treu, T., Woo, J.-H., Currie, T., Hayashi, M., Kashikawa, N., Motohara, K., Shimasaku, K., and Yoshida, M.: 2009, *ApJ* **697**, 1410

Ma, X., Hopkins, P. F., Faucher-Giguère, C.-A., Zolman, N., Muratov, A. L., Kereš, D., and Quataert, E.: 2016, *MNRAS* **456**, 2140

Madau, P.: 1995, *ApJ* **441**, 18

Madau, P. and Dickinson, M.: 2014, *ARA&A* **52**, 415

Madau, P., Ferguson, H. C., Dickinson, M. E., Giavalisco, M., Steidel, C. C., and Fruchter, A.: 1996, *MNRAS* **283**, 1388

Madau, P., Ferrara, A., and Rees, M. J.: 2001, *ApJ* **555**, 92

Magnelli, B., Elbaz, D., Chary, R. R., Dickinson, M., Le Borgne, D., Frayer, D. T., and Willmer, C. N. A.: 2011, *A&A* **528**, A35

McLean, I. S., Steidel, C. C., Epps, H., Matthews, K., Adkins, S., Konidaris, N., Weber, B., Aliado, T., Brims, G., Canfield, J., Cromer, J., Fucik, J., Kulas, K., Mace, G., Magnone, K., Rodriguez, H., Wang, E., and Weiss, J.: 2010, in *Ground-based and Airborne Instrumentation for Astronomy III*, Vol. 7735 of *SPIE*, pp 77351E–77351E–12

McLean, I. S., Steidel, C. C., Epps, H. W., Konidaris, N., Matthews, K. Y., Adkins, S., Aliado, T., Brims, G., Canfield, J. M., Cromer, J. L., Fucik, J., Kulas, K., Mace, G., Magnone, K., Rodriguez, H., Rudie, G., Trainor, R., Wang, E., Weber, B., and Weiss, J.: 2012, in *Ground-based and Airborne Instrumentation for Astronomy IV*, Vol. 8446 of *SPIE*, p. 84460J

McLure, R. J., Cirasuolo, M., Dunlop, J. S., Foucaud, S., and Almaini, O.: 2009, *MNRAS* **395**, 2196

McLure, R. J., Dunlop, J. S., Bowler, R. A. A., Curtis-Lake, E., Schenker, M., Ellis, R. S., Robertson, B. E., Koekemoer, A. M., Rogers, A. B., Ono, Y., Ouchi, M., Charlot, S., Wild, V., Stark, D. P., Furlanetto, S. R., Cirasuolo, M., and Targett, T. A.: 2013, *MNRAS* **432**, 2696

McLure, R. J., Dunlop, J. S., de Ravel, L., Cirasuolo, M., Ellis, R. S., Schenker, M., Robertson, B. E., Koekemoer, A. M., Stark, D. P., and Bowler, R. A. A.: 2011, *MNRAS* **418**, 2074

Mehta, V., Scarlata, C., Colbert, J. W., Dai, Y. S., Dressler, A., Henry, A., Malkan, M., Rafelski, M., Siana, B., Teplitz, H. I., Bagley, M., Beck, M., Ross, N. R., Rutkowski, M., and Wang, Y.: 2015, *ApJ* **811**, 141

Menci, N., Sanchez, N. G., Castellano, M., and Grazian, A.: 2016, *ApJ* **818**, 90

Merten, J., Cacciato, M., Meneghetti, M., Mignone, C., and Bartelmann, M.: 2009, *A&A* **500**, 681

Merten, J., Coe, D., Dupke, R., Massey, R., Zitrin, A., Cypriano, E. S., Okabe, N., Frye, B., Braglia, F. G., Jiménez-Teja, Y., Benítez, N., Broadhurst, T., Rhodes, J., Meneghetti, M., Moustakas, L. A., Sodré, Jr., L., Krick, J., and Bregman, J. N.: 2011, *MNRAS* **417**, 333

Meurer, G. R., Heckman, T. M., and Calzetti, D.: 1999, *ApJ* **521**, 64

Moller, P. and Jakobsen, P.: 1990, *A&A* **228**, 299

Mosleh, M., Williams, R. J., Franx, M., Gonzalez, V., Bouwens, R. J., Oesch, P., Labbe, I., Illingworth, G. D., and Trenti, M.: 2012, *ApJL* **756**, L12

Muller, S., Wu, S.-Y., Hsieh, B.-C., González, R. A., Loinard, L., Yee, H. K. C., and Gladders, M. D.: 2008, *ApJ* **680**, 975

Muzzin, A., Marchesini, D., Stefanon, M., Franx, M., McCracken, H. J., Milvang-Jensen, B., Dunlop, J. S., Fynbo, J. P. U., Brammer, G., Labbé, I., and van Dokkum, P. G.: 2013, *ApJ* **777**, 18

Narayan, R., Blandford, R., and Nityananda, R.: 1984, *Nat.* **310**, 112

Nestor, D. B., Shapley, A. E., Kornei, K. A., Steidel, C. C., and Siana, B.: 2013, *ApJ* **765**, 47

Nestor, D. B., Shapley, A. E., Steidel, C. C., and Siana, B.: 2011, *ApJ* **736**, 18

Noeske, K., Baggett, S., Bushouse, H., Petro, L., Gilliland, R., and Khozurina-Platais, V.: 2012, *WFC3 UVIS Charge Transfer Eciency October 2009 to October 2011*, Technical report

Oesch, P. A., Bouwens, R. J., Carollo, C. M., Illingworth, G. D., Magee, D., Trenti, M., Stiavelli, M., Franx, M., Labbé, I., and van Dokkum, P. G.: 2010a, *ApJL* **725**, L150

Oesch, P. A., Bouwens, R. J., Illingworth, G. D., Carollo, C. M.,oesch Franx, M., Labbé, I., Magee, D., Stiavelli, M., Trenti, M., and van Dokkum, P. G.: 2010b, *ApJL* **709**, L16

Oesch, P. A., Bouwens, R. J., Illingworth, G. D., Franx, M., Ammons, S. M., van Dokkum, P. G., Trenti, M., and Labbé, I.: 2015, *ApJ* **808**, 104

Oesch, P. A., Stiavelli, M., Carollo, C. M., Bergeron, L. E., Koekemoer, A. M., Lucas, R. A., Pavlovsky, C. M., Trenti, M., Lilly, S. J., Beckwith, S. V. W., Dahlen, T., Ferguson, H. C., Gardner, J. P., Lacey, C., Mobasher, B., Panagia, N., and Rix, H.-W.: 2007, *ApJ* **671**, 1212

Oguri, M.: 2010, *PASJ* **62**, 1017

Oke, J. B. and Gunn, J. E.: 1983, *ApJ* **266**, 713

O'Meara, J. M., Prochaska, J. X., Worseck, G., Chen, H.-W., and Madau, P.: 2013, *ApJ* **765**, 137

Ono, Y., Ouchi, M., Curtis-Lake, E., Schenker, M. A., Ellis, R. S., McLure, R. J., Dunlop, J. S., Robertson, B. E., Koekemoer, A. M., Bowler, R. A. A., Rogers, A. B., Schneider, E., Charlot, S., Stark, D. P., Shimasaku, K., Furlanetto, S. R., and Cirasuolo, M.: 2013, *ApJ* **777**, 155

Ouchi, M., Mobasher, B., Shimasaku, K., Ferguson, H. C., Fall, S. M., Ono, Y., Kashikawa, N., Morokuma, T., Nakajima, K., Okamura, S., Dickinson, M., Giavalisco, M., and Ohta, K.: 2009, *ApJ* **706**, 1136

Ouchi, M., Shimasaku, K., Okamura, S., Furusawa, H., Kashikawa, N., Ota, K., Doi, M., Hamabe, M., Kimura, M., Komiyama, Y., Miyazaki, M., Miyazaki, S., Nakata, F., Sekiguchi, M., Yagi, M., and Yasuda, N.: 2004, *ApJ* **611**, 660

Overzier, R. A., Bouwens, R. J., Cross, N. J. G., Venemans, B. P., Miley, G. K., Zirm, A. W., Benítez, N., Blakeslee, J. P., Coe, D., Demarco, R., Ford, H. C., Homeier, N. L.,

Illingworth, G. D., Kurk, J. D., Martel, A. R., Mei, S., Oliveira, I., Röttgering, H. J. A., Tsvetanov, Z. I., and Zheng, W.: 2008, *ApJ* **673**, 143

Owers, M. S., Randall, S. W., Nulsen, P. E. J., Couch, W. J., David, L. P., and Kempner, J. C.: 2011, *ApJ* **728**, 27

Parsa, S., Dunlop, J. S., McLure, R. J., and Mortlock, A.: 2016, *MNRAS* **456**, 3194

Pettini, M., Rix, S. A., Steidel, C. C., Hunt, M. P., Shapley, A. E., and Adelberger, K. L.: 2002, *Ap&SS* **281**, 461

Pickles, A. J.: 1998, *VizieR Online Data Catalog* **611**, 863

Porciani, C. and Madau, P.: 2005, *ApJL* **625**, L43

Postman, M., Coe, D., Benítez, N., Bradley, L., Broadhurst, T., Donahue, M., Ford, H., Graur, O., Graves, G., Jouvel, S., Koekemoer, A., Lemze, D., Medezinski, E., Molino, A., Moustakas, L., Ogaz, S., Riess, A., Rodney, S., Rosati, P., Umetsu, K., Zheng, W., Zitrin, A., Bartelmann, M., Bouwens, R., Czakon, N., Golwala, S., Host, O., Infante, L., Jha, S., Jimenez-Teja, Y., Kelson, D., Lahav, O., Lazkoz, R., Maoz, D., McCully, C., Melchior, P., Meneghetti, M., Merten, J., Moustakas, J., Nonino, M., Patel, B., Regös, E., Sayers, J., Seitz, S., and Van der Wel, A.: 2012, *ApJS* **199**, 25

Priewe, J., Williams, L. L. R., Liesenborgs, J., Coe, D., and Rodney, S. A.: 2016, *ArXiv e-prints*

Rafelski, M., Teplitz, H. I., Gardner, J. P., Coe, D., Bond, N. A., Koekemoer, A. M., Grogin, N., Kurczynski, P., McGrath, E. J., Bourque, M., Atek, H., Brown, T. M., Colbert, J. W., Codoreanu, A., Ferguson, H. C., Finkelstein, S. L., Gawiser, E., Giavalisco, M., Gronwall, C., Hanish, D. J., Lee, K.-S., Mehta, V., de Mello, D. F., Ravindranath, S., Ryan, R. E., Scarlata, C., Siana, B., Soto, E., and Voyer, E. N.: 2015, *AJ* **150**, 31

Rao, S. M., Turnshek, D. A., and Nestor, D. B.: 2006, *ApJ* **636**, 610

Reddy, N. A., Erb, D. K., Pettini, M., Steidel, C. C., and Shapley, A. E.: 2010, *ApJ* **712**, 1070

Reddy, N. A., Pettini, M., Steidel, C. C., Shapley, A. E., Erb, D. K., and Law, D. R.: 2012, *ApJ* **754**, 25

Reddy, N. A. and Steidel, C. C.: 2009, *ApJ* **692**, 778

Reddy, N. A., Steidel, C. C., Fadda, D., Yan, L., Pettini, M., Shapley, A. E., Erb, D. K., and Adelberger, K. L.: 2006, *ApJ* **644**, 792

Reddy, N. A., Steidel, C. C., Pettini, M., Adelberger, K. L., Shapley, A. E., Erb, D. K., and Dickinson, M.: 2008, *ApJS* **175**, 48

Rees, M. J. and Ostriker, J. P.: 1977, *MNRAS* **179**, 541

Ribaudo, J., Lehner, N., and Howk, J. C.: 2011, *ApJ* **736**, 42

Richard, J., Jauzac, M., Limousin, M., Jullo, E., Clément, B., Ebeling, H., Kneib, J.-P., Atek, H., Natarajan, P., Egami, E., Livermore, R., and Bower, R.: 2014, *MNRAS* **444**, 268

Richard, J., Kneib, J.-P., Ebeling, H., Stark, D. P., Egami, E., and Fiedler, A. K.: 2011, *MNRAS* **414**, L31

Richard, J., Stark, D. P., Ellis, R. S., George, M. R., Egami, E., Kneib, J.-P., and Smith, G. P.: 2008, *ApJ* **685**, 705

Rix, H.-W., Barden, M., Beckwith, S. V. W., Bell, E. F., Borch, A., Caldwell, J. A. R., Häussler, B., Jahnke, K., Jogee, S., McIntosh, D. H., Meisenheimer, K., Peng, C. Y., Sanchez, S. F., Somerville, R. S., Wisotzki, L., and Wolf, C.: 2004, *ApJS* **152**, 163

Robertson, B. E.: 2010, *ApJ* **713**, 1266

Robertson, B. E. and Ellis, R. S.: 2012, *ApJ* **744**, 95

Robertson, B. E., Furlanetto, S. R., Schneider, E., Charlot, S., Ellis, R. S., Stark, D. P., McLure, R. J., Dunlop, J. S., Koekemoer, A., Schenker, M. A., Ouchi, M., Ono, Y., Curtis-Lake, E., Rogers, A. B., Bowler, R. A. A., and Cirasuolo, M.: 2013, *ApJ* **768**, 71

Rogers, A. B., McLure, R. J., and Dunlop, J. S.: 2013, *MNRAS* **429**, 2456

Rogers, A. B., McLure, R. J., Dunlop, J. S., Bowler, R. A. A., Curtis-Lake, E. F., Dayal, P., Faber, S. M., Ferguson, H. C., Finkelstein, S. L., Grogin, N. A., Hathi, N. P., Kocevski, D., Koekemoer, A. M., and Kurczynski, P.: 2014, *MNRAS* **440**, 3714

Salmon, B., Papovich, C., Finkelstein, S. L., Tilvi, V., Finlator, K., Behroozi, P., Dahlen, T., Davé, R., Dekel, A., Dickinson, M., Ferguson, H. C., Giavalisco, M., Long, J., Lu, Y., Mobasher, B., Reddy, N., Somerville, R. S., and Wechsler, R. H.: 2015, *ApJ* **799**, 183

Salpeter, E. E.: 1955, *ApJ* **121**, 161

Sandage, A., Tammann, G. A., and Yahil, A.: 1979, *ApJ* **232**, 352

Sawicki, M.: 2012, *MNRAS* **421**, 2187

Sawicki, M. and Thompson, D.: 2006, *ApJ* **642**, 653

Schechter, P.: 1976, *ApJ* **203**, 297

Schenker, M. A., Robertson, B. E., Ellis, R. S., Ono, Y., McLure, R. J., Dunlop, J. S., Koekemoer, A., Bowler, R. A. A., Ouchi, M., Curtis-Lake, E., Rogers, A. B., Schneider, E., Charlot, S., Stark, D. P., Furlanetto, S. R., and Cirasuolo, M.: 2013, *ApJ* **768**, 196

Schiminovich, D., Ilbert, O., Arnouts, S., Milliard, B., Tresse, L., Le Fèvre, O., Treyer, M., Wyder, T. K., Budavári, T., Zucca, E., Zamorani, G., Martin, D. C., Adami, C., Arnaboldi, M., Bardelli, S., Barlow, T., Bianchi, L., Bolzonella, M., Bottini, D., Byun, Y.-I., Cappi, A., Contini, T., Charlot, S., Donas, J., Forster, K., Foucaud, S., Franzetti, P., Friedman, P. G., Garilli, B., Gavignaud, I., Guzzo, L., Heckman, T. M., Hoopes, C., Iovino, A., Jelinsky, P., Le Brun, V., Lee, Y.-W., Maccagni, D., Madore, B. F., Malina, R., Marano, B., Marinoni, C., McCracken, H. J., Mazure, A., Meneux, B., Morrissey, P., Neff, S., Paltani, S., Pellò, R., Picat, J. P., Pollo, A., Pozzetti, L., Radovich, M., Rich, R. M., Scaramella, R., Scodeggio, M., Seibert, M., Siegmund, O., Small, T., Szalay, A. S., Vettolani, G., Welsh, B., Xu, C. K., and Zanichelli, A.: 2005, *ApJL* **619**, L47

Schlafly, E. F. and Finkbeiner, D. P.: 2011, *ApJ* **737**, 103

Schmidt, K. B., Treu, T., Brammer, G. B., Bradač, M., Wang, X., Dijkstra, M., Dressler, A., Fontana, A., Gavazzi, R., Henry, A. L., Hoag, A., Jones, T. A., Kelly, P. L., Malkan, M. A., Mason, C., Pentericci, L., Poggianti, B., Stiavelli, M., Trenti, M., von der Linden, A., and Vulcani, B.: 2014a, *ApJL* **782**, L36

Schmidt, K. B., Treu, T., Trenti, M., Bradley, L. D., Kelly, B. C., Oesch, P. A., Holwerda, B. W., Shull, J. M., and Stiavelli, M.: 2014b, *ApJ* **786**, 57

Sendra, I., Diego, J. M., Broadhurst, T., and Lazkoz, R.: 2014, *MNRAS* **437**, 2642

Shapley, A. E., Steidel, C. C., Erb, D. K., Reddy, N. A., Adelberger, K. L., Pettini, M., Barmby, P., and Huang, J.: 2005, *ApJ* **626**, 698

Shibuya, T., Ouchi, M., and Harikane, Y.: 2015, *ApJS* **219**, 15

Siana, B., Polletta, M. d. C., Smith, H. E., Lonsdale, C. J., Gonzalez-Solares, E., Farrah, D., Babbedge, T. S. R., Rowan-Robinson, M., Surace, J., Shupe, D., Fang, F., Franceschini, A., and Oliver, S.: 2008a, *ApJ* **675**, 49

Siana, B., Smail, I., Swinbank, A. M., Richard, J., Teplitz, H. I., Coppin, K. E. K., Ellis, R. S., Stark, D. P., Kneib, J.-P., and Edge, A. C.: 2009, *ApJ* **698**, 1273

Siana, B., Teplitz, H. I., Chary, R.-R., Colbert, J., and Frayer, D. T.: 2008b, *ApJ* **689**, 59

Smail, I., Ivison, R. J., and Blain, A. W.: 1997, *ApJL* **490**, L5

Somerville, R. S., Hopkins, P. F., Cox, T. J., Robertson, B. E., and Hernquist, L.: 2008, *MNRAS* **391**, 481

Soucail, G., Fort, B., Mellier, Y., and Picat, J. P.: 1987, *A&A* **172**, L14

Sparre, M., Hayward, C. C., Feldmann, R., Faucher-Giguère, C.-A., Muratov, A. L., Kereš, D., and Hopkins, P. F.: 2015, *ArXiv e-prints*

Stark, D. P., Ellis, R. S., Richard, J., Kneib, J.-P., Smith, G. P., and Santos, M. R.: 2007, *ApJ* **663**, 10

Stark, D. P., Swinbank, A. M., Ellis, R. S., Dye, S., Smail, I. R., and Richard, J.: 2008, *Nat.* **455**, 775

Steidel, C. C., Adelberger, K. L., Giavalisco, M., Dickinson, M., and Pettini, M.: 1999, *ApJ* **519**, 1

Teplitz, H. I., Rafelski, M., Kurczynski, P., Bond, N. A., Grogin, N., Koekemoer, A. M., Atek, H., Brown, T. M., Coe, D., Colbert, J. W., Ferguson, H. C., Finkelstein, S. L., Gardner, J. P., Gawiser, E., Giavalisco, M., Gronwall, C., Hanish, D. J., Lee, K.-S., de Mello, D. F., Ravindranath, S., Ryan, R. E., Siana, B. D., Scarlata, C., Soto, E., Voyer, E. N., and Wolfe, A. M.: 2013, *AJ* **146**, 159

Tody, D.: 1986, in D. L. Crawford (ed.), *Society of Photo-Optical Instrumentation Engineers (SPIE) Conference Series*, Vol. 627 of *Society of Photo-Optical Instrumentation Engineers (SPIE) Conference Series*, p. 733

Tomczak, A. R., Quadri, R. F., Tran, K.-V. H., Labbé, I., Straatman, C. M. S., Papovich, C., Glazebrook, K., Allen, R., Brammer, G. B., Kacprzak, G. G., Kawinwanichakij, L., Kelson, D. D., McCarthy, P. J., Mehrtens, N., Monson, A. J., Persson, S. E., Spitler, L. R., Tilvi, V., and van Dokkum, P.: 2014, *ApJ* **783**, 85

Tremaine, S., Gebhardt, K., Bender, R., Bower, G., Dressler, A., Faber, S. M., Filippenko, A. V., Green, R., Grillmair, C., Ho, L. C., Kormendy, J., Lauer, T. R., Magorrian, J., Pinkney, J., and Richstone, D.: 2002, *ApJ* **574**, 740

Trenti, M., Perna, R., Levesque, E. M., Shull, J. M., and Stocke, J. T.: 2012, *ApJL* **749**, L38

Treu, T., Schmidt, K. B., Brammer, G. B., Vulcani, B., Wang, X., Bradač, M., Dijkstra, M., Dressler, A., Fontana, A., Gavazzi, R., Henry, A. L., Hoag, A., Huang, K.-H., Jones, T. A., Kelly, P. L., Malkan, M. A., Mason, C., Pentericci, L., Poggianti, B., Stiavelli, M., Trenti, M., and von der Linden, A.: 2015, *ApJ* **812**, 114

Trujillo-Gomez, S., Klypin, A., Colín, P., Ceverino, D., Arraki, K. S., and Primack, J.: 2015, *MNRAS* **446**, 1140

van der Burg, R. F. J., Hildebrandt, H., and Erben, T.: 2010, *A&A* **523**, A74

Vanzella, E., de Barros, S., Vasei, K., Alavi, A., Giavalisco, M., Siana, B., Grazian, A., Hasinger, G., Suh, H., Cappelluti, N., Vito, F., Amorin, R., Balestra, I., Brusa, M., Calura, F., Castellano, M., Comastri, A., Fontana, A., Gilli, R., Mignoli, M., Pentericci, L., Vignali, C., and Zamorani, G.: 2016, *ApJ* **825**, 41

Vargas, C. J., Bish, H., Acquaviva, V., Gawiser, E., Finkelstein, S. L., Ciardullo, R., Ashby, M. L. N., Feldmeier, J., Ferguson, H., Gronwall, C., Guaita, L., Hagen, A., Koekemoer, A., Kurczynski, P., Newman, J. A., and Padilla, N.: 2014, *ApJ* **783**, 26

Vasei, K., Siana, B., Shapley, A. E., Quider, A. M., Alavi, A., Rafelski, M., Steidel, C. C., Pettini, M., and Lewis, G. F.: 2016, *ArXiv e-prints*

Wang, X., Hoag, A., Huang, K.-H., Treu, T., Bradač, M., Schmidt, K. B., Brammer, G. B., Vulcani, B., Jones, T. A., Ryan, Jr., R. E., Amorín, R., Castellano, M., Fontana, A., Merlin, E., and Trenti, M.: 2015, *ApJ* **811**, 29

Weiner, B. J., Willmer, C. N. A., Faber, S. M., Harker, J., Kassin, S. A., Phillips, A. C., Melbourne, J., Metevier, A. J., Vogt, N. P., and Koo, D. C.: 2006, *ApJ* **653**, 1049

Weisz, D. R., Johnson, B. D., and Conroy, C.: 2014, *ApJL* **794**, L3

White, S. D. M. and Rees, M. J.: 1978, *MNRAS* **183**, 341

Wilkins, S. M., Bunker, A. J., Stanway, E., Lorenzoni, S., and Caruana, J.: 2011, *MNRAS* **417**, 717

Williams, M. J., Bureau, M., and Cappellari, M.: 2009, in S. Jogee, I. Marinova, L. Hao, and G. A. Blanc (eds.), *Galaxy Evolution: Emerging Insights and Future Challenges*, Vol. 419 of *Astronomical Society of the Pacific Conference Series*, p. 167

Windhorst, R. A., Cohen, S. H., Hathi, N. P., McCarthy, P. J., Ryan, Jr., R. E., Yan, H., Baldry, I. K., Driver, S. P., Frogel, J. A., Hill, D. T., Kelvin, L. S., Koekemoer, A. M., Mechtley, M., O'Connell, R. W., Robotham, A. S. G., Rutkowski, M. J., Seibert, M., Straughn, A. N., Tuffs, R. J., Balick, B., Bond, H. E., Bushouse, H., Calzetti, D., Crockett, M., Disney, M. J., Dopita, M. A., Hall, D. N. B., Holtzman, J. A., Kaviraj, S., Kimble, R. A., MacKenty, J. W., Mutchler, M., Paresce, F., Saha, A., Silk, J. I., Trauger, J. T., Walker, A. R., Whitmore, B. C., and Young, E. T.: 2011, *ApJS* **193**, 27

Wyder, T. K., Treyer, M. A., Milliard, B., Schiminovich, D., Arnouts, S., Budavári, T., Barlow, T. A., Bianchi, L., Byun, Y.-I., Donas, J., Forster, K., Friedman, P. G., Heckman, T. M., Jelinsky, P. N., Lee, Y.-W., Madore, B. F., Malina, R. F., Martin, D. C., Morrissey, P., Neff, S. G., Rich, R. M., Siegmund, O. H. W., Small, T., Szalay, A. S., and Welsh, B. Y.: 2005, *ApJL* **619**, L15

Yan, H., Dickinson, M., Giavalisco, M., Stern, D., Eisenhardt, P. R. M., and Ferguson, H. C.: 2006, *ApJ* **651**, 24

Yan, H. and Windhorst, R. A.: 2004, *ApJL* **612**, L93

Yan, H.-J., Windhorst, R. A., Hathi, N. P., Cohen, S. H., Ryan, R. E., O'Connell, R. W., and McCarthy, P. J.: 2010, *Research in Astronomy and Astrophysics* **10**, 867

Yoshida, M., Shimasaku, K., Kashikawa, N., Ouchi, M., Okamura, S., Ajiki, M., Akiyama, M., Ando, H., Aoki, K., Doi, M., Furusawa, H., Hayashino, T., Iwamuro, F., Iye, M., Karoji, H., Kobayashi, N., Kodaira, K., Kodama, T., Komiyama, Y., Malkan, M. A., Matsuda, Y., Miyazaki, S., Mizumoto, Y., Morokuma, T., Motohara, K., Murayama, T., Nagao, T., Nariai, K., Ohta, K., Sasaki, T., Sato, Y., Sekiguchi, K., Shioya, Y., Tamura, H., Taniguchi, Y., Umemura, M., Yamada, T., and Yasuda, N.: 2006, *ApJ* **653**, 988

Yuan, T.-T., Kewley, L. J., and Richard, J.: 2013, *ApJ* **763**, 9

Zehavi, I., Zheng, Z., Weinberg, D. H., Frieman, J. A., Berlind, A. A., Blanton, M. R., Scoccimarro, R., Sheth, R. K., Strauss, M. A., Kayo, I., Suto, Y., Fukugita, M., Nakamura, O., Bahcall, N. A., Brinkmann, J., Gunn, J. E., Hennessy, G. S., Ivezić, Ž., Knapp, G. R., Loveday, J., Meiksin, A., Schlegel, D. J., Schneider, D. P., Szapudi, I., Tegmark, M., Vogeley, M. S., York, D. G., and SDSS Collaboration: 2005, *ApJ* **630**, 1

Zheng, W., Postman, M., Zitrin, A., Moustakas, J., Shu, X., Jouvel, S., Høst, O., Molino, A., Bradley, L., Coe, D., Moustakas, L. A., Carrasco, M., Ford, H., Benítez, N., Lauer, T. R., Seitz, S., Bouwens, R., Koekemoer, A., Medezinski, E., Bartelmann, M., Broadhurst, T., Donahue, M., Grillo, C., Infante, L., Jha, S. W., Kelson, D. D., Lahav, O., Lemze, D., Melchior, P., Meneghetti, M., Merten, J., Nonino, M., Ogaz, S., Rosati, P., Umetsu, K., and van der Wel, A.: 2012, *Nat.* **489**, 406

Zitrin, A., Broadhurst, T., Umetsu, K., Coe, D., Benítez, N., Ascaso, B., Bradley, L., Ford, H., Jee, J., Medezinski, E., Rephaeli, Y., and Zheng, W.: 2009, *MNRAS* **396**, 1985

Zitrin, A., Meneghetti, M., Umetsu, K., Broadhurst, T., Bartelmann, M., Bouwens, R., Bradley, L., Carrasco, M., Coe, D., Ford, H., Kelson, D., Koekemoer, A. M., Medezinski, E., Moustakas, J., Moustakas, L. A., Nonino, M., Postman, M., Rosati, P., Seidel, G., Seitz, S., Sendra, I., Shu, X., Vega, J., and Zheng, W.: 2013, *ApJL* **762**, L30

Zitrin, A., Moustakas, J., Bradley, L., Coe, D., Moustakas, L. A., Postman, M., Shu, X., Zheng, W., Benítez, N., Bouwens, R., Broadhurst, T., Ford, H., Host, O., Jouvel, S., Koekemoer, A., Meneghetti, M., Rosati, P., Donahue, M., Grillo, C., Kelson, D., Lemze, D., Medezinski, E., Molino, A., Nonino, M., and Ogaz, S.: 2012, *ApJL* **747**, L9

Zitrin, A., Zheng, W., Broadhurst, T., Moustakas, J., Lam, D., Shu, X., Huang, X., Diego, J. M., Ford, H., Lim, J., Bauer, F. E., Infante, L., Kelson, D. D., and Molino, A.: 2014, *ApJL* **793**, L12